SYSTEMS DESIGN AND UNCERTAINTY QUANTIFICATION OF CO_2 CAPTURE FROM AIR

A Dissertation
Presented to
The Academic Faculty

by

Anshuman Sinha

In Partial Fulfillment
of the Requirements for the Degree
Doctor of Philosophy in the
School of Chemical and Biomolecular Engineering

Georgia Institute of Technology
August 2018

SYSTEMS DESIGN AND UNCERTAINTY QUANTIFICATION OF CO_2 CAPTURE FROM AIR

Approved by:

Dr. Matthew J. Realff, Advisor
School of Chemical and Biomolecular Engineering
Georgia Institute of Technology

Dr. David S. Sholl
School of Chemical and Biomolecular Engineering
Georgia Institute of Technology

Dr. Yoshiaki Kawajiri, Co-Advisor
School of Chemical and Biomolecular Engineering
Georgia Institute of Technology

Dr. Jianjun Shi
Department of Industrial Systems and Engineering
Georgia Institute of Technology

Dr. Christopher W. Jones
School of Chemical and Biomolecular Engineering
Georgia Institute of Technology

Date Approved: April 27, 2018

To friends & family

ACKNOWLEDGEMENTS

I am thankful to a lot of people, without whom it would not have been a wonderful PhD life at Georgia Tech. First I would like to thank Dr. Carson Meredith for the email that he sent me regarding my admission for the PhD program at Georgia Tech. I am greatly thankful to my PhD advisor, Dr. Matthew J. Realff for believing in my capability throughout my PhD life. I learned much about process design and uncertainty quantification because of him. He always encouraged me take multiple side projects which helped me expand my research knowledge. He also helped me grow as an efficient presenter and speaker during various conferences.

I would like to thank my thesis co-advisor, Dr. Yoshiaki Kawajiri. I learnt so much about process simulations and optimization from him. He also helped me write research articles in a professional manner. I am honored to be his student.

I am grateful to my thesis committee, Dr. David S. Sholl, Dr. Christopher Jones and Dr. Jianjun Shi for providing me useful updates during the review process. Dr. Christopher Jones has been an important part of the Direct Air Capture project. His support and experience provided me useful insights which I incorporated in my research work. Dr. David S Sholl has provided me useful insights in my research work. His discipline, multi-tasking, leadership roles and life philosophy has been an important lesson for me in my professional as well as personal life. I am also thankful to Dr. Jianjun Shi (and his student Xiaowei Yue) for providing me useful insights in uncertainty quantification.

I am grateful to my colleagues, Hector Rubiera Landa, Jayashree Kalyanaraman and Trisha Sen, with whom I have fruitful discussions about this research. I am also thankful to all the members of Kawajiri group who helped me prepare for various research talks and presentations. I am also thankful to Harrison Rose and Lalit Darunte who were important part of the research project. My research would not have been complete without their experimental collaboration.

My PhD journey would not have been complete without continuous support of my parents. It was their immense motivation that helped through all the hard times I faced during my stay at Georgia Tech.

One person that deserves the most acknowledgment is my wife, Pallavi. I am happy to have met her during my PhD life. It is because of her constant support, love and motivation that has helped me complete my research work.

TABLE OF CONTENTS

LIST OF TABLES

LIST OF FIGURES

SUMMARY

The rapid increase in concentration of atmospheric CO_2 has stimulated the recent development of CO_2 capture technologies. One of the strategy is to capture CO_2 directly from ambient air which, if successfully implemented, could result in capture of CO_2 from disperse emission sources. My work proposes comparison of adsorbents for Direct Air Capture (DAC) through temperature vacuum swing adsorption (TVSA). The adsorbents are grown as films inside monolith contactors which offer low pressure drop during the adsorption step. To achieve a temperature swing, steam is used as a stripping agent during the desorption step. A cyclic steady state process has been simulated and detailed techno-economic study has been performed on DAC. I have identified sensitive parameters such as gas flow rate, cycle time, adsorbent purchase cost, which effects the overall energy requirements and net economics of the Direct Air Capture process.

Another area of CO_2 capture is enclosed environments. Removal of CO_2 from enclosed environment, such as commercial buildings is also of critical importance, primarily due to health risks associated with high CO_2 concentration (>0.5%). In this study, I have designed and modeled a modified air conditioning system which regulates temperature as well as air quality inside an enclosed environment. The model is simulated on a 24 hour timescale including time varying human occupancy of the room. Human respiration and perspiration dynamics have been taken into consideration while modeling the complex multi-bed system. The system is optimized keeping realistic constraint as per ASHRAE standards to maintain a complex state of CO_2, O_2 and humidity levels with

operation of air flow through different beds and recirculation. The optimized model shows improvement in performance as compared with conventional ventilation systems.

CO_2 capture systems have been modeled by understanding the physical process and solving coupled heat and mass balances equations through numerical simulators. Model parameters such as mass transfer coefficient, inlet flow rates etc. often remains uncertain due to lack of precise measurement as well as incomplete information. The accuracy of model outputs and performance metrics such as the net energy and cost can be questioned because of these parametric uncertainties. Hence, quantification of these uncertainties is necessary for more useful model predictions. I have employed Polynomial Chaos Expansion (PCE) methods (intrusive and non-intrusive) to quantify model uncertainty and compared it with Monte Carlo Simulations (MCS). Galerkin method is used to solve intrusive case, Latin Hypercube is used as sampling method and Nataf transformations are used for handling correlations in random variables. The PCE methods have shown better performance in terms of computational time, as compared to MCS. The intrusive PCE method shows higher complexity in model formulation but reduced computational time as compared to non-intrusive PCE method.

In order to model all these systems, partial differential algebraic equations have been implemented in gPROMS, which is a commercial dynamic process modeling and optimization software. Linear driving force (LDF) model is used to approximate the rate of CO2 adsorption. The model is solved discretizing axial and radial domain using second order centered finite difference method (CFDM). Further, MATLAB lsqnonlin solver is used to solve nonlinear curve fitting for parameter estimation of isotherm data points obtained from experiments.

CHAPTER 1. INTRODUCTION

1.1 CO_2 capture from Air

CO_2 concentration in the atmosphere have risen from a pre-industrial level of 270 ppm to around 408 ppm today. This rise has led to increased trapping of heat by the atmosphere and a potential for catastrophic climate change. To mitigate this threat, efforts needs to be made to reduce CO_2 emissions and to directly manage the concentration of CO_2 in the atmosphere. To reduce emissions, one strategy is to capture CO_2 from stationary sources. Such plans usually focus on removing CO_2 from power plant or industrial flue gases and then to transport it to a sequestration site through pipelines. The wide scale deployment of a costly new pipeline infrastructure for a gas that is heavier than air, and an asphyxiate, may be a prohibitive barrier to such a scheme, and limit this capture approach to those places where sequestration is very close to the point emission. In addition, point sources accounts for approximately only one-third of the global emissions and therefore may not constitute enough emissions reduction to avoid further significant changes in atmospheric concentrations. In contrast, another strategy is to capture CO_2 directly from ambient air which, if successfully implemented, could result in capture of CO_2 from disperse emission sources. In contrast to CO_2 capture from stationary sources, Direct Air Capture (DAC) plants are location independent. Thus, the DAC plant can be set up near the sequestration site, eliminating the need for CO_2 transportation infrastructure. The design and evaluation of DAC systems through mathematical modeling and cost estimation motivates this thesis.

CO_2 capture from air can be performed through absorption or adsorption [1]. The absorption approach involves CO_2 capture through chemical solvents such as caustic soda and is

generally associated with high heat of reaction and regeneration (+200 kJ/mole). On the other hand, the adsorption approach utilizes solid adsorbents for capturing CO_2. In recent years, adsorbents with significant equilibrium capacity at ambient conditions (CO_2 concentration ~ 400 ppm) have been synthesized. Such adsorbents, having low heat of adsorption (45-70 kJ/mole), can be explored for capturing CO_2 from the atmosphere. This thesis will focus on DAC using adsorbents as a promising technical pathway to achieve carbon capture with the goal of assessing the capital and operating costs and energy requirements for such systems. Details about the adsorption process and the adsorbents under consideration are presented below.

1.2 Adsorption

Figure 1.1 shows schematic of a prototypical adsorption process consisting of two basic steps. During the adsorption step, air flows through a contactor which has adsorbent embedded inside it in the form of powders or films or as part of the wall structure itself. The CO_2 (adsorbate) is adsorbed in the adsorbent through either physisorption (inter-molecular forces) or chemisorption (chemical bonds). The air depleted in CO_2 flows out of the contactor and is sent back to the atmosphere. During the desorption step, CO_2 is extracted out (desorbed) of the adsorbents through application of temperature, pressure or vacuum swing. Depending on the mode of the desorption agent (temperature, pressure or vacuum), the overall process is termed as a temperature, pressure and/or vacuum swing adsorption process.

The adsorption and desorption steps operate in a cyclic manner. The desorption step is also termed a regeneration step since during this step the adsorbent is returned to the state for

the next adsorption step. After a number of cycles, the adsorbent is no longer effective due to deterioration. The period during which the adsorbent is effective is called the lifetime of the adsorbent.

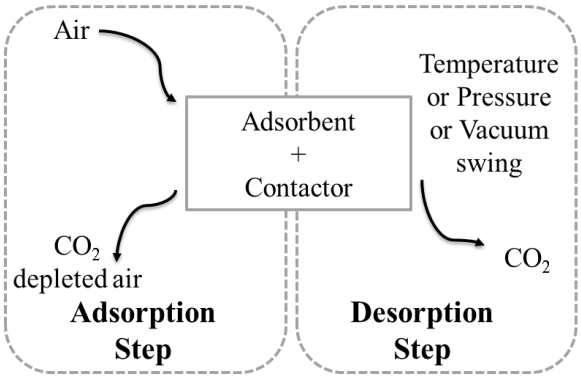

Figure 1.1: Schematic of an adsorption process

The equilibrium quantity of adsorbate adsorbed on the adsorbent is characterized by isotherms which are unique for a pair of adsorbate-adsorbent system. Figure 1.2 shows schematic of a typical isotherm. Depending on the temperature and pressure of the system, the equilibrium quantity of adsorbate adsorbed can be determined. For example, as seen from Figure 1.2, at temperature T_0 and pressure P_0, the equilibrium amount of adsorbate adsorbed on the adsorbent is q_{eq}. As the temperature is increased the amount adsorbed at a given pressure decreases as shown in Figure 2 where $T_1 > T_0$. The sensitivity of the adsorbed quantity to temperature is governed by the heat of adsorption of the material, and the higher this value is, the more sensitive the adsorbed quantity is to temperature.

In addition to the equilibrium behavior of the adsorbent, the mass transfer characteristics of the contactor are an important determinant of the process operation. The simplest and widely used method for determining the mass transfer characteristic is linear driving force

(LDF) model. The LDF model assumes that the rate of uptake into the adsorbent is directly proportional to the difference between the surface concentration on the adsorbent and the average loading in the adsorbent. The proportionality constant is the mass transfer coefficient which is dependent on the type of contactor and is determined from the combined effect of external and internal mass transfer resistances. The external and internal mass transfer resistance effects are due to fluid film around the surface of adsorbent and inside the adsorbent crystalline structure respectively.

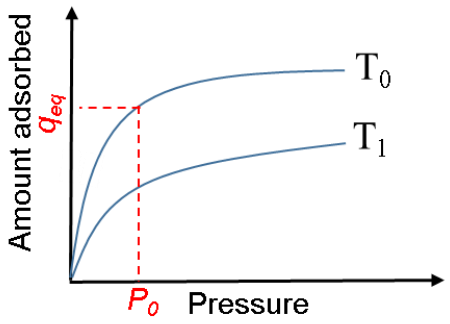

Figure 1.2: Typical Adsorption Isotherms, $T_1 > T_0$

1.3 Adsorbents

An ideal adsorbent is the one which has high adsorption capacity, fast adsorption and desorption kinetics, stable under varied conditions and long lifetime. In reality, no adsorbent is perfect and there are certain tradeoffs for each adsorbent. Ultimately, the adsorbent should be chosen such that it can work efficiently in a realistic separation process. Activated carbon, Zeolites and Metal Organic Frameworks are few of the adsorbents that have been used for CO_2 capture [2].

Activated carbon are well known adsorbents that have been studied for CO_2 separation applications. Wide availability of sources for activated carbon (such as coal, industrial byproducts, biomass, etc.) makes them cheaper for production at industrial scale. However, activated carbons generally have a lower capacity than other adsorbents such as zeolites and MOFs at low pressures [3].

Zeolites are microporous crystalline aluminosilicates that are widely used as adsorbents for gas separation. Figure 1.3 shows a schematic view of three dimensional crystalline structure of zeolites. Due to their unique structural characteristics, zeolites have shown high adsorption capacity for CO_2 adsorption under mild temperature conditions [4]. However, zeolites shows decrease in CO_2 adsorption capacity under humid conditions since water molecules compete with CO_2 for adsorption sites on zeolites [5].

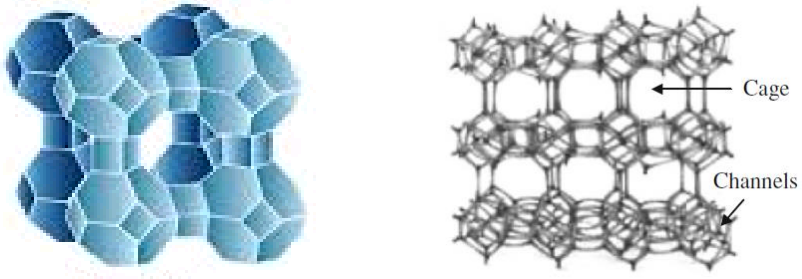

Figure 1.3: Crystal structure of zeolites (left) and zeolite structure showing three dimensional cages and channels (right)

Metal Organic Frameworks (MOFs) are hybrid materials consisting of metal ions that are coordinated with organic ligands forming a multi-dimensional structure with permanent porosity. Because of various combinations of metals and organic linkers, there are over

20,000 MOFs reported in the literature [6]. Due to the wide variety and functionalities of MOFs, they provide a very versatile platform for many applications. MOFs offer certain advantages compared to other substrates such as silica. MOFs have large pore volume, tunable pore size and high specific surface area. This has made MOFs potential sorbents for gas separations [7].

Figure 1.4 shows two examples of MOFs: MIL-101(Cr) [8] and Mg_2(dobpdc) (dobpdc^{4-} = 4,4′-dioxido- 3,3′-biphenyldicarboxylate) [9]. These two MOFs in particular exhibit excellent CO_2 adsorption characteristics at ambient CO_2 conditions (refer the isotherms shown in Figure 1.4) due to their high density of open metal sites and high pore volume. In this thesis the focus will be on Metal Organic Frameworks (MOFs) as the solid adsorbent that has a high potential for DAC applications.

MIL-101 (Cr)-PEI

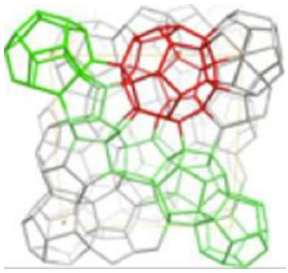

mmen-Mg_2(dobpdc)

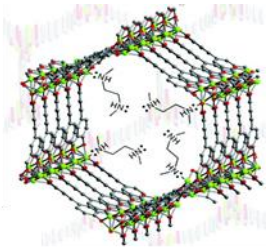

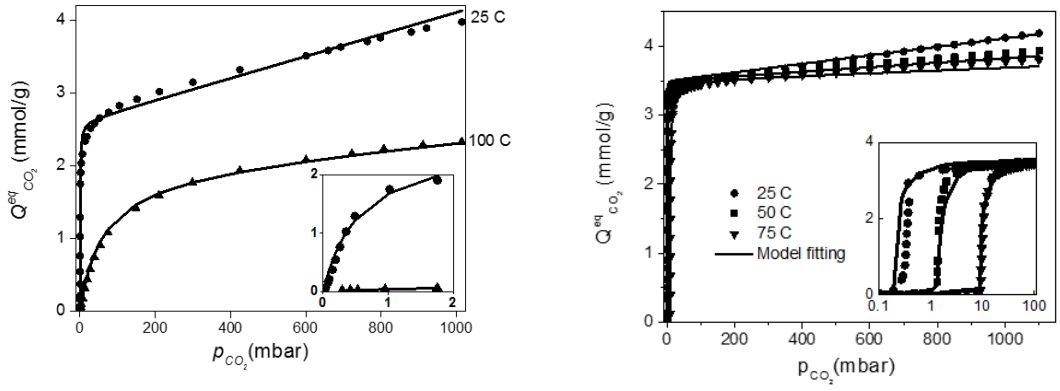

Figure 1.4: Examples of Metal Organic Frameworks with their corresponding isotherms

1.4 Contactors

Contactors are widely used in gas separation processes and act as support structures for the adsorbents. Figure 1.5 shows two examples of contactors: monoliths and packed beds. In packed beds the adsorbent particles are moulded or compressed into pellets sometime using a binder to keep the individual particles together. Packed beds provide large surface area for adsorption to take place and a high density of sorbent per unit volume of contactor. However the disadvantage of using packed bed is that it suffers from very high pressure drop for the gas to flow through it due to the tortuous path the gas must take through the packing. On the other hand, monoliths are a form of structured packing that consist of multiple channels where each channel has nearly the same geometry. This results in lower pressure drop for a given velocity flow, higher mass transfer rates at a given pressure drop, as well as provide larger surface area compared to a packed bed, but lower overall sorbent density if it is as a film on the monolith channel surface. This makes monoliths favourable for gas separation processes, especially CO_2 capture from air, where large volume of air

needs to be passed through the contactors for significant removal of CO_2 and the energy cost of providing the flow, proportional to the pressure drop, must be minimized.

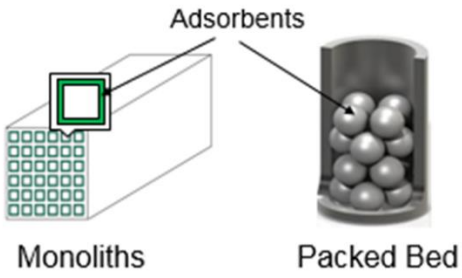

Figure 1.5: Examples of contactors: Monoliths (left) and Packed bed (right)

1.5 Process simulation

Process simulation is performed in order to understand the performance of a given contactor adsorbent combination for CO_2 capture from air. Key gas components of the system are identified such as CO_2, H_2O, and inert gases, and a mass balance is performed for each of these components in each of the phases of the contactor, for example the gas and sorbent phases. Energy balances are similarly developed for each of the phases and a momentum balance for the gas phase. This results in a system of momentum, heat and mass balance equations which are coupled with each other. Hence, changes in the energy profile of one phase effects the concentration profile of another component. For example, adsorption is an exothermic process which changes the temperature of the adsorbent phase, reducing the equilibrium concentration of CO_2. In addition, adsorption of CO_2 on the adsorbent results in decrease in partial pressure of CO_2 in the gas phase. Hence, the more adsorption, the lower the gaseous CO_2 concentration and higher the temperature of the contactor.

Process simulation takes certain inputs and generates a series of outputs which capture the behaviour of different phases during adsorption and desorption stage in a cyclic manner. After simulating a certain number of cycles, no further change in the output profile of the components and temperature is observed between consecutive cycles. The system is said to have reached cyclic steady state at this point. The simulation results are analysed at the cyclic steady state, which to optimize process performance measures.

Process simulation is useful to predict the overall performance of the system and to provide key feedback for material synthesis through experiments. Once the process is modelled and simulated, it can be used for model optimization to maximize its performance. Process simulation is also utilized to perform sensitivity analysis which helps in analysing the results over a range of input parameters. Process sensitivity analysis also helps in predicting the parameters which are most vulnerable to model uncertainties. Strategies to handle model uncertainties are presented below.

1.6 Uncertainty Analysis

Uncertainties can arise from a number of sources while predicting model outcomes. CO_2 capture systems are modeled, in this thesis, by understanding the physical process and solving coupled heat and mass balances equations through numerical simulators. Model parameters often remains uncertain due to lack of precise measurement as well as incomplete information. Broadly there are two sources of uncertainty: aleatoric and epistemic. Aleatoric uncertainty, also known as statistical uncertainty, is caused by error in measurement of parameters while performing experiments. This type of uncertainty arises due to limitations of the equipment or execution of complex experiments which involves

series of manual errors. Aleatoric uncertainty can be reduced by repetition of experiments several times, however, it not be reduced to zero. For example, measurement of thickness of the adsorbent inside the contactor is complicated due to small size of the system and variability in adsorbent thickness each time new adsorbent is grown on the contactor.

Epistemic uncertainty, also known as systematic uncertainty, arises due to assumptions incorporated in formulating the model. These assumptions bring uncertainty in describing the exact physical process resulting in uncertainty in process outcome. For example, mass transfer rates of the CO_2 adsorption are computed from empirical relations which involves understanding the diffusivity mechanism of CO_2 inside the MOF crystals. However, since the diffusivity of CO_2 inside the particular MOF used in this thesis has not been experimentally observed, it was assumed that the CO_2 exhibits similar diffusivity as in other MOFs which can be found in the literature. This assumption brings uncertainty in the mass transfer rate. The accuracy of model outputs and performance metrics such as the amount and purity of CO_2 captured can be questioned because of this parametric uncertainty.

Quantification of model uncertainties is necessary to make model predictions more useful for decision making. Figure 1.6 shows flowchart for uncertainty quantification (UQ). The procedure of process optimization based on UQ is as follows: Initially, the uncertain inputs in the model are identified and a UQ method is chosen to quantify the uncertainty. Then, the uncertainty is propagated through the model using the mathematical procedure which is unique for each UQ method. Finally, based on the uncertainty propagation, n^{th} order moments of the outputs are analyzed as metrics of uncertain performance. The process

performance can then be optimized under uncertainty and a mitigation strategy proposed to minimize the variability in the output due to parametric uncertainties.

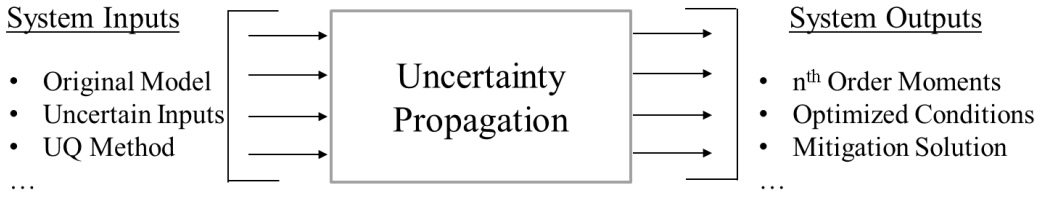

Figure 1.6: Flowsheet for uncertainty quantification

1.7 Thesis summary

The objectives of this thesis are (1) modeling CO_2 capture processes from air, providing cost and energy estimates of their operation, and quantifying the parametric uncertainties in the model using the principles outlined above. In Chapter 2, I discuss the design of temperature vacuum swing adsorption processes for capturing CO_2 from the ambient air. The modeling of the CO_2 capture system is performed by formulating detailed heat and mass balance equations and the resulting mathematical equations are implemented to analyze the model outputs. The energy and economics of CO_2 capture is discussed for a base case parametric values.

In Chapter 3, I present detailed sensitivity analysis of the CO_2 capture by considering best, mid-range and worst case scenarios. The system is analyzed by varying key sensitive parameters and the modeling outcome is utilized to provide feedback for adsorbent synthesis and experimental designs. This chapter also discusses carbon footprint and emissions caused by CO_2 capture from ambient air.

In Chapter 4, I present an analysis on CO_2 capture from enclosed air. I have modeled such a system by proposing a modified ventilation strategy for a sample room inside a building. The mathematical equations resulting from complex heat and mass transfer equation is modeled by programming a multi-bed, multi-component system. The energy requirements of the system is compared with the conventional ventilation system and a scale up study is performed to compute the emissions requirements of the CO_2 capture system from enclosed air.

Parametric uncertainties arising due to modeling of systems in previous chapters is analyzed and quantified in Chapter 5. Polynomial Chaos Expansion (PCE) is chosen as the UQ method and mathematical procedures of different PCE methods is programmed to quantify the multi-dimensional uncertainties. The results from the PCE method is compared with a Monte Carlo method to analyze the process performance.

Finally, I have outlined the main challenges and future opportunities in designing CO_2 capture processes and quantifying uncertainties associated with the model in Chapter 6. This thesis contributes a framework for designing CO_2 capture processes and establishes the economics of CO_2 capture from air through solid adsorbents. Furthermore, this thesis is the first application of PCE methods to gas separation processes.

CHAPTER 2. DIRECT AIR CAPTURE: SYSTEM DESIGN [A]

The current CO_2 level in the atmosphere is over 408 ppm, as reported by Mauna Loa Observatory, and it continues to rise at a rate of around 2 ppm/yr, driven by anthropogenic emissions mainly from fossil fuel combustion.[10-11] Fossil fuels remain abundant and will continue to be the primary source of energy production for much of the world in the near future. For this problem, developing carbon capture utilization and sequestration (CCUS) technologies that act on the atmosphere itself will provide direct control over CO_2 concentrations with the possibility of lowering them over time. CCUS strategies have focused on capturing CO_2 from point sources such as coal-fired power plants, or natural gas production wells. These systems focus on removing CO_2 from flue gases and then transporting it to a sequestration site through pipelines, with possible use to enhance oil recovery. However, point sources account for approximately only one-third of the global emissions.[12] In contrast, the strategy explored in this chapter is to capture CO_2 directly from ambient air. The advantage of this strategy is that it can capture CO_2 from all emission sources, as direct air capture (DAC) plants can be located anywhere, and specifically can be located either near the site of CO_2 sequestration or of a use. Further, ambient air is cleaner than the flue gas from point sources, where the higher concentrations of contaminants such as small particulates and other acid gases such as NO_x and SO_x, which can poison the separating agent.

[A] Portions of this chapter was adapted from Sinha et al. "Systems design and economic analysis of direct air capture of CO_2 through temperature vacuum swing adsorption using MIL-101 (Cr)-PEI-800 and mmen-Mg_2(dobpdc) MOF adsorbents." Ind. Eng. Chem. Res, 56 (3) 2017, 750-764.

2.1 Introduction and Literature Review

CO_2 capture from air has been researched for more than half a century.[13-15] Lackner et al. [16-17] suggested large scale capture of CO_2 from air as an alternative to CCUS from stationary sources. One proposed approach that has reached pilot scale deployment is to absorb CO_2 using sodium hydroxide solutions.[18-22] There have been several studies[12, 23-26] that review DAC technology. Reports by Simon et al.[27] and Smith, Pete et al.[28] stress the need for substantial research into the kinetics of air capture chemistry to reduce cost and energy requirements. House et al.[29] claimed that air capture technology is likely to require more than 400 kJ of work per mole of CO_2 and costs will be on the order of \$1000/t-CO_2. Realff and Eisenberger[30] pointed out a flaw in the analysis of House et al., [29] stating that because the adsorption capture process is exothermic, the usual scaling of costs with feed dilution do not apply, and the minimum work of capture of CO_2 scales only logarithmically with concentration and is therefore not as serious a barrier as might be expected. A report by the American Physical Society (APS) [31] estimates cost for both post combustion capture (PCC) and DAC. The DAC case study was based on a scheme published by Baciocchi et al. [20] which studied CO_2 absorption using a sodium hydroxide solution and regeneration was performed with the help of a calcium hydroxide solution. It estimated the net cost of DAC to be close to \$610/ton CO_2 captured. Krekel et al.[32] concluded the cost of avoiding CO2 emissions to be between \$ 824 (wind) to 1333 (natural gas) / tCO_2 based on a specific process design with huge cost penalty caused due to cyclone which separates the humid air and the carrier gas in their model.

Based on Socolow [31] and the studies mentioned above, one may claim that DAC is economically challenging. However, it is important to note that they considered a particular

process (using NaOH) to arrive at their conclusion or used scaling from other mineral separation technologies. Zeman [33] pointed out that the APS estimates can be significantly reduced from \$610 to \$309/tCO_2 with reduced carbon electricity and plastic packing materials. Other alternatives for capturing CO_2 (such as using solid adsorbents like zeolites or MOFs) can be explored since solid sorbents have lower heats of adsorption (45-70 kJ/mole) compared to the heat of reaction of sodium hydroxide and calcination reaction (+200 kJ/mole). These processes have other energy and cost components as well and the conclusion for energy and economic analysis may vary for such processes. Kulkarni et al.[34] analyzed temperature swing adsorption processes for DAC using purity of CO_2 and annual product throughput as metric for comparing process performance. They used steam as stripping agent to capture CO_2 from air using a specific adsorbent TRI-PE-MCM-41. They considered two approaches: One approach was to use diurnal heating and cooling as a driving force for TSA. In the second approach they used steam to provide heat during desorption. They estimated that at the highest working capacity of the adsorbent as 1.93 mmol/g, and the net operating CO_2 capture cost up to \$100 /t-CO_2 captured depending on the source of electricity. However, their estimates do not include any information about capital cost of DAC.

There have been further studies [8, 35-38] that emphasized the potential merits of CO_2 capture via the adsorption route. Yu et al. [1] provided a qualitative review on absorption and adsorption processes for CO_2 capture. They highlighted the drawbacks of absorption such as high equipment corrosion rate, high energy consumption in regeneration and need for large absorber volume. Furthermore, they also suggested solid adsorption processes to

overcome inherent problems in chemical absorption and highlighted MOFs as promising adsorbents for CO_2 capture.

Metal Organic Frameworks (MOFs) offer large pore volume, tunable pore size and high specific surface area. They have recently attracted significant attention for use in gas separations.[7, 39-41] Yaghi and Millward [42] first reported MOFs with exceptionally high capacity for CO_2 capture at room temperature (298 K). Kuppler et al. [43-44] reviewed the application and progress of MOFs for CO_2 capture. MOFs have shown better performance in terms of CO_2 uptake and adsorption rate as compared to zeolites.[45-46] MIL-101(Cr)[8, 47-49] and Mg_2(dobpdc)[9] ($dobpdc^{4-}$ = 4,4′-dioxido- 3,3′-biphenyldicarboxylate) are two MOFs that exhibit excellent CO_2 adsorption characteristics at ambient CO_2 conditions due to their high density of open metal sites and high pore volume. The cyclic stability of amine loaded MIL-101(Cr) for DAC has been demonstrated in the literature.[8] A series of studies [9, 50-51] reported experimental studies on Mg_2(dobpdc) to evaluate its performance in CO_2 capture. They concluded that the large capacity, high selectivity and fast kinetics of this material for CO_2 adsorption makes it an attractive adsorbent for removal of CO_2 from air.

Solid sorbents have been used to capture CO_2 through temperature, pressure and vacuum swing cycles. In a study by Rezaei et al.[52], building on earlier work by Lively et al.[53] a rapid temperature swing adsorption process was developed to predict the performance of post-combustion CO_2 capture from flue gas using polymer supported amine hollow fiber sorbents. In their work, the sensitivity of the model to gas and water velocity and initial temperature was evaluated. They predicted that it is possible to achieve high purity and recovery with a cycle time shorter than 3 minutes. Casas et al.[54] used PSA technology for pre-combustion CO_2 capture within an integrated gasification combined cycle (IGCC)

power plant to perform parametric analysis with activated carbon as the adsorbent material. They carried out multi-objective optimization having CO_2 purity and recovery as trade off variables. Wurzbacher et al.[55] demonstrated lab scale capture of CO_2 from dry and humid air using a temperature vacuum swing adsorption (TVSA) with the help of packed bed of diamine-functionalized silica gel beads. They studied the effect of parameters such as adsorption time, desorption temperature, etc. on cyclic adsorption capacity. They also predicted specific energy requirements of the TVSA process to be 0.12 MJ/mol CO_2 of mechanical work and between 0.49 and 0.64 MJ/mol CO_2 of heat, depending on the air relative humidity. Socolow [31] reported a total primary energy requirement of 0.44 MJ/mole for 100% conversion efficiency. In a more recent work by Hefti et al.,[56] a TSA based model was used to compare the performance of five different metal organic frameworks [51] for post combustion CO_2 capture. They found that the specific energy requirement of the processes with these materials was lower than for a commercial 13X zeolite and similar levels of CO_2 purity and recovery could be attained by a lower temperature swing with these materials.

Many alternatives to packed bed systems have been proposed to reduce pressure drop and achieve higher mass throughput. Parallel channel monoliths offer lower pressure drop and higher mass transfer rates than most other mass-solid contactors. The technical feasibility of using parallel channel monoliths for adsorption cycles has already been reported in the literature.[57-59] In studies performed by Rezaei and Webley, [60-61] optimum structures for gas separation processes were explored. Four structured adsorbents, viz. pellet/bead, monolith, laminate and foam, were analyzed. External surface area, the size of the mass transfer zone, pressure drop and mass transfer rates were considered as trade-off variables. Laminate and

monolith structures were finalized as the optimum structures with appropriate spacing and widths for laminate systems and cell densities and voidages for monoliths, respectively. Rezaei et al. _ENREF_62 studied the impact of monolith wall porosity, channel width distribution and adsorbent film thickness on the dynamic behavior of zeolite coated 400 and 1200 cell per square inch (cpsi) monolith adsorbents for CO_2 adsorption. They demonstrated the advantage of zeolite coated monoliths with low wall porosity for gas separation processes. Thus, literature studies [57-61] suggest that monoliths can be considered a feasible option as a support structure for coating MOF films.

There have been a few studies on the application of steam as the stripping agent for CO_2 capture.[63-66] Li et al.[67] carried out lab scale experiments to analyze the stability of three classes of supported amine sorbents under steam stripping conditions during the desorption step. These sorbents were subjected to cyclic adsorption and desorption tests using CO_2 diluted in N_2 and then regenerating the sorbents by contacting them with pure saturated steam with the flow rate at 1.2 g/min at 103°C for 25 min. They have demonstrated that amine adsorbents can show stability in cyclic adsorption/desorption experiments using steam stripping.

The studies discussed above provide useful insights into the development of CO_2 capture technologies. However, no study has yet reported detailed cost and energy analysis of DAC through modeling of a process that employed temperature vacuum swing adsorption on monolith structures coated with MOF films. In this chapter, we propose to evaluate the performance of MIL-101(Cr)-PEI-800[8] and mmen-Mg_2(dobpdc)[51] MOF materials by performing detailed economic and energy analysis of a DAC process employing these two adsorbents. Two case studies (one for each adsorbent) have been performed and

temperature vacuum swing adsorption has been used in each of these case studies to remove CO_2 from the adsorbent film coated on monolithic contactors with the help of saturated steam as the stripping agent. The outcome of this modeling effort is used to provide guidance on materials development to improve the performance of the DAC process.

2.2 Process Model Description

We consider a cyclic TVSA process comparing MIL-101(Cr)-PEI-800 [8] and mmen-Mg_2(dobpdc) [9, 51] as adsorbents coated inside cordierite monolith channels. Figure 2.1 shows an overall view of a monolith support structure with an enlarged schematic of a single monolithic channel, which we assume to be cylindrical for convenience in this analysis. Each monolithic channel is coated with an adsorbent film. The thickness of the adsorbent film is around 60 microns and each monolith channel is around 1270 microns in diameter ($2R_3$) which corresponds with a cell density of 400 cpsi.

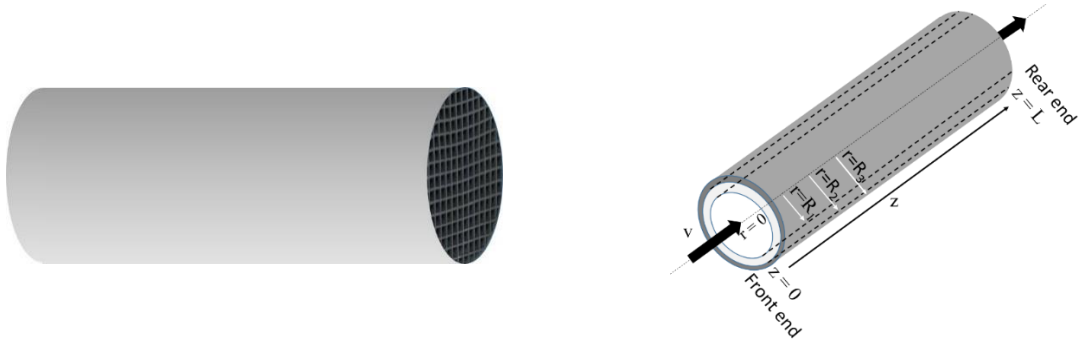

Figure 2.1: Monolithic support structure with multiple channels (left) and schematic of a single monolithic channel (right)

We propose a five step TVSA cycle as illustrated in Figure 2.2. In the adsorption step (Step 1), air is passed through the channel at ambient conditions (298 K, 1 atm and 25% relative humidity). The CO_2 concentration in the air is 400 ppm. This corresponds to a molar concentration of 0.016 mole/m^3. The adsorbent film starts adsorbing this CO_2 during this step, and in cyclic steady state, condensed water is evaporated from the channel surface at the start of the step.

The second step is to evacuate the channel, since it is filled with air (containing oxygen) at the end of adsorption step. This step is required since the amine groups in the MOFs may be oxidized[68-69] at higher temperatures. Hence, the oxygen concentration in the channel must be lowered during the evacuation step. This is achieved by closing the front end ($z = 0$) of the channel and evacuating it by decreasing the pressure at the rear end ($z = L$) with the help of a vacuum pump. This step is finished once the oxygen concentration inside the channel falls below 4% since at that oxygen concentration and at 373 K, the amine groups in MOFs have been observed not to be oxidized to any significant extent. [69] It is assumed that the vacuum is pulled rapidly and that the dynamics of the mass transfer from the MOF does not allow CO_2 to desorb from the surface.

The third step is to pressurize the channel to 1 atm to prevent any backflow of air (oxygen) from the rear end ($z = L$) of the channel. This is done by closing the rear end of the channel and passing saturated steam at 1 atm through the front end ($z = 0$) until the entire channel is pressurized; this happens very rapidly.

For the desorption step (Step 4), the rear end ($z = L$) of the channel is opened and saturated steam at 1 atm is fed to the channel from the front end ($z = 0$). The steam condenses on the

surface of the adsorbent, increasing its temperature. This results in CO_2 desorption during this step due to the temperature swing.

The last step (cooling) of the TVSA cycle is to cool the system down to 348 K. This step is essential because at the end of desorption step, the system is at 373 K. This poses the risk of oxidative degeneration of amine groups in the adsorbent if we start flowing air (Step 1) through the channel. Hence, it is necessary to bring the channel temperature down, and we have used 348 K since the amine groups do not show significant oxidative degeneration when the temperature is in this range.[69] To achieve this, we close the front end ($z = 0$) of the channel and decrease the pressure at the rear end ($z = L$), using the vacuum pump, so that some of the water condensed on the adsorbent surface evaporates, thereby cooling the adsorbent.

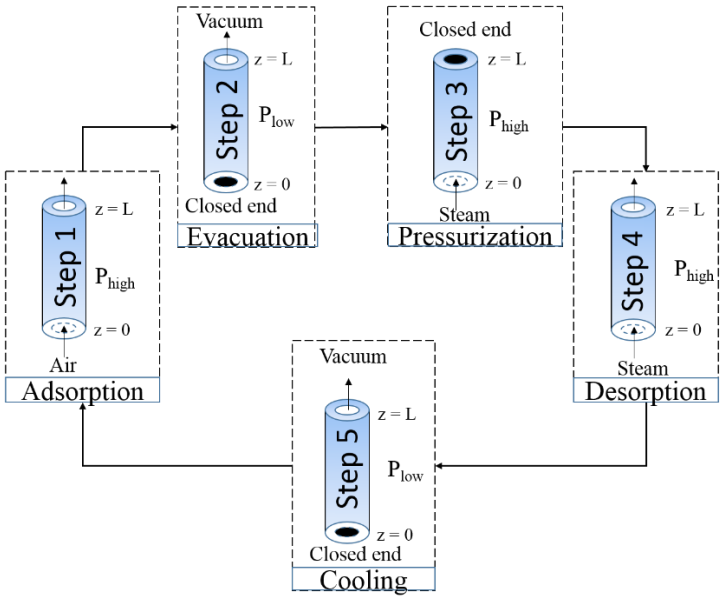

Figure 2.2: Overview of the steps involved in the TVSA model for DAC.

2.3 Model Equations

A mathematical model has been developed to simulate the DAC process to capture temperature and concentration dynamics of the TVSA model. The following assumptions were made to develop the mathematical model:

- Air is considered to have oxygen and nitrogen components in addition to the CO_2 (and 25% relative humidity) and the saturated steam is pure.
- Ideal gas law and ideal mixtures are assumed for the non-condensible components;
- Temperature and concentration variations are neglected in the radial direction in the adsorbent film and monolith wall leading to a lumped model in the radial coordinate for these model elements.
- Adsorbent film thickness is uniform in the axial direction;
- During the desorption step, condensed water does not penetrate inside the MOF pores due to high flowrate of desorbed CO_2 from the MOF pores in the opposing direction. Thus, heat is conducted into the MOF and wall and is not transferred by diffusion of steam within the MOF phase following steam condensation.
- Heat loss from the channel is negligible during all steps of the cycle.

The pressure drop across the channel is given by the Hagen-Poiseuille equation: [70]

$$\Delta P = \frac{8 L \mu v}{R_1^{\,2}} \tag{1}$$

where L is the length of the channel, *v* is the velocity of gas inside the channel, μ is the gaseous viscosity and R_1 is channel inner radius. The CO_2 adsorption rate is approximated by linear driving force model [71] as given by:

$$\frac{\partial Q_{CO2}}{\partial t} = k\left(Q^{eq}{}_{CO_2} - Q_{CO_2}\right) \tag{2}$$

where Q_{CO2} is the adsorbed CO_2 concentration. $Q^{eq}{}_{CO2}$ and *k* are the equilibrium concentration of CO_2 as determined by isotherm equations and overall mass transfer coefficient [71]. The heats of adsorption for CO_2 were determined using Clausius−Clapeyron equation at 25, 50 and 75 °C. They were calculated to be around 55 kJ/mole for MIL-101(Cr)-PEI-800 and 70 kJ/mole for mmen-Mg_2(dobpdc). The system design specifications and mass and heat transfer properties are tabulated in Table 2.1 and Table 2.2, respectively.

Table 2.1: System properties for TVSA CO_2 capture.

Name	Symbol	Value
Air thermal conductivity (W/m K)	k_g	0.0257 [72]
Air heat capacity (J/kg K)	$C_{p,g}$	1003 [72]
Air density (kg/m^3)	ρ_g	1.1839 [72]
Adsorbent thermal conductivity (W/m K)	k_{ads}	0.32 [73-74]
Adsorbent heat capacity (J/kg K)	$C_{p,ads}$	892.5 [73, 75]
Adsorbent density (kg/m^3)	ρ_{ads}	500 [73]
Wall thermal conductivity (W/m K)	k_{wall}	1.6 [76]
Wall heat capacity (J/kg K)	$C_{p,wall}$	840 [77]
Wall density (kg/m^3)	ρ_{wall}	2050 [76]
Antoine constants	a,b,c	5.2, 1733.9, -39.5 [78]

Table 2.2: Mass and heat transfer properties.

Parameter	value
D_g (m^2/s)	0.000016
h (W/m^2-K)	75
$T_{ambient}$ (K)	298
$C_{CO_{2_0}}$ (mol/m^3)	0.016
C_{inert_0} (mol/m^3)	40.88
ΔH (J/mol)	55000 (MIL-101(Cr)-PEI-800)
ΔH (J/mol)	70000 (mmen-Mg_2(dobpdc))
A_1 (m)	0.000063
A_2 (m)	0.000052

2.4 Simulation Results

In this section, we compare the results of the base case TVSA model for both the adsorbents, using the parameters for the monolith in Table 2.3 and operating parameters in Table 2.4. We present the results for the adsorption step (step1), desorption step (step 4).

Table 2.3: Systems design parameters for the TVSA cycle CO_2 capture

Name	Unit	Value
Monolith cell density	-	400 cpsi
Channel outer radius	μm	635
Monolith wall thickness	μm	50
Adsorbent film thickness	μm	60
Channel Length	m	0.3
Overall mass transfer coefficient, k	s^{-1}	0.005
Effective diffusivity, D_e	m^2s^{-1}	10^{-11} [79-81]
Reynolds number, *Re*	-	190

Table 2.4: TVSA operating conditions

Parameter	Value (MIL-101(Cr)-PEI-800)	Value (mmen-Mg_2(dobpdc))
v_{step1} (m/s)	3.0	3.0
v_{step4} (m/s)	0.04	0.1
t_{step1} (s)	1150	3600
t_{step4} (s)	1230	900

2.4.1 Adsorption Step

The simulated breakthrough profiles and adsorbed phase concentration fronts for both MIL-101(Cr)-PEI-800 and mmen-Mg_2(dobpdc) are presented in Figure 2.3. The adsorption step is simulated for 6000 seconds for both the adsorbents at the cyclic steady state, utilizing effectively the full adsorption equilibrium of both the adsorbents (for comparison purposes).

Comparing the dynamics of the CO_2 breakthrough fronts for both the adsorbents (shown in Figure 2.3 a) under the same operating conditions, MIL-101(Cr)-PEI-800 undergoes an earlier breakthrough as compared to mmen-Mg_2(dobpdc). Similarly, Figure 2.3 b compares

the average adsorbed CO_2 in the adsorbent film during the adsorption step for both the adsorbents. The average amount of CO_2 adsorbed in the adsorbent is defined as:

$$Q_{avg} = \frac{\int_0^L Q_{CO_2} dz}{L} \tag{3}$$

These results follow directly from the difference in the saturation capacities of the two adsorbents. mmen-Mg_2(dobpdc) has a higher saturation capacity (~2.9 mmol/g) than MIL-101(Cr)-PEI-800 (~ 1 mmol/g) at ambient conditions, (1 mmol/g adsorbent capacity corresponds to 64.8 mmol/m3 of monolithic contactor).

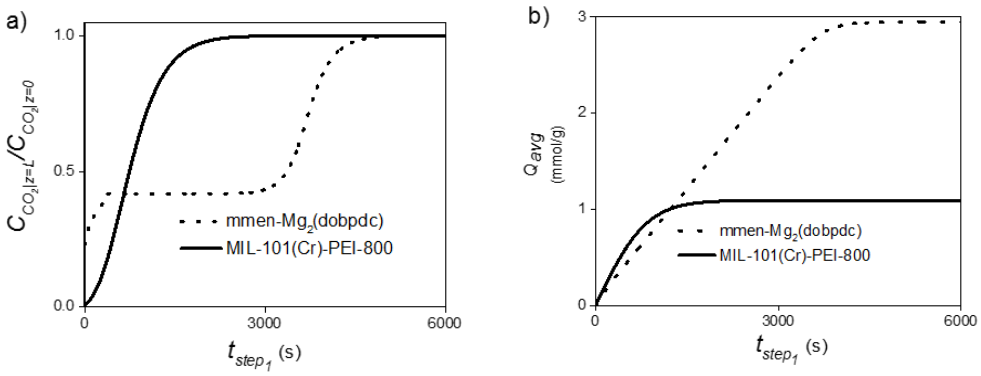

Figure 2.3. a) CO_2 breakthrough profile and b) adsorbed average CO_2 concentration.

2.4.2 Desorption Step

During the desorption step, the saturated steam causes an increase in temperature of the channel. The steam condenses at 373 K upon contacting the adsorbent film, resulting in heat transfer from the condensed water to the adsorbent surface. Figure 2.4a shows the variation of the adsorbent temperature at the channel exit for both the adsorbents. Keeping the steam velocity at 0.04 m/s (for MIL-101(Cr)-PEI-800) and 0.1 m/s (for mmen-

Mg_2(dobpdc)), the desorption step is simulated for 1500 seconds for both the adsorbents at the cyclic steady state, utilizing the full desorption potential of both the adsorbents (for comparison purposes). It can be seen from the figure that the temperature increased from 298 K to 373 K for both the adsorbents during the desorption step.

It takes some time before the temperature starts increasing during the desorption step, as seen from Figure 2.4a. This is because this analysis is shown at the channel exit ($z = L$). It takes time before the steam reaches the channel exit, and by keeping the steam velocity at 0.04 m/s (for MIL-101(Cr)-PEI-800) and 0.1 m/s (for mmen-Mg_2(dobpdc)), it is ensured that the steam concentration front is always behind the desorbed CO_2 front. This minimizes the use of steam at the expense of having a longer desorption time, rolling the CO_2 along the channel, increasing its concentration as it proceeds.

Figure 2.4b shows the variation of the amount of CO_2 (in moles) adsorbed per channel for both the adsorbents. The total amount of CO_2 captured per channel per cycle by mmen-Mg_2(dobpdc) is higher than by MIL-101(Cr)-PEI-800 since mmen-Mg_2(dobpdc) has a higher equilibrium capacity than MIL-101(Cr)-PEI-800 at ambient conditions. This can be further confirmed from Figure 2.4b, which shows that the initial amount of CO_2 adsorbed for mmen-Mg_2(dobpdc) is almost triple that of MIL-101(Cr)-PEI-800, and mmen-Mg_2(dobpdc) shows a steeper slope at the end of this step.

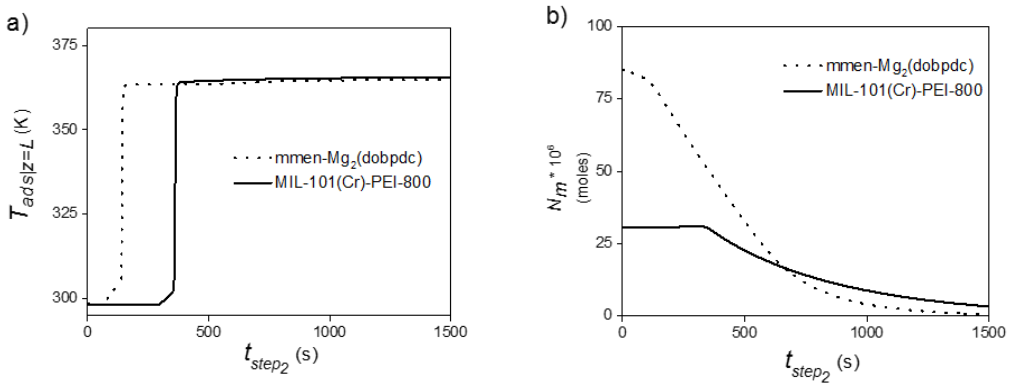

Figure 2.4. Variation of a) the adsorbent exit temperature and b) the total CO_2 moles adsorbed per channel during the desorption step.

2.5 Estimation of Energy Requirements

To estimate the feasibility of the DAC process through the proposed TVSA model, it is essential to analyze the energy requirements of the process. The air is assumed to be moved via an electrically driven fan during the adsorption step (Step 1). Higher air flow rates cause a larger pressure drop across the channel and hence a higher load on the fan. The energy requirement of the fan (E_1) is the product of pressure drop required across the channel and the net volumetric air flow during the adsorption step. During the evacuation step (Step 2), energy is required by the vacuum pump (E_5) to decrease the pressure inside the channel from 1 atm to 0.2 atm. During the desorption step (Step 4), energy is required to provide sensible heat to the adsorbent (E_2), the monolithic wall (E_3) for desired temperature rise, and to desorb adsorbed CO_2 molecules (E_4). Energy is also embodied in the uncondensed steam (E_6) that exits the monolith channel during the desorption step. During the cooling step (Step 5), vacuum pumps are used (E_5) to lower down the partial pressure of water vapor inside the channel.

The sum of these energies (E_1+…+E_6) gives the total energy used by the system. The theoretical minimum energy requirement of the system is defined by the sum of E_1 to E_5, as the steam that is uncondensed is effectively wasted unless this low temperature enthalpy can be recovered.

Table 2.5 describes the equations used to estimate the energy requirements. *E* refers to the energy required in joules per mole of CO_2 removed. Q_{step_1} and t_{step_1} are the gas flow rate and time taken during Step 1 of the TVSA cycle and m_{ads} and m_{wall} are the mass of the adsorbent and monolithic wall per channel, respectively. P_1 is the initial pressure and V_2 and V_1 are the final and initial volume, respectively, during the vacuum swing steps (Evacuation and cooling steps). L' is the latent heat of low grade. We assume a pump efficiency of 85% in this analysis.

Table 2.5: Energy requirements for the TVSA model.

Components	Energy requirements (in Joules per mole CO_2 captured)
Electrical energy for blowers	$E_1 = \Delta P Q_{step_1} t_{step_1} / N_m$
Adsorbent sensible heat	$E_2 = \frac{m_{ads} C_{p.ads}}{L N_m} \int_{t=t_{step_4}}^{t_{step_5}} \left(\int_{z=0}^{L} \frac{dT_{ads}}{dt} dz \right) dt$
Monolithic wall sensible heat	$E_3 = \frac{m_{wall} C_{p,wall}}{L N_m} \int_{t=t_{step_4}}^{t_{step_5}} \left(\int_{z=0}^{L} \frac{dT_{wall}}{dt} dz \right) dt$
CO_2 desorption heat	$E_4 = \Delta H$
Electrical energy for vacuum pump	$E_5 = -\frac{P_1 V_1^{\gamma}}{N_m} \frac{\left(V_2^{1-\gamma} - V_1^{1-\gamma} \right)}{1-\gamma}$
Energy in uncondensed steam	$E_6 = \frac{2\pi L'}{N_m} \int_{t=t_{step_4}}^{t_{step_5}} \left(\int_{r=0}^{R_1} v_{step_4} r C_{H_2O}(L) dr \right) dt$

We use a "primary combustion energy" basis where all the energy requirements are moved back through a supply chain into a fossil energy source in the ground that would correspond to the final delivered energy for the process. This allows us to put electricity, steam and fuel use on a common basis and to compare them to the energy available when combusting carbon. In order for the latter comparison to be made, a representative form of fossil carbon has to be chosen relative to its composition, or state of reduction. Following,[17] we choose CH_2 as the basis for comparison with a heat of combustion of 0.45 (MJ/mole carbon as CH_2). This provides an upper bound on the combustion energy we should expend to capture a mole of CO_2.

For simplicity, we assume the steam would come from a steam turbine system running from 753 K and 65 bar to 408 K and 1.1 bar, which are reasonable conditions at the inlet of a high pressure and condensing steam turbine respectively. The steam for the desorption would be extracted before the remaining steam is sent to a condensing turbine. Thus, we consider the difference in electricity generation between two systems, one with and one without a condensing turbine, as the energy penalty of the air capture system. The decreased electricity can be translated to a fuel use by using an efficiency of electricity generation. A scale up factor [82] of 3.14 and 1.20 have been used to convert electrical and thermal energy respectively to primary combustion energy. Table 2.6 below gives the assumptions for the steam system, additional efficiency factors and energy requirements for the system.

Table 2.6: Assumptions for the steam system, efficiency factors and primary combustion energy requirements.

Steam inlet condition	753 K and 65 bar
Steam outlet condition	408 K and 1.1 bar
Boiler efficiency (%)	85
Turbine isentropic efficiency (%)	70
Loss of electricity generation per kg of steam	0.14 MJ/hr

Primary Combustion Energy Requirements (MJ/mole)	MIL-101(Cr)-PEI-800	mmen-Mg_2(dobpdc)
Energy consumed by Blowers (E_1)	0.1	0.09
Adsorbent sensible heat (E_2)	0.006	0.002
Monolithic wall sensible heat (E_3)	0.022	0.006
Energy due to CO_2 desorption (E_4)	0.006	0.005

Table 2.6 continued

Energy consumed by vacuum pumps (E_5)	0.010	0.010
Minimum Primary Combustion Energy requirements (E_1+…+E_5)	0.145	0.113
Energy due to uncondensed steam (E_6)	0.080	0.045
Net Primary Combustion Energy used (E_1+…+ E_6)	0.225	0.158

Table 2.6 presents an analysis of the energy requirements for the MIL-101(Cr)-PEI-800 and mmen-Mg_2(dobpdc) adsorbents. It can be noted that the energy requirement for the MIL-101(Cr)-PEI-800 is higher than that for the mmen-Mg_2(dobpdc) adsorbent. Here, the energy requirements for these two materials are evaluated by comparing them with the minimum theoretical energy use: the energy required for unmixing of two ideal gases, inert and CO_2, is around 0.02 MJ/mole for CO_2 at atmospheric concentrations.[31] A benchmark for the maximum energy use that would lead to a net negative CO_2 balance in the atmosphere is the 0.45 kJ/mol given earlier. It can be seen from Table 2.6 that the minimum primary combustion energy requirements for the MIL-101(Cr)-PEI-800 and mmen-Mg_2(dobpdc) adsorbents are around 0.145 MJ/mole and 0.113 MJ/mole, respectively. We assume 100% thermal efficiency to calculate these values. However, for a process with a thermal efficiency of 85%, the minimum primary combustion energy requirements for the

MIL-101(Cr)-PEI-800 and mmen-Mg_2(dobpdc) adsorbents are around 0.150 MJ/mole and 0.125 MJ/mole, respectively. This means that this process does require less primary combustion energy than the primary combustion energy available in the carbon using these process conditions and assumptions on the form of the carbon fuel. The energy loss from the channel boundary has been assumed to be negligible compared to other energy consumption terms.

2.6 Estimation of Cost

The total cost of DAC can be split into operating and capital costs. To place these on the same basis, we will use the normal procedure of finding an annualized capital cost (annualized over 10 years lifetime for the monolith, blower and vacuum pump and 1-3 years lifetime for the adsorbents), and use a basis of 1 tonne of CO_2 captured. We assume a 1.1 × 1.1 × 0.3 m contactor, which results in 750,000 channels per contactor (for 400-cpsi monolith). The capital cost consists of mainly adsorbent, monolith, fans and vacuum pump costs.

Table 2.7 describes the equations used to estimate each of these costs. C_1 - C_3 are the operating cost requirements and C_4 - C_7 are the capital cost requirements of the system. Q_{step_1} and Q_{step_4} are the gas flow rate during step 1 (adsorption step) and step 4 (desorption step) of the TVSA cycle, respectively. t_{step_1}, t_{step_4} and t_{cycle} are the time taken (in seconds) during step 1, step 4 and the entire TVSA cycle, respectively, and t_{yr} is the time (in seconds) in 1 year, assuming 330 days of operation per year. C_E ($/kW-hr), C_{st} ($ per unit weight of steam), *and* C_{ads} ($ per unit weight of adsorbent) are the purchase costs of electricity, steam and adsorbent, respectively. Note that the adsorbent cost (C_5) is not factored up as a part

of installed capital cost. $C_{monolith}$ ($ per cubic inch of monolith substrate), C_B ($), C_{Vac} ($) and C_M ($) are the bare module costs of the monoliths, blowers, pumps and electric motor, respectively. $V_{monolith}$ and m_{ads} are the volume of one monolithic channel and mass of the adsorbent per channel, respectively. N_t is the amount of CO_2 removed (in tonnes) per channel per cycle and $N_{yr,i}$ is the lifetime of the individual components. We assume that the steam is provided from a main steam system and there is no capital recovery charge for the steam use. This was done to avoid the complexity of designing and building a standalone combined heat and power (CHP) system or another means for providing the steam to the plant, such as a solar thermal cycle.

Table 2.7: Cost calculations for the TVSA model.

Components	Operating Cost (dollars per tonne)
Fan	$C_1 = \Delta P Q_{step_1} t_{step_1} C_E / N_t$
Steam	$C_2 = Q_{step_4} t_{step_4} \rho_{st} C_{st} / N_t$
Vacuum Pump	$C_3 = \frac{E_5 N_m}{N_t}$

Table 2.7 continued

Components	Capital Cost (dollars per tonne)
Monolith	$C_4 = V_{monoltih} \frac{C_{Monolith} t_{cycle}}{N_t N_{yr_1} t_{yr}}$
Adsorbent	$C_5 = m_{ads} \frac{C_{ads} t_{cycle}}{N_t N_{yr_2} t_{yr}}$
Blower	$C_6 = \frac{C_B t_{cycle}}{N_t N_{yr_3} t_{yr}}$
Vacuum pump	$C_7 = \frac{\left(C_{vac} + C_M\right) t_{cycle}}{N_t N_{yr_4} t_{yr}}$

The steam operating cost is estimated from the lost power production in a steam turbine system because air capture has been added to the turbine system. In our case, we assume that the turbine system is not increased in size and that steam is diverted from making power in the condensing turbine. Therefore we included the cost of the lost power because the steam could not be put through this final expansion step. The cost of the electricity for the fans and vacuum pumps is taken to be the same value as that for the lost generating capacity.

The cost of the adsorbent and its lifetime are two additional parameters that affect the overall cost of the DAC process. We assume the purchase cost (C_{ads}) of MIL-101(Cr)-PEI-800 and mmen-Mg_2(dobpdc) to be \$15/kg and \$50/kg, respectively [83]. This assumes the bulk price of reagents with 100% product yield and includes raw material, labor, maintenance and utility costs required for the adsorbent production. The cost coefficient may increase or decrease from the value assumed above if the adsorbent synthesis has lower yield or is made more efficiently. To account for this uncertainty, we perform a sensitivity analysis on the overall DAC cost, fixing the bounds for the adsorbent's cost coefficients to \$7-30 per kg for MIL-101(Cr)-PEI-800 and \$25-100 per kg for mmen-Mg_2(dobpdc). The lower bound corresponds to twice the adsorbent synthesis efficiency and the upper bound corresponds to 50% product yield for both the adsorbents. The lifetime of the adsorbent (N_{yr2}) is assumed to vary between 1 to 3 years for the sensitivity analysis.

Table 2.8 summarizes the contribution of each component that contributes to the total cost for the DAC process. The adsorbent capital cost, which includes the adsorbent's purchase cost and the lifetime of the adsorbent, is the parameter to which the total cost is most sensitive.

Table 2.8: Cost components of the TVSA model for DAC

Cost components	Value ($/tonne) (MIL-101(Cr)-PEI-800)	Value ($/tonne) (mmen-$Mg_2$(dobpdc))
Blowers (C_1)	24.0	20.0
Steam (C_2)	15.0	5.0
Vacuum pump Opex(C_3)	2.0	1.0
Monolith (C_4)	5.0	4.0
Adsorbent (C_5)	5.0-70.0	10.0-140.0
Blower (C_6)	15.0	10.0
Vacuum pump Capex (C_7)	9.0	10.0
Total cost	75.0-140.0	60.0-190.0

2.7 Conclusion

In this chapter, numerical modeling and simulation was used to analyze the performance of a TVSA process for DAC using a monolith structure coated with a MOF film. For the monolith structure, a wall thickness of 50 microns (corresponding to 400 cpsi) and a film thickness of 60 microns were chosen as design parameters. The TVSA process comprised five steps: adsorption, evacuation, pressurization, desorption and cooling.

The energy requirements for the DAC process were determined. The minimum energy requirement for both the adsorbents, (0.19 MJ/mole for MIL-101(Cr)-PEI-800 and 0.14 MJ/mole for mmen-Mg_2(dobpdc)), is less than the energy associated with the heat of combustion that generated the CO_2 (0.45 MJ/mole). The energy requirements can be further reduced if we are able to experimentally grow thicker MOF films and have thinner monolith walls structurally stable. However, thicker MOF layer might end up with higher mass transfer resistance which may increase the cycle time and hence the overall cost of DAC.

We have also performed a detailed economic analysis for the Direct Air Capture. Various components for operating and capital costs were identified and the purchase cost of the adsorbent was identified as the key uncertain parameters in the TVSA model. It was found that the total cost for MIL-101(Cr)-PEI-800 is around $ 95-160 per tonne of CO_2 captured if we consider the lifetime of adsorbent between 1 to 3 years. On the other hand, the net cost formmen-Mg_2(dobpdc) is around $ 75-200 per tonne of CO_2 captured for same range of adsorbent's lifetime.

Growing thicker adsorbent films and thinner monolithic walls can further reduce the net energy requirement. Other ways to reduce these energy requirements is to look for better adsorbent candidates with higher equilibrium capacities at the ambient CO_2 concentration. Finally, in this analysis we assume that the steam was raised using traditional fuels; if the steam and electricity were provided via a solar thermal cycle (primary solar energy) the net sequestration potential of the process, the difference between the CO_2 captured versus the CO_2 spent in capturing it, could be further improved. Further optimization study with additional parameters such as channel length, film and wall thickness needs to be performed on the proposed model and recovery of heat from the steam through heat integration will further improve the energy and cost estimates for the process. Diffusivity of CO_2 inside the adsorbent also needs to be determined experimentally for more accurate analysis. Checking thermal stability of the MOFs in the long-term cycle test (for determining lifetime of the adsorbent) is also a key issue which needs to be addressed in future studies.

CHAPTER 3. DIRECT AIR CAPTURE: TECHNO-ECONOMIC ANALYSIS

Based on the methodology developed for DAC in the previous chapter, I have performed detailed sensitivity analysis to study the energetics and techno-economic in this chapter to analyze the DAC process using solid adsorbents with parametric ranges on key properties that impact system performance and costs.

3.1 Cost and Energy components

For a generic DAC process using solid adsorbents, the two main steps are adsorption and desorption. In order to perform a high-level techno-economic study on a DAC process, I have identified the major cost and energy components involved in the CO_2 capture model. Figure 3.1 shows the schematic of a typical DAC process along with cost and energy components involved in the adsorption and the desorption step. During the adsorption step, the major cost components are the blower, adsorbent and contactor capital costs and electricity operating cost to operate the blowers. During the desorption step the cost components are the vacuum pump capital cost and electricity operating cost to operate the vacuum pumps. The energy requirements during the adsorption step is due to electrical energy to operate the blowers, and those during the desorption step are the thermal energy to heat the system and electrical energy to operate the vacuum pumps.

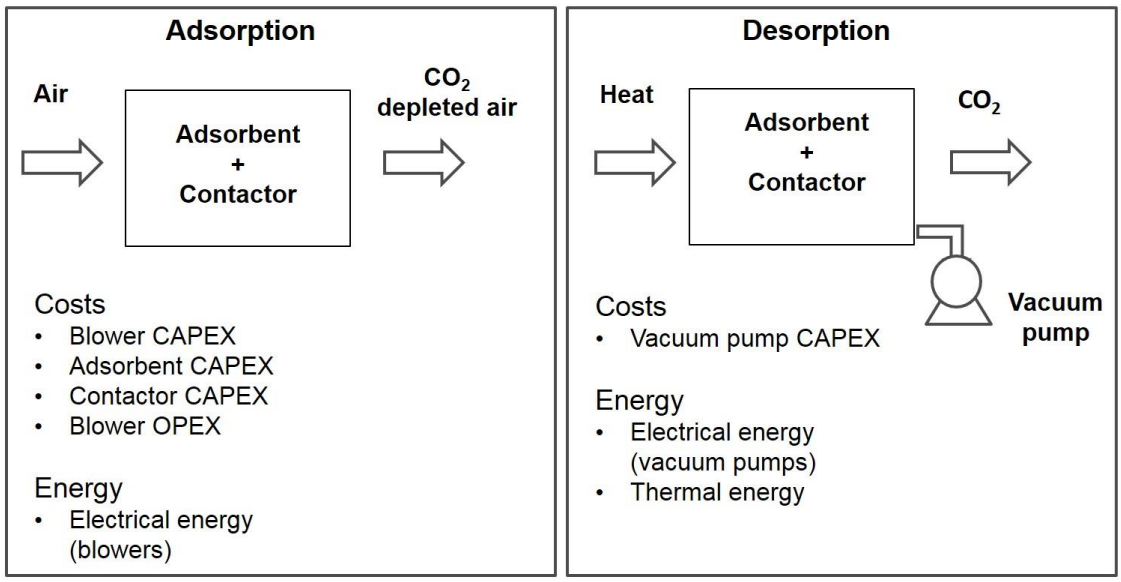

Figure 3.1: Schematic of the DAC process

3.2 Analysis approach

In order to perform a detailed sensitivity analysis on the techno-economics of this DAC process, I have followed a hierarchical approach in varying the model parameters. Figure 3.2 depicts the strategy adopted in performing the analysis. Initially, level 1 analysis is performed, in which the desorption pressure and desorption final temperature is varied in the model which has direct influence on the desorption time, vacuum operating cost and the desorption thermal cost. Utilizing the information gathered from above analysis, level 2 analysis is performed, in which the model is simulated with variation in inlet air velocity and mass transfer coefficient. Each of the instances of level 2 analysis (inlet air velocity and mass transfer coefficient) has the same set of variations of level 1 analysis (desorption pressure and desorption final temperature). The level 2 analysis influences the adsorption time, blower operating cost and pressure drop across the contactor. In the level 3 analysis, adsorbent CO_2 capacity, ratio of H_2O:CO_2 and CO_2 swing fraction in the model are varied.

The ratio of H_2O:CO_2 can affect the system performance since if the water is completely desorbed water from the system each cycle, the parasitic load can be very high based on reasonable estimates of water co-adsorption.

Level 3 analysis influences the total amount of CO_2 captured, the heat of adsorption and the desorption time. Finally, level 4 analysis incorporates variation in contactor: adsorbent ratio, the adsorbent purchase cost and the lifetime of the adsorbent. Level 4 analysis has influence on the capital cost of the adsorbent and the contactor. The level 4 analysis contains the data from level 3 analysis, which contains the data from level 2 analysis, which contain the data from level 1 analysis.

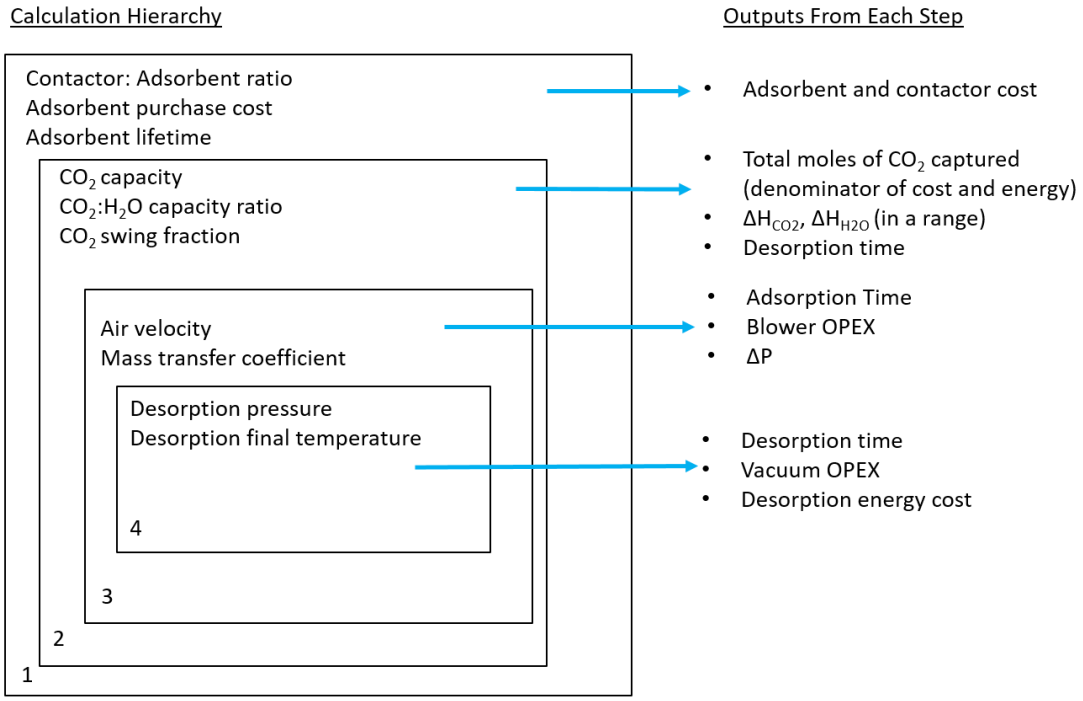

Figure 3.2: Cost and Energy analysis approach

The strategy described above assumes certain bounds on model parameters. I have defined two extreme bounds, worst and best case scenario for the DAC process. The worst case assumes an adsorbent with the shortest lifetime and the most expensive synthesis, lowest swing fraction during the adsorption – desorption step, highest desorption pressure and temperature and the highest H_2O:CO_2 ratio. The best case represents the ideal situation which is desired where all the parameters operate in their prime capacity such that the lowest cost and energy is invested in running the DAC process. The complete analysis requires examining 1300 scenarios with different combination of parameters provided in Table 3.1. The table lists the model parameters with their respective bounds that have been used to perform the hierarchical analysis as discussed above. The table shows bounds on the input parameters which are fixed using the predefined range of the bounds. Bounds have also been placed on certain outputs as listed in the table. These outputs are constrained in the given range. We neglect any data point which falls beyond these ranges as being an infeasible combination of parameters for the operation. The outputs which are not constraint by any ranges are the capital and operating costs and thermal and electrical energy requirements.

Table 3.1: Range on model inputs and outputs

Parameter	**Lower bound**	**Upper bound**	**Units**
Inputs (Predefined range)			
Contactor : Adsorbent Ratio (Mass)	4.0 : 1.0	1:10	-
Adsorbent Purchase Cost	15	100	$/kg
Sorbent Total Capacity	0.5	1.5	mol/kg
Desorption Swing Capacity	0.75 SC_{max}	0.9 SC_{max}	
CO_2: Water Ratio	1:2	1:40	
Velocity	1	5	m/s
Desorption Pressure	0.2	1	bar
Desorption Final Temperature	340	373	K
Heat of Adsorption (CO_2)	40	90	kJ/mole
Outputs (Constraint with range)			
Adsorption Time	8	50	min
Desorption Time	7	35	min
Mass Transfer Coefficient	0.01	0.1	1/s
Pressure drop	300	1400	Pa

3.3 Cost and Energy Estimates

The cost and energy estimates for the DAC process are analyzed utilizing the strategy discussed in the previous section. Table 3.2 lists the cost and energy for the level 4 analysis with different contactor: adsorbent ratio. This analysis includes the results from all the higher level analysis in addition to level 4 analysis. It can be seen from the table that lower contactor: adsorbent ratio results in decrease in thermal and electrical energy requirements of the DAC process. This is because, lower the ratio of contactor: adsorbent, lesser the thermal energy is required for the sensible heat of the contactor. In addition, for a fixed contactor volume, lower contactor: adsorbent ratio results in higher mass of adsorbent, hence a higher amount of CO_2 captured. This results in decrease of electrical energy requirements as the energy is defined with respect to amount of CO_2 captured.

It can be seen from Table 3.2 that lowering the ratio of contactor: adsorbent does not have substantial effect on the cost of the DAC process, particularly for the lower bound. The reason is at the lower bound each of the cost components are low so the overall cost is less sensitive to the change in contactor to adsorbent ratio. At the upper bound, decreasing the contactor to adsorbent ratio initially lowers the costs and then increases it. This is because, there is a tradeoff between the amount of CO2 captured and the adsorbent capital cost. Lowering the contactor to adsorbent ratio increases the amount of CO_2 captured. Hence the cost per tonne of CO2 captured decreases. However, decrease in the ratio means higher mass of the adsorbent, hence higher adsorbent cost.

Table 3.2: Cost and Energy estimates of the DAC process

Contactor:Adsorbent = 4:1			**Contactor:Adsorbent = 1:1**			**Contactor:Adsorbent =0.1:1**		
Lower	Upper	Units	Lower	Upper	Units	Lower	Upper	Units
Thermal Energy								
0.20	0.85	MJ/mole	0.15	0.40	MJ/mole	0.08	0.28	MJ/mole
4.6	19.3	GJ/tCO_2	3.5	9.16	GJ/tCO_2	1.85	6.5	GJ/tCO_2
1239	5367	kW-hr/tCO_2	982	2549	kW-hr/tCO_2	514	1810	kW-hr/tCO_2
Electrical Energy								
0.005	0.167	MJ/mole	0.004	0.108	MJ/mole	0.003	0.089	MJ/mole
0.12	3.79	GJ/tCO_2	0.09	2.46	GJ/tCO_2	0.08	2.03	GJ/tCO_2
35	1055	kW-hr/tCO_2	25	685	kW-hr/tCO_2	20	565	kW-hr/tCO_2
Cost								
18	1030	$/$tCO_2$	14	1015	$/$tCO_2$	14	1065	$/$tCO_2$

The parasitic load on the system is defined as the unwanted energy that is needed for the CO_2 capture process. This is the heat put into the system that is not used to desorb the CO_2 over the total heat that is added to the system. It comprises of sensible heat of contactor and the adsorbent in order to heat them up to the temperature of the surrounding. With the decrease in the contactor to adsorbent ratio, the parasitic load on the system is expected to decrease because of less energy (per mole of CO_2) spent to account for the sensible heat of the contactor and the adsorbent. Table 3.3 lists the parasitic load on the system with the decrease in the contactor to adsorbent ratio. It can be seen from the table that the parasitic load decreases as the ratio of contactor to adsorbent is reduced.

Table 3.3: Parasitic load requirements for different contactor: adsorbent ratio

Contactor:Adsorbent = 4:1			**Contactor:Adsorbent = 1:1**			**Contactor:Adsorbent =0.1:1**		
Lower	Upper	Units	Lower	Upper	Units	Lower	Upper	Units
0.15	0.81	MJ/mole	0.10	0.32	MJ/mole	0.04	0.16	MJ/mole

The DAC process has different cost components as described in Section 3.1. Figure 3.3 shows the contribution of these cost components for the best and worst case scenarios. It can be seen from the figure that for the best case scenario, the cost is dominated by the adsorbent and vacuum pump capital cost and steam operating cost. However for the worst case scenario, the cost is primarily dominated by the adsorbent capital cost.

Figure 3.3: Cost components of the DAC process for best and worst case scenario

The upper and lower bounds obtained through the above analysis covers the entire spectrum of estimates available in the literature. Figure 3.4 compares the bounds on energy requirements in the present analysis with the comparison made by Bauer et. al [84]. The analysis by Bauer et.al includes work from Baciocchi [20], Stolaroff [22], Keith [85], Zeman [18], Lackner [86], Socolow [31] and Goeppert [87]. It can be seen from the figure that the analysis presented in this chapter covers the entire range of analysis performed in the existing literature.

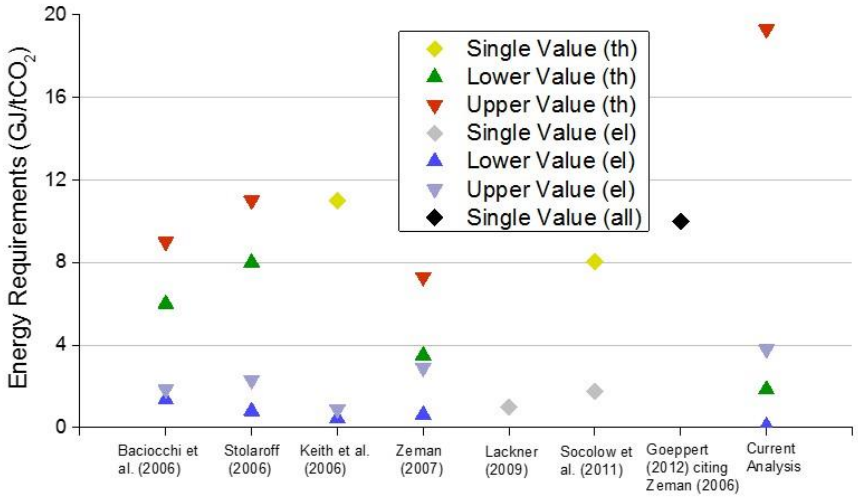

Figure 3.4: Comparison of the analysis with the existing literature

Between these best and the worst cases, lies the mid-range bounds which are practically possible with the present state of the research. Techno-economic analysis through mid-range values provide a more reasonable estimates with respect to current advancement in the DAC process through solid adsorbents. Table 3.4 lists the values of parameters used while simulating the mid-range cases.

Table 3.4: Parameter values for mid-range estimates

Parameters	**Units**
Adsorbent Purchase Cost ($/kg)	50
Adsorbent Lifetime (years)	0.5
Sorbent Total Capacity (mol/kg)	1
Desorption Swing Capacity	0.8 SC_{max}
Contactor : Adsorbent ratio	0.1:1 - 1:1
Desorption Pressure (bar)	0.5
Final Desorption Temperature (K)	360

Utilizing the information provided in Table 3.4, I have listed the cost and energy requirements of the DAC process through mid-range estimates (Mid-low and Mid-high corresponds to lower and upper bounds on contactor to adsorbent ratio) in Table 3.5. It can

be seen from the table that energy requirement is dominated by the thermal cost of the system.

Table 3.5: Cost and Energy requirements of the DAC process for the mid-range estimates

Thermal Energy		
Mid-low	Mid-high	
0.15	0.21	MJ/mole
3.4	4.8	GJ/tCO_2
950	1326	kW-hr/tCO_2
Electrical Energy		
0.024	0.049	MJ/mole
0.55	1.12	GJ/tCO_2
153	312	kW-hr/tCO_2
Cost		
86	221	\$/tCO_2

Table 3.6 lists the contribution of the cost components of the DAC process for mid-range cases. It can be seen from the table that the adsorbent capital cost is the major contributor. Hence, selecting a cheaper adsorbent with high capacity for CO_2 adsorption and long lifetime will help further bring down the overall cost of the DAC process.

Table 3.6: Cost components estimates of the DAC process for mid-range cases

Cost	Mid-Low ($/tCO$_2$)	Mid-High ($/tCO$_2$)
Adsorbent CAPEX	70	186
Adsorption OPEX	9	19
Blower CAPEX	2	6
Vacuum pump CAPEX	1.5	5
Steam OPEX	2.2	3
Monolith CAPEX	0.7	2.1
Vacuum pump OPEX	0.19	0.24
Total Cost	85.6	221.3

3.4 Effect of Water Co-adsorption

Water co-adsorption can affect the energetics of the DAC process because of the sensible heat due to water co-adsorption. In order to study the effect of H_2O:CO_2 ratio, a sensitivity analysis is performed on the model by varying the ratio from 2:1 to 40:1 keeping contactor:adsorbent ratio at 0.1:1. Table 3.7 lists the best and the worst case thermal energy values with variation in the H_2O:CO_2 ratio. It can be seen from the table that increase in the H_2O:CO_2 ratio increases the thermal energy for both the cases. This is because,

increasing the ratio increases the sensible heat requirement due to water co-adsorption and hence the overall thermal energy requirements.

Table 3.7: Effect of $H_2O:CO_2$ ratio on DAC energetics

$H_2O:CO_2$	Best Case (MJ/mole)	Worst Case(MJ/mole)
2:1	0.08	0.17
10:1	0.10	0.20
20:1	0.12	0.25
40:1	0.14	0.28

3.5 Carbon Footprint

In order to analyze the impact of DAC process on the environment, I have computed the CO_2 emissions assuming the electricity generation is through solar, wind, natural gas (NG), as well as coal and thermal (steam) generation through NG or coal. Table 3.8 lists the emissions values for the different cases. It can be seen from the table that the CO_2 emissions caused due to steam is much higher as compared to electricity. This is due to higher energy consumption by the steam as compared to the electricity.

Table 3.8: Energy emissions of the DAC process for electricity and steam

Electricity (MtCO2e/yr)	**Best case**	**Mid low**	**Mid high**	**Worst case**
Solar	0.0011	0.0084	0.0171	0.0579
Wind	0.0003	0.0022	0.0046	0.0158
NG	0.0098	0.0749	0.1527	0.5163
Coal	0.0164	0.1253	0.2557	0.8641
Steam (MtCO2e/yr)	**Best case**	**Mid high**	**Mid low**	**Worst case**
NG	0.1169	0.2156	0.3010	1.1815
Coal	0.1720	0.3173	0.4428	1.7384

3.6 Flux and Intensity estimates

So far I have analyzed the DAC process based on energy, cost and emissions. It would be interesting to analyze the CO_2 flux associated with the DAC process and energy intensity associated with it. This will help to compare energy statistics of the DAC process with a tropical forest. In order to analyze such metric, Leaf Area Index (LAI) is defined as provided in eq. 4.

$$\text{LAI} = \frac{\text{leaf surface area } (\text{m}^2)}{\text{ground area } (\text{m}^2)} \quad (4)$$

A tropical evergreen broadleaf has a LAI of 5 m^2 leaf/m^2 ground with CO_2 uptake rate of 8 μmoles per second per m^2 of leaf area or steady state rate of 20 μmoles per second per m^2 of ground [88]. A metric similar to LAI can be used which computes the ratio of monolith surface area to the ground area of the CO_2 capture plant. Another comparison metric is the energy intensity which is calculated in Watts per m^2 of ground area. For a tropical forest, the average energy intensity is around 450 W/m^2-ground during photosynthesis [88]. Table 3.9 lists the CO_2 flux and energy intensity requirements of the DAC process. The analysis assumes monoliths ground area of 10 x 0.3 m^2 stacked up to 10 m height with the total DAC plant area of 400 m^2 which has a capture density of 40,000 tCO_2 per acre per year. It can be seen from the table that the DAC process has a higher flux and lower energy intensity for all the cases as compared to a tropical tree.

Table 3.9: Flux and intensity of the DAC process

	Units	Best case	Mid-low	Mid-high	Worst case
Flux	$\frac{\mu moles}{s-m^2 surface}$	51	30	22	7
	$\frac{\mu moles}{s-m^2 ground}$	984	564	427	143
Electrical energy intensity		4	18	28	32
Thermal energy intensity	$\frac{W}{m^2 ground}$	105	113	120	159
Primary energy intensity		138	192	231	291

3.7 Conclusion

CO_2 capture from the ambient air can have an economic pathway if the design and operating parameters are chosen judiciously. The analysis presented in this chapter provides a comprehensive study on the range of parameters for the energetics and techno-economic assessment of DAC through solid adsorbents. A hierarchical approach was followed to vary the parameters sequentially. The ranges on the parameters were selected such that a best case, mid-range and worst case scenarios can be represented for the analysis.

The cost analysis shows the economics of the DAC process vary between \$14 – 1065 per tCO_2 if the model parameters are varied from best to worst case scenario with mid-range cost estimates of \$86 – 221 per tCO_2. The energy range for the DAC process is 0.08 – 0.85 MJ per mole of CO_2 captures with mid-range energy estimates of 0.15 – 0.21 MJ per mole of CO_2 captured. CO_2 emissions due to the DAC process was also calculated in this chapter. It was found that the emissions due to steam was much higher compared to the emissions caused due to the electricity. Finally, CO_2 flux and energy intensity was analyzed for the DAC process and compared with the tropical trees. It was found that the DAC process has higher flux and utilizes lower intensity as compared to tropical trees.

The adsorbent purchase cost is found the most sensitive parameter in this analysis, which is the key for energy reduction. A cheaper adsorbent with high CO_2 capacity and high lifetime is desired for further improvement in energetics and cost of the DAC process through solid adsorbents.

CHAPTER 4. CO_2 CAPTURE FROM ENCLOSED SPACES

Globally, energy use for enclosed environments, such as the building sector, account for more than 30% of the total CO_2 emissions [89] and the demand is constantly increasing due to increasing population, urbanization and economic development. Rapid growth in global energy consumption has raised concern on the environmental impacts such as ozone layer depletion and climate change. The energy demands in the building sector calls for strategic measures to develop energy efficient technologies.

In this chapter, I have utilized the methodologies developed in the previous chapters to model the capture of CO_2 from enclosed space such as buildings. CO_2 removal from buildings offers the advantage of a greater driving force for separation exploiting the higher CO_2 concentration compared to ambient air (~ 400 ppm). Further, air inside buildings is cleaner compared to flue gases. However, removal of CO_2 from buildings is more challenging than CO_2 capture from flue gas due to the low concentration gradient driving force.

4.1 Introduction and Literature Review

Fossil energy use and its impact on global warming is a major concern worldwide. The rising levels of CO_2 concentration in the atmosphere poses a serious threat to climate stability. In most developed countries, the building sector is the largest consumer of total energy, which is even larger than the industry and transportation sectors combined. For example, the energy consumption from buildings in the United States and European Union is between 20 – 40 % of the total energy usage [90-91] resulting in approximately 1000 Tg of

carbon dioxide released in the atmosphere per year. Further, the energy demand is steadily increasing in this sector due to population and economic growth and shifts in climate [92]. Hence, reducing the carbon footprint of buildings by increasing their energy efficiency should be a priority to mitigate future anthropogenic emissions.

Several energy saving strategies have been proposed in the existing literature [93-97]. One such strategy is to optimize the usage of HVAC systems inside buildings [98-100]. HVAC consumption accounts for half the energy use in the building sector and one fifth of the total national energy use in the developed countries [101]. Primary reason for HVAC to be the largest consumer is the need to maintain a comfortable and workable environment inside buildings.

Specific air quality standards needs to be maintained inside buildings to ensure that the air does not possess threat to health of people inside the enclosed space. In particular, controlling CO_2, O_2 and humidity level inside buildings is of critical importance to regulate the air quality. The U.S. Occupational Safety and Health Administration (OSHA) defines critical O_2 concentration inside enclosed space as 19.5%. It states that any atmosphere with an oxygen level below 19.5% is oxygen deficient and possess immediate danger to life and health. Studies have shown health risks associated with high CO_2 concentration (>0.5%) [102-103]. People may suffer headache, nausea, fatigue and listlessness when exposed to high CO_2 concentration for prolonged duration. Regulating humidity level inside buildings is also of critical importance. It is recommended to maintain the indoor relative humidity level between 30 – 60%. Humidity level less than 30% can cause dryness of skin and respiratory discomfort while over 60% humidity can promote growth of molds and fungi [104-105].

Better air quality leads to improved human productivity [106]. The conventional method of regulating the air quality is through ventilation. However, such techniques are not energy efficient for enclosed spaces because significant energy is spent in conditioning the outside air. There have been limited studies on artificial CO_2 and humidity control inside buildings. A study by Lee et al. [107] proposes removal of CO_2 from indoor air through electric swing adsorption using carbon monoliths as adsorbing agents. Their work supports that regulating CO_2 concentration is an important factor in energy consumption.

Recently, there has been an increased interest in implementing novel ventilation strategies inside enclosed environments[108-111]. Cui et al. [112] proposed a hybrid air treatment system which consists of an ozone based oxidation process and an air scrubbing device. Their system shows improvement in performance compared to conventional ventilation systems. However, their system has deployment limitations due to large footprint required for the air treatment system. Recently Thakkar et al. [113] fabricated three dimensional (3D)- printed 13X zeolite monoliths and reported their use in CO_2 removal from air in enclosed environments. The 3D monolith showed mechanical stability that can prevent attrition and dusting issues, and can be used as a cost effective approach for gas separation processes.

The studies described above provide useful insights into improving energy efficiency and air quality inside buildings. However, there has been limited research on CO_2 removal techniques inside enclosed environments. In addition, previous research focuses on controlling only one of the components of the air (CO_2, O_2 or Humidity). This chapter aims to bridge this gap by controlling all the three air components through a novel air composition control and reduced ventilation strategy. This strategy is based on concentration swing adsorption of CO_2 on 3D zeolite 13X monoliths and temperature

swing adsorption of water on silica gel packed beds. The system is specifically designed to minimize the rate of external ventilation, which is targeted to control the oxygen level inside the room.

4.2 Process Description

4.2.1 System *Design*

I propose a multi-component, multi bed adsorption system, which aims at controlling CO_2, O_2 and humidity level inside a room of a building. Figure 3.1 depicts the schematic of the process. I term this "enclosed air capture" to reflect the main purpose of the system which is to capture CO_2 from the enclosed air and reject it to outside the building. An office room is assumed with people occupancy during office hours (9 AM – 5 PM). The concentration of CO_2 inside the room increases due to human metabolism. The CO_2 rich air from the room is fed to the dehumidification unit (silica gel packed bed) which removes moisture from the feed air. This unit is necessary since the adsorbent (zeolite 13X) used downstream (CO_2 removal system) shows a decay in the CO_2 adsorption capacity when exposed to humid conditions [114]. The product from the dehumidification unit is supplied to the CO_2 removal system. The CO_2 removal system consists of parallel honeycomb 3D printed zeolite 13X monoliths. The size of the monolithic structure is tuned according to the volume of the room, adsorption capacity of the adsorbent material, and the number of people present inside the room. The monoliths adsorbs the CO_2, and the dry air depleted in CO_2 is recycled back to the room.

The external ventilation rate is tuned to control the oxygen level inside the room. The room humidity level will drop due to continuous removal of humidity from the dehumidification

unit. Hence, there is another saturated dehumidification unit, which maintains the humidity level inside the room through regeneration. The proposed strategy ensures that the CO_2, O_2 and humidity level inside the room is maintained within the bounds as prescribed by ASHRAE standards [103].

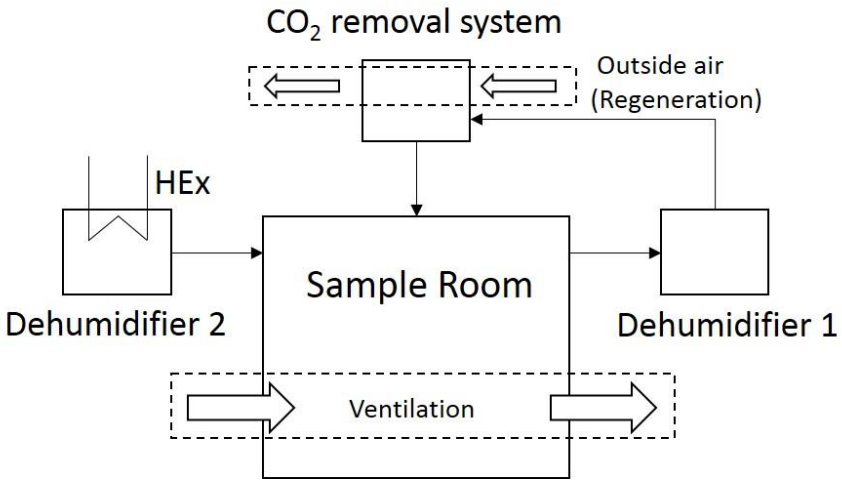

Figure 4.1: Schematic of the enclosed air capture system

The enclosed air capture system is run on a 24 hour cycle. The packed bed (dehumidifier 1) and monolithic systems are switched on at 9 AM when the office hour starts and the systems continue to run until the CO_2 level is brought back to its initial conditions. The flow from dehumidifier 2 is tuned such that humidity inside the room is always within desired level. This regenerates the dehumidifier 2 which is switched with dehumidifier 1 for the next day operation. The regeneration of the zeolite 13X monoliths is performed with outside air through concentration swing adsorption.

4.2.2 Model Equations

There are certain assumption that are used to model the multi-component, multi bed system. These assumptions are listed as follows:

- The regular human occupancy inside the room is assumed to be 8 hours (9 AM – 5 PM) per day.
- The gases inside the room are well mixed.
- Ideal gas law is assumed for non-condensable components.

Based on the above assumptions, a mathematical model is developed to capture the dynamics of the multi-component, multi bed system. Coupled heat and mass transfer model is developed for the sample room, CO_2 removal monolithic system and packed bed dehumidification system. The details regarding modeling complex heat and mass transfer equations for monoliths and packed bed systems can be found in APPENDIX A and APPENDIX B.

The gas concentration dynamics inside the room is modeled using Eq. 5.

$$V_1 \frac{dC_{i,R}}{dt} = R_i + F_V C_{i,in} - F_V C_{i,R} + F_M C_{i,\mathrm{M}} - F_M C_{i,D} \qquad (5)$$

where V_1 is the room volume (m^3), R is the perspiration/respiration rate of healthy adult (mol/s), C is the concentration of i^{th} gas component (mol/m^3) and F is the gas flow rate (m^3/s). The subscript R, M and D represents the room, monolith entrance and dehumidifier entrance respectively. The CO_2 and H_2O adsorption rate is approximated by a linear driving force model provided in Eq. 6.

$$\frac{\partial Q_i}{\partial t} = K_i(Q_i^{eq} - Q_i) \quad (6)$$

where Q_i is adsorbed gas concentration for i^{th} component (CO_2 for monolith and H_2O for dehumidifier), K is the overall mass transfer coefficient and Q_i^{eq} is the equilibrium concentration of the i^{th} component as determined by the isotherm equations. The heat of adsorption for CO_2 is determined using the Clausius−Clapeyron equation at 25, 50, and 75 °C. It is calculated to be 57 kJ/mol for 3D zeolite 13X monolith. Table 4.1 lists the values of parameters used in the multi bed model.

Table 4.1: System properties of the enclosed air capture system

Parameter	Value	Unit
Air thermal conductivity, k_g	0.0257 [72]	W/m-K
Air heat capacity, $C_{p,g}$	1003 [72]	J/kg-K
Air density, ρ_g	1.1839 [72]	kg/m^3
Zeolite 13 X thermal conductivity, k_{ads}	0.1 [115]	W/m-K
Zeolite 13X heat capacity, $C_{p,ads}$	836 [115]	J/kg-K
Zeolite 13X bulk density, ρ_{ads}	689 [116]	kg/m^3
Silica gel thermal conductivity, k_{sil}	0.17 [117]	W/m-K
Silica gel heat capacity, $C_{p,sil}$	921 [117]	J/kg-K

Table 4.1 continued

Silica gel bulk density, ρ_{sil}	770 [117]	kg/m^3
Silica gel porosity	0.5 [118]	-
Silica gel particle diameter	$1.7e^{-4}$ [119]	m
Silica gel mass transfer coefficient, K_{sil}	0.0057 [119]	s^{-1}
H_2O heat of adsorption	35 [114]	kJ/mole
Human oxygen consumption rate, $k_{r,O2}$	3.72×10^{-4} [120]	mole/s-person
Human CO_2 generation rate, $k_{r,CO2}$	2.63×10^{-4} [121]	mole/s-person
Human perspiration rate, $k_{r,H2O}$	5.3×10^{-4} [122]	mole/s-person

The multi component, multi bed model is implemented in gPROMS version 4.0. The model is solved by discretizing the axial and radial domain using the second order centered finite difference method (CFDM). The method of lines is used to solve the partial differential algebraic equations, and the DASOLV integrator is used to solve the resulting equations.

4.3 Parameter Estimation

4.3.1 CO_2 Isotherm

The data points obtained experimentally were fitted using MATLAB through lsqnonlin solver for nonlinear curve fitting. The isotherm parameters were fitted to eq. 7.

$$Q^{eq}_{CO_2} = \frac{q_{sat}\, b_1\, p_{CO_2}}{1+ (b_1\, p_{CO_2})} + b_2 p_{CO_2} \qquad (7)$$

where p_{CO_2} is the partial pressure of CO_2 obtained from C_{CO2_M}, q_{sat} is the saturation capacity of the adsorbent and b_1 and b_2 are isotherm parameters listed in Table 4.2.

Table 4.2: Isotherm parameters for the zeolite 13X adsorbent.

Parameter	**298 K**	**323 K**	**348 K**
q_{sat_1} (mmol/g)	2.6	2.4	1.9
b_1 ($mbar^{-1}$)	1.8	0.3	0.02
b_2 (mmol/g-mbar)	0.0015	0.00096	0.00046

Figure 4.2 shows the model fitting of the isotherm with the experimental date at 25, 50 and 70 C. The figure shows good agreement between the experimental data and the fitted model.

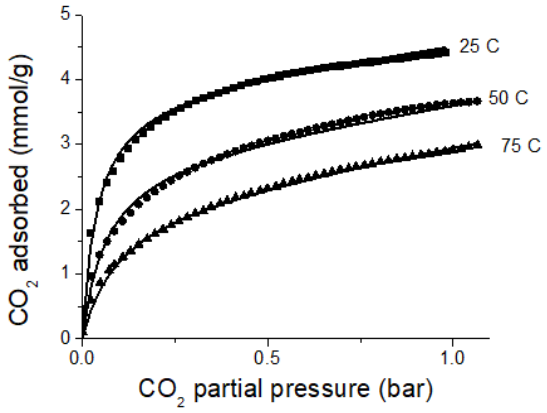

Figure 4.2: 3D zeolite 13X monolith isotherm fitting for CO_2 adsorption

4.3.2 Mass transfer coefficient estimation:

The mass transfer coefficient for 3D zeolite 13X monolith is estimated by fitting the experimental data of fixed bed experiments. Figure 4.3 shows the model fitting with the experimental data. The model parameters such as air velocity, monolith bed length, etc. are kept the same as the experimental set up. It can be seen from the figure that fitting obtained with mass transfer coefficient of 0.016 s^{-1} shows good agreement with the experimental data points. Hence, mass transfer of 0.016 s^{-1} is chosen for further analysis for the enclosed air capture system.

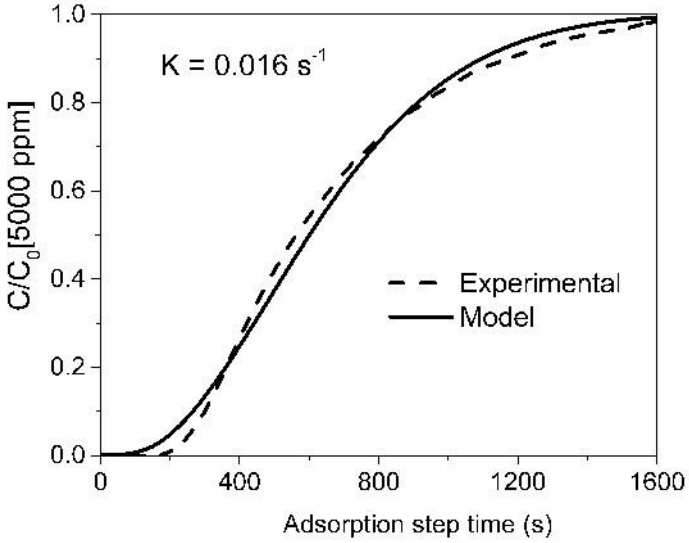

Figure 4.3: Fitting of modeling data with experimental points

4.4 Modeling results

The enclosed air capture system is modeled to maintain a specific air quality inside the room. The minimum accepted oxygen level is 19.5%, in order to avoid adverse health effects of people inside the room. The CO_2 level is maintained below 5000 ppm in order to reduce the chances of headaches and nausea and potentially to increase work efficiency. The humidity level is kept between 30 – 60 %. This range is set because a humidity level below 30% causes discomfort in respiration, while over 60% encourages growth of molds and fungi. The bounds provided are consistent with ASHRAE standards [103].

In order to capture the concentration profiles of the multi component system, I have used the system design parameters provided in Table 4.3. A room size of 5×5 m^2 with the ceiling height of 2.5 m is chosen as a sample room which has enclosed air capture system installed to maintain the air quality. It is assumed that 5 people occupy the room during regular

office hours (9 AM – 5 PM). The dimension of 3D monolith is determined based on the room dimensions, number of people and zeolite 13X adsorption properties, such that CO_2 concentration inside the room is to remain below 5000 ppm at all times. The size of dehumidifier packed bed is determined such that it maintain the humidity level inside the room between 30-60% during an entire day of operation of enclosed air capture system.

Table 4.3: Design parameters of the enclosed air capture system

Parameter	**Value**	**Unit**
Room size	5×5×2.5	m^3
Number of people	5	-
Monolith cell density	400	cpsi
Monolith outer radius	0.22	m
Monolith length, *L*	0.6	m
Monolith channel wall thickness	325	μm
Packed bed dimension	0.60×0.30	m^2

I have defined three different ventilation rates:

1. Normal ventilation rate: This is the external air flow that needs to be maintained during the office hours in order to keep the air quality within the bounds without the use of enclosed air capture system.
2. Reduced ventilation rate: With the use of enclosed air capture system, the amount of external flow rate required to keep the air quality within the bounds is less than

normal ventilation rate. Hence, the flow rate during such scenario is termed as reduced ventilation rate.

3. No-Occupancy ventilation rate: During non-office hours, the office space is not occupied with people. Hence, only a minimum ventilation rate needs to be maintained which is termed as no-occupancy ventilation rate.

Table 4.4 lists the values of different kinds of ventilation rates and other operating parameters that have been used in modeling the enclosed air capture system.

Table 4.4: Operating parameters of the enclosed air capture system

Parameter	**Value**	**Unit**
Normal ventilation rate	14×10^{-4}	m^3/s-person
Reduced ventilation rate	4.5×10^{-4}	m^3/s-person
No-Occupancy ventilation rate	2.0×10^{-4}	m^3/s-person
Net cycle time	24	hr
Monolith air flow rate	3	m/s
CO_2 adsorption time	300	s
CO_2 desorption time	300	s

The cost of electricity in the US is usually higher during 2 – 7 pm [123]. For enclosed air capture system to be cost effective, I have analyzed three cases as mentioned below (also illustrated in Figure 4.4):

A) During office hours (9 AM – 5 PM), the air quality is maintained within the defined limits by running the enclosed air capture system (monoliths for CO_2 removal and packed bed for dehumidification) and maintaining reduced external ventilation. The enclosed air capture system is switched off from 5 – 7 PM. The enclosed air capture system is switched on after 7 PM until the CO_2 level has reached the initial concentration.

B) During office hours, the monoliths and packed bed operate from 9 AM – 2 PM. From 2 – 7 PM, the enclosed air capture system is switched off and the air quality inside the room is maintained by normal ventilation. The enclosed air capture system is switched on after 7 PM until the CO_2 level has reached the initial concentration.

C) During the office hours, the monolith and packed bed are operative from 9 AM- 5 PM, except for an interim period such that the air quality is maintained within the limits without the need for increase in external ventilation. The modeling results indicate a 20 minute window between 2 -5 pm, during which the enclosed air capture system can be switched off with this strategy. Enclosed air capture system is switched off from 5 – 7 PM. The enclosed air capture system is switched on after 7 PM until the CO_2 level has reached the initial concentration.

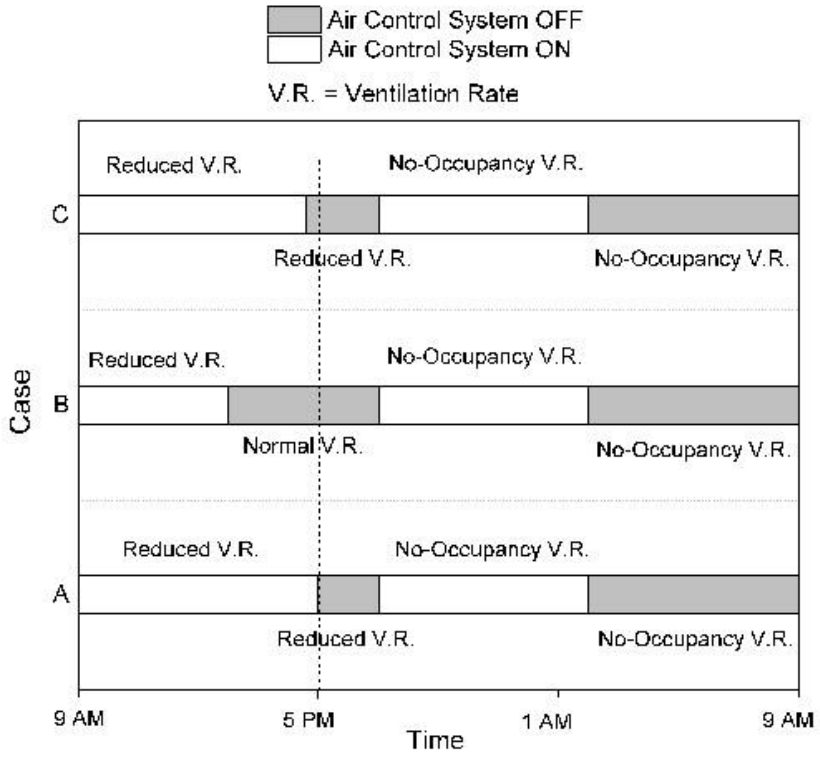

Figure 4.4: Different cases for implementation of enclosed air capture system

Figure 4.5 provides the operating cost ($/yr) of the above cases. It can be seen from the figure that case B has the highest operating cost. This is due to the increase in external flow rate (because of normal ventilation rate) from 2 – 7 PM which results in higher consumption of electricity to condition the excess ventilated air. It is also evident from Figure 4.5 that case A and case C have the same economics. This signifies that even though the monolith and packed bed are switched off for 20 minutes (between 2 – 7 pm) in case C, it does not lower the operating cost as compared to case B. This is because the power consumption due to blowers is relatively small as compared to air conditioners (refer section 4.6). Hence switching off the enclosed air capture system for 20 minutes does not

have substantial effect on the overall cost. I have considered case A for the purpose of further analysis in this chapter.

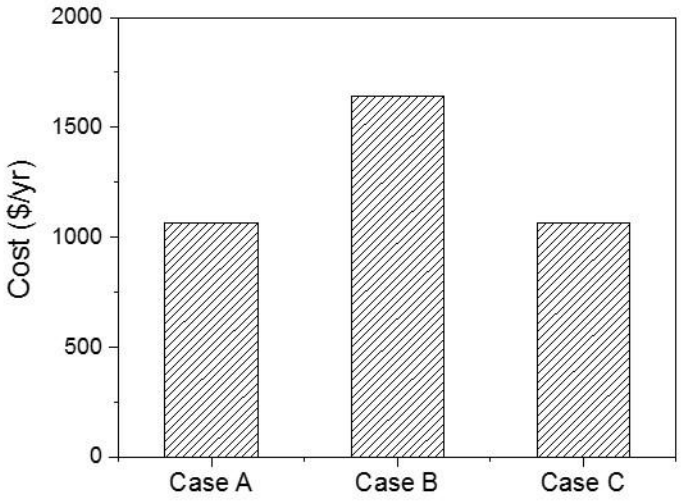

Figure 4.5: Operating cost of enclosed air capture and conventional ventilation system

Using the strategy described in case A, the system was modeled to analyze the dynamics of CO_2, O_2 and H_2O concentration. Figure 4.6 shows the CO_2 concentration inside room (Figure 4.6 a) and at monolith exit (Figure 4.6 b) on a 24 hour time basis. The CO_2 concentration inside the room increases during 9 AM – 5 PM due to respiration by the people present inside the room. This can be seen from Figure 4.6 a, where the CO_2 concentration inside the room rises during this period. However, as seen from the figure, there are periodic drops in the CO_2 concentration. This is because the CO_2 is being removed at regular intervals by the zeolite 13X monoliths as seen from Figure 4.6 b. After 5 PM, the people are assumed to leave the room. In order to decrease the CO_2 concentration back to the initial value, the CO_2 removal system (monolith) needs to be run again. However the

enclosed air capture system is not operative till 7 PM. This is done to save electricity cost which is usually higher during that time [123]. This is evident from Figure 4.6 a in which slow reduction in CO_2 concentration can be seen from 5 – 7 PM. The slow reduction is due to no-occupancy ventilation rate that has been maintained once the people have left the room (Table 4.4). The CO_2 removal system starts to operate from 7 PM onwards until the CO_2 concentration inside the room stabilizes at the lower bound. This can be seen from Figure 4.6 a, where CO_2 concentration drops until it reaches the initial level at around 3 AM. The periodic adsorption and desorption of CO_2 concentration at the monolith exit can be seen in Figure 4.6 b during this time. After 3 AM, the CO_2 removal system is switched off, since there is no need for further reduction in the room CO_2 concentration. This can be seen from Figure 4.6 a and b, where CO_2 concentration in 3 – 9 AM changes only slightly. This minimal change is due to no-occupancy ventilation rate that has been maintained during night (Table 4.4). This design provides flexibility during this period (3 AM – 9 AM) should there be need for uncertainty quantification due to variations in input parameters such as variation in number of people inside room, variable respiration or perspiration rates, etc.

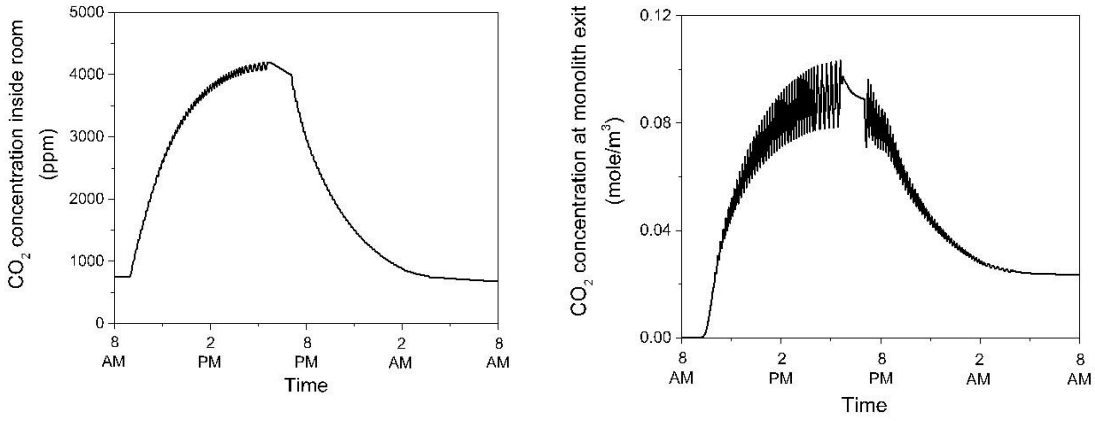

Figure 4.6: CO_2 concentration dynamics a) inside room and b) at monolith exit

In order to analyze the effect of the proposed enclosed air capture system on the CO_2 concentration inside the room, I have considered four different cases: a) no ventilation and no enclosed air capture system, b) with a ventilation system that ensures that the CO_2 level stays below 5000 ppm without an enclosed air capture system, c) reduced ventilation such that CO_2 level remains below 5000 ppm with an enclosed air capture system and d) reduced ventilation without enclosed air capture system. The dynamics of the CO_2 profile from 9 AM to 5 PM in these four cases is illustrated in Figure 4.7. It can be seen from the figure that CO_2 concentration can be only maintained with 5000 ppm with case b and c.

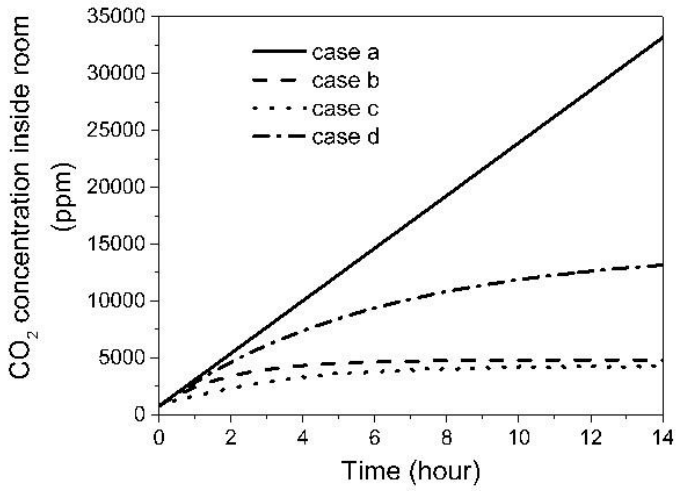

Figure 4.7: CO_2 concentrations inside the room

Figure 4.8 shows the concentration of CO_2, O_2 and H_2O when the enclosed air capture system operates for a week. It can be seen from the figure that the CO_2 concentration remains below 5000 ppm, and humidity level swings between 40 -50% during the entire duration of the operation of the enclosed air capture system. It can also be seen from the figure that the oxygen level initially drops and then reaches equilibrium within 3 days, after

which it swings from 19.5 – 20.4 %. This shows that the multi-bed, multi-component model is able to constraint the air components within the desired ranges.

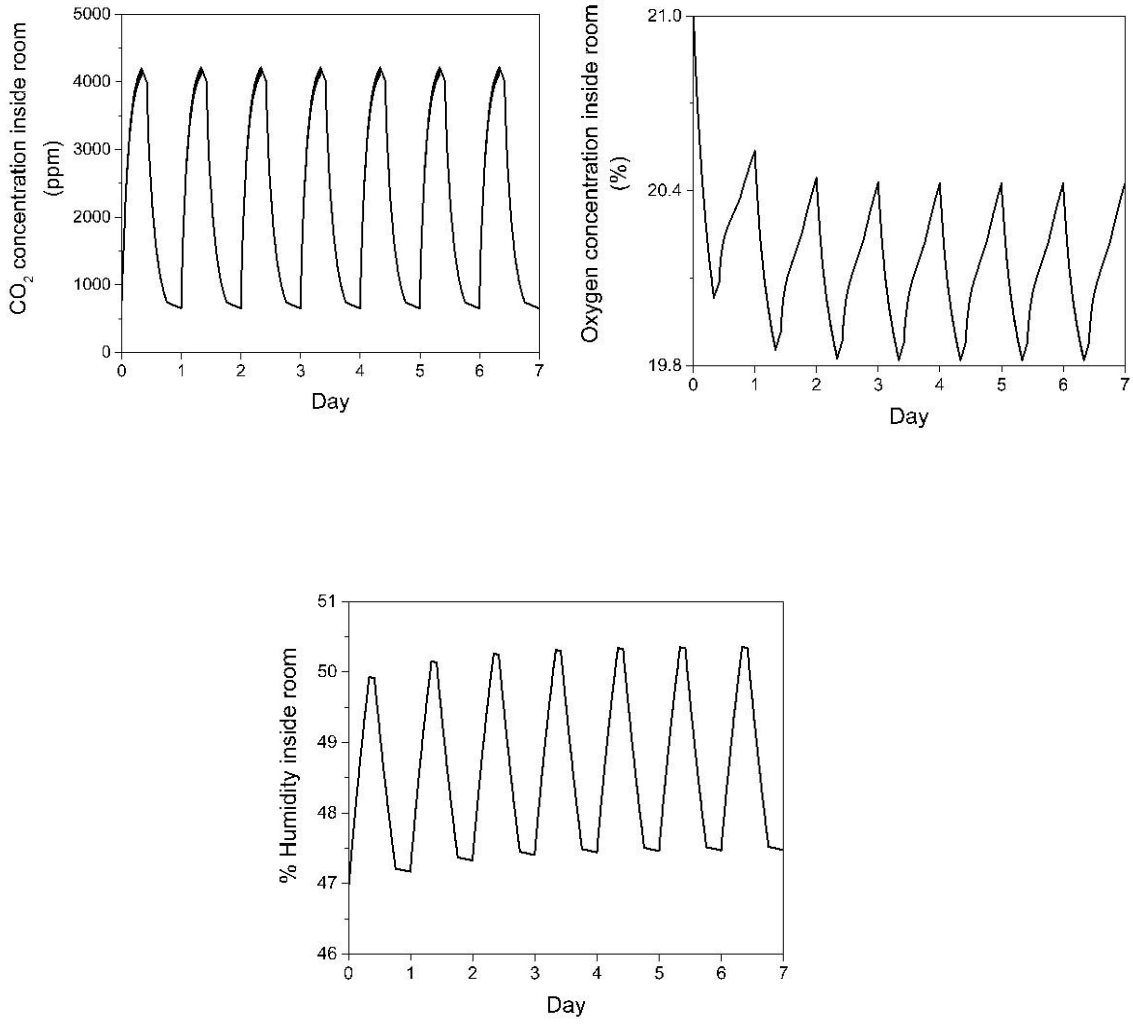

Figure 4.8: Concentration profiles with enclosed air capture system operative for 1 week

4.5 Energy Estimates

The energy requirement of the enclosed air capture system is due to electrical energy required by the air conditioners to condition the externally ventilated air, and the blowers to flow the air through monolithic and dehumidification units. The energy requirement (in Joules) due to blowers is provided in Eq. 8.

$$E_{Blower} = \Delta P q_{air} t_{Blower} \eta \tag{8}$$

where q_{air} is the volumetric flow of air through the enclosed air capture units in m^3/s, η is the blower efficiency (assumed as 80%) and t_{Blower} is the time of operation of the blower. ΔP is the pressure drop (pascals) across the enclosed air capture system given by Ergun equation (Eq. 9).

$$\frac{\Delta P}{L} = \frac{150\mu(1-\varepsilon)^2 v}{\varepsilon^2 d_p^2} + \frac{1.75(1-\varepsilon)\rho v^2}{\varepsilon^3 d_p} \tag{9}$$

where μ is the viscosity of air, ε is void space of the bed, v is the air velocity, d_p is the particle diameter and ρ is the density of air.

The energy requirement of an air conditioner consists of sensible heat and latent heat. Sensible heat is required to bring the temperature of external air in equilibrium with the room temperature. The energy requirement (in Joules) due to sensible heat (E_s) is given by Eq. 10.

$$E_s = C_{p,air}\rho_{air}q''_{air}\Delta T \quad (10)$$

where $C_{p,air}$ is the specific heat of air, ρ_{air} is the density of air, q''_{air} is the volumetric flow of air through the air conditioners and ΔT is the temperature difference between external air and enclosed space. Latent heat is required to maintain the moisture content inside the room. The energy requirement (in Joules) due to latent heat (E_L) is given by Eq. 11.

$$E_L = \rho_{air}q''_{air}L_w dw_{kg} \quad (11)$$

where L_w is the latent heat of vaporization of water and dw_{kg} is the humidity ratio difference (kg water/kg of dry air) which can be estimated using the psychrometric chart or the Mollier diagram. During summer where the cooling load of air conditioners is taken into account, water condensation occurs, and thus cooling load consists of the sum of the sensible heat and latent heat. On the other hand, during winter where the heating load is taken into account, water condensation is negligible, and thus the heating load consists only of the sensible heat.

In order to compute the energy (and cost) of enclosed air capture system in a typical commercial building, I have assumed a 10 m tall building (with 5 floors) occupying a ground area of 250 m^2 (10 rooms on each floor) with a space allocation of 5 m^2 per person.

The energy requirements are computed for the following two scenarios:

1) Conventional ventilation system: The air quality inside the room is maintained by external ventilation only (with normal ventilation rate). The external air flow rate is maintained such that the CO_2, O_2 and humidity level remain within the bounds. The energy consumption is due to conditioning the external air to room condition.
2) Proposed enclosed air capture system: The air quality inside the room is maintained by CO_2 and moisture removal system and reduced ventilation rate as described in the previous section. The energy consumption for enclosed air capture system is due to conditioning of external air and energy required by the blowers to cycle the air inside the room through dehumidification and monolithic units.

Table 4.5 shows the energy usage comparison of the enclosed air capture system with the conventional ventilation system. It can be seen from the table that the energy usage due to blowers is negligible compared to the energy usage by air conditioning units. It can also be seen from the table that that the energy usage by application of enclosed air capture system reduces the energy requirement by 60% as compared to the conventional ventilation system. This is because enclosed air capture system allows reduced ventilation compared to conventional ventilation system. This results in lower energy consumption to condition the external air.

Table 4.5: Energy usage of the enclosed air capture and conventional ventilation systems

System	Components	Energy usage (kW-hr/year)
Enclosed air capture system	Blowers	1130
	Air conditioners	14600
Conventional ventilation system	Air conditioners	36500

The energy usage of conventional ventilation system with the enclosed air capture system is compared in summer as well as winter conditions on an hourly basis as shown in Figure 4.9. It can be seen from the figure that system when people are inside the room, the enclosed air capture system requires only a quarter of the power consumption of the conventional ventilation. This is due to lower external ventilation rate in enclosed air capture system as compared to the conventional ventilation system.

Seasonal differences and daily dynamics is observed in Figure 4.9. For both systems, the summer energy usage is higher than winter because of the additional humidification load incurred for conditioning external air during summer. It can be seen in the figure that the summer hourly energy usage is around twice as compared to winter energy usage. It can also be seen from the figure that the energy usage for both systems is higher during office

hours (9 AM – 5 PM) compared to non-office hours (after 5 PM). This is because the external ventilation is substantially higher during office hours compared to non-office hours (refer Table 4.4). Hence higher energy is required to condition the external air during office hours.

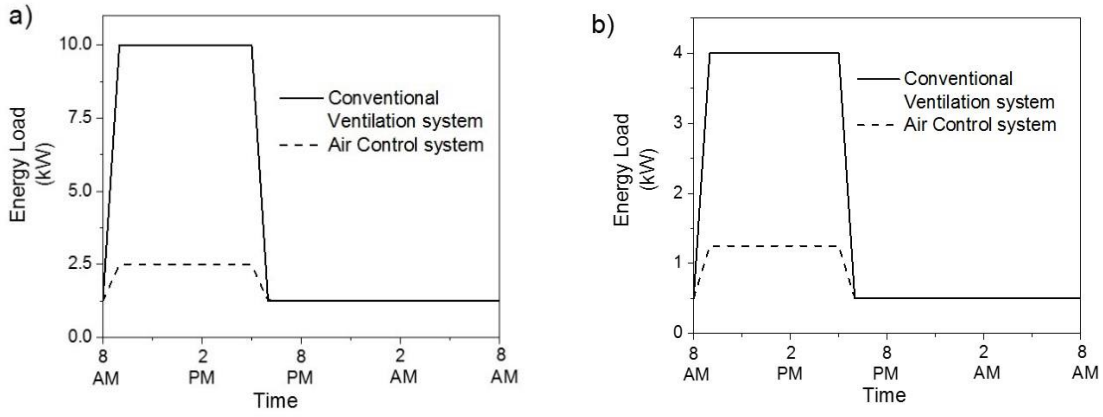

Figure 4.9: Energy consumption during a) summer and b) winter conditions

The energy consumption of capturing unit mass of CO_2 is provided in Table 4.6. A scale up factor of 3.14 [82] have been used to convert the electrical energy to primary energy. It can be seen from the table that the total energy consumption is 1.25 MJ per mole of CO_2 removed. This is more than the energy associated with heat of combustion that generated the CO_2 (0.45 MJ/mole using combusting CH_2 as the basis for comparison). However, it should be noted that the primary objective of the enclosed air capture process is not to capture CO_2, but to reduce the energy burden of air conditioning system by reduced external ventilation. CO_2 capture by the enclosed air capture system is an auxiliary benefit if the CO_2 removed can be utilized, stored or integrated with other processes inside a commercial building, labs and research facilities. It is important to note that the current

configuration removes CO_2 with concentration swing using outside air which results in a low concentration of CO_2 being generated (~10 tCO_2 per building per year). It would be possible to remove the CO_2 with a vacuum and temperature swing to generate nearly pure CO_2 but this would have a higher energy consumption.

Table 4.6: Energy consumption due to CO_2 removal

Primary Energy Requirements	**Value (MJ/mole)**
Air conditioner	1.17
Blower	0.08
Total	1.25

4.6 Cost Estimates

The total cost of enclosed air capture system can be divided into operating and capital cost. The operating cost consist of electrical cost of operating the blowers (C_B) and the air conditioner (C_{AC}). This can be calculated using the Eq. 12 and 13 respectively.

$$C_B = E_{Blower} C_E \tag{12}$$

$$C_{AC} = (E_s + E_L) C_E \tag{13}$$

where E_{blower}, E_s and E_L are energy requirements of blowers, sensible and latent heat respectively, expressed in kW-hr and C_E is the cost of electricity in dollars per kW-hr.

The capital cost consists of blowers, 3D monoliths and a dehumidification unit. The capital cost can be computed using Eq. 14.

$$C_i = \frac{C_{P,i}}{N_{cycle} N_{LT,i}} \tag{14}$$

where C_i is the capital cost of i^{th} component (monolith, blower and silica gel packed bed),$C_{P,i}$ is the purchase cost of the i^{th} component, N_{cycle} is the number of cycles in each year and $N_{LT,i}$ is the life time of the i^{th} component. The lifetime of the adsorbent-monoliths is assumed to be 1 year and for blowers and the silica gel packed bed, the lifetime is assumed to be 5 years.

Using Eq. 12, 13 and 14, I have calculated the cost associated with enclosed air capture system. Figure 4.10 shows the distribution of cost of enclosed air capture system in $/year. It can be seen from the figure that the operating cost (OPEX) for the air conditioner (A/C) is the key cost component of enclosed air capture system. This is because of high electricity consumption to condition the ventilated air.

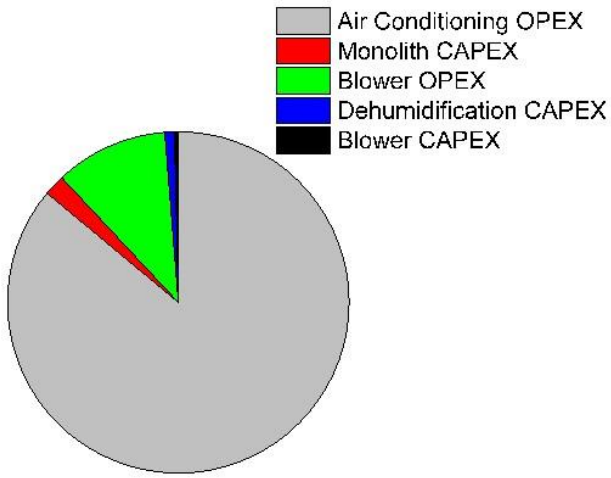

Figure 4.10: Cost distribution of enclosed air capture system

The cost to condition the external air through enclosed air capture system is around $1070 per year while the conventional ventilation system costs around $2430 per year. The enclosed air capture has a lower cost because of lesser volume of external air being conditioned in the enclosed air capture system.

Another metric to quantify and assess the economics of the enclosed air capture system is to evaluate the cost in terms of the unit mass of CO_2 removed from the air. Table 4.7 shows the contribution of the components involved in removing CO_2. The total cost of CO_2 removal from the enclosed environment is $180 per tCO_2 removed. It can be seen from the table that the operating cost (OPEX) of the air conditioner is the leading cost contributors. The total cost of CO_2 removal can be further reduced by optimizing the cycle time and synthesizing a new adsorbent that has a higher CO_2 adsorption capacity, which should be manufactured in a 3D monolith structure

Table 4.7: Economics for CO_2 removal

Cost components	**Value ($/tCO$_2$)**
Air conditioner OPEX	154
Blower OPEX	20
Monolith CAPEX	3
Packed bed CAPEX	2
Blower CAPEX	1
Total cost	180

4.7 Carbon Footprint

It is important to assess the impact of enclosed air capture system on the environment because of the energy consumption and CO_2 emissions, and compare its performance with the conventional ventilation system. In order to get realistic estimates, I assume an office inventory of 45 million m^2 which is roughly the same size as net office space in New York City [118]. I also assume an average of 5 floor office buildings which results in 1 MtCO_2 removal by the enclosed air capture system per year. Keeping the statistics same for the

conventional ventilation system, I have compared the CO_2 emissions in terms of CO_2 equivalent for both systems.

Table 4.8 lists the emission data for the two systems based on the source of electricity generation. The amount of CO_2 emission is calculated where five different sources of electricity generation per unit energy consumption are given: solar, wind, natural gas (NG), coal and US grid. Among these sources, emissions from solar and wind per unit energy consumption is substantially lower because of their renewable nature.

Table 4.8: CO_2 emissions from enclosed air capture and conventional ventilation system (The analysis is based on 1 $MtCO_2$ removed)

Electricity generation source	**Life Cycle Greenhouse Gas Emissions [124] (g CO2e/kWh)**	**Enclosed air capture system ($MtCO_2e/yr$)**	**Conventional Ventilation system ($MtCO_2e/yr$)**
Solar	55	0.14	0.36
Wind	15	0.04	0.10
NG	490	1.29	3.22
Coal	820	2.15	5.39
US grid	700	1.84	4.60

As mentioned earlier in this section, the analysis in Table 4.8 is based on 45 million sq. m of office inventory which is a typical estimate for New York. If the emissions from enclosed air capture and conventional ventilation system for electricity generated from US grid source is analyzed, difference in emissions from both the systems is equivalent 92.3 million incandescent lamps switched to LEDs or 6.4 million barrels of oil consumed [125].

The above analysis was based on scale up studies with office space of the order of magnitude of New York city. If the emissions from a single building with five floors and occupying 250 sq. m of ground space is analyzed, the emissions for enclosed air capture and conventional ventilation system are 10.2 and 25.5 tCO_2e/yr respectively. The difference in their emissions provide the same environmental benefit as replacing 510 incandescent bulbs to LEDs.

4.8 Conclusion

Reduced ventilation rates leads to lower consumption of electrical energy by air conditioners whilst keeping the gas concentrations similar through adsorption. This chapter utilizes this principle and proposes a strategy to lower the energy consumption of buildings. An alternative route for maintaining air quality inside the enclosed space is discussed through an enclosed air capture system. CO_2 removal through 3D zeolite 13X monolith and H_2O removal by silica gel packed bed is simulated using a multi-component, multi-bed model. The CO_2 concentration dynamics is validated against experimental runs to establish the adsorption equilibrium capacity and mass transfer rate of CO_2 through the adsorbent. The multi-bed model is simulated on a 24 hour basis and system parameters are tuned to keep the CO_2, O_2 and humidity level within the safe limits. Energy and economic

analysis of the enclosed air capture system is performed and compared against the conventional ventilation system. It is found that the energy and cost requirement of the enclosed air capture system is dominated by the electricity consumption by the air conditioners. On comparison of the enclosed air capture system with the conventional ventilation system, it is found that installation of the enclosed air capture system leads to 60% reduction in energy usage as compared to the conventional ventilation system without compromising the concentrations of water, carbon dioxide and oxygen. It is also concluded that the power consumption by the enclosed air capture system is around one-fourth of the conventional ventilation system during the office hours. Similarly, the cost requirements of the enclosed air capture system are lower than conventional ventilation system despite the increased capital cost of the enclosed capture system. It is concluded that using a better adsorbent with a higher CO_2 equilibrium capacity would further bring down the cost and energy requirement of the enclosed air capture system. Another strategy to cut down cost is to use a water stable adsorbent, which would entirely remove the dehumidification unit.

Energy and cost requirements of the enclosed air capture system are also quantified in terms of the mass of CO_2 removed. The strategy proposed in this paper discards the CO_2 removed back into the atmosphere. This paper also presented a scale up study by analyzing the carbon footprint of total office inventory of New York and compared the emissions from the enclosed air capture system with the conventional ventilation system. It is found that total annual savings in emissions by using enclosed air capture system is equivalent to 92.3 million incandescent lamps switched to LEDs or 6.4 million barrels of oil consumed.

CHAPTER 5. UNCERTAINTY QUANTIFICATION

5.1 Introduction and Literature Review

CO_2 capture systems have been modeled by understanding the physical process and solving coupled heat and mass balances equations through numerical simulators [126-127]. Model parameters such as mass transfer coefficient, adsorbent thickness etc. often remain uncertain due to lack of precise measurement as well as incomplete information. The accuracy of model outputs such as equipment design and operating conditions as well as performance metrics such as the amount and purity of CO_2 captured can be questioned because of these parametric uncertainties. For this problem, quantification of these uncertainties is necessary for more useful model predictions.

There has been substantial research in modeling uncertainty in different physical systems.[128-132] Monte Carlo simulation [133-135] is one ubiquitous approach for handling uncertainty. Davis and Keller [136] utilized Monte Carlo simulations (MCS) to analyze uncertainties introduced due to limitation in measurement techniques in data analysis for Geographical Information Science. Cox et al.[137] described a procedure to evaluate measurement uncertainty based on propagation of probability distributions on parameters using Monte Carlo simulations. However, Monte Carlo methods are often computationally expensive since it involves repetitive deterministic model simulations for different realizations of input samples. Another class of methods, which involve non-sampling techniques, are perturbation methods;[138-139] which utilize the concept of Taylor series expansion of stochastic terms in the model equations. However, this is limited to small perturbations in uncertain inputs and outputs. Hence, it is hard to estimate accurate model

predictions through perturbation methods for a complex, nonlinear system where small variation in input parameter may result in large variations in model outputs.[140] Stochastic Galerkin methods [141-142] are another approach, which can handle large variations in model inputs and outputs. The stochastic Galerkin methods are a generalization of the Polynomial Chaos Expansion (PCE), which was first introduced by Wiener [143].

There are two main approaches to solving a system of equations through PCE: intrusive and non-intrusive methods.[144-145] The intrusive polynomial chaos (IPC) method involves modification of original governing equations by introducing additional dimension for each input uncertainty. The PCE framework is solved using Galerkin projections of the orthogonal basis functions.[146-149] IPC methods can be challenging in terms of model complexity. However, once the PCE framework is formulated, this method is efficient in terms of computational time since it requires only a single simulation of the model to compute the uncertainty in the model outputs.

The non-intrusive polynomial chaos (NIPC) method, on the other hand, keeps the original governing equations intact. It involve small numbers of model simulations by sampling realizations of input uncertain parameters through a sampling scheme.[150-152] It has been shown[153] that Latin Hypercube and Hammersley sampling shows better accuracy and smoother convergence, as compared to random sampling. The NIPC method treats the model as a black box and evaluate the output PCE coefficients through different approaches such as linear regression and spectral projection.[154-155] In the case of correlated uncertain parameters, certain transformations (Nataf [156], Box Cox [157], Rosenblatt [158]) are required to convert them into uncorrelated uncertain parameters before IPC or NIPC method can be employed.

PCE methods have been used to efficiently analyze and predict model outputs for complex systems.[159-164] In their pioneering work, Ghanem and Spanos [165] demonstrated the use of PCEs, to represent uncertain parameters in quantifying uncertainty in computational models. Their method was based on the original theory of Wiener[143] and demonstrated higher order representations of PCE with increased computational efficiency. Xiu et al.,[147, 166-168] employed orthogonal polynomial functional from the Askey scheme to compare generalized PCE (or gPCE) method with MCS. They applied the algorithm to model uncertainty and its propagation in incompressible flows and steady state diffusion problems. They showed that gPCE method showed considerable speed up in performance compared to MCS.

There have been a few studies on application of PCE in chemical systems.[169-171] Ghanem et al.[172] studied PCE approximations in the context of H_2-O_2 ignition under supercritical-water conditions and extended their work to one dimensional reacting flow simulations. They also developed a multi-resolution analysis scheme for the quantification of parametric uncertainties in chemical systems. [173] The PCE method has been explored for carbon storage methods in the area of carbon capture utilization and sequestration (CCUS) technologies. Sahinidis et al.[174] introduced mixed integer programming formulation for systematic selection of subsets of basis function to find optimal CO_2 injection rates that maximize CO_2 immobilization under parametric uncertainty.

However, there has been no study that explores the application of PCE to carbon capture technologies. In this chapter, I quantify uncertainties on carbon capture systems through PCE based methods. The chapter is organized as follows: Initially, I discuss the PCE methods that is used to quantify the uncertainties in the CO_2 capture model. Then, I perform

uncertainty quantification on DAC by discussing uncertainties up to three uncertain parameters. Next, I discuss the results of uncertainty quantification on the CO_2 capture from the enclosed environments. I use the Galerkin method for IPC, Latin Hypercube Sampling (LHS) for sampling techniques, linear regression to evaluate output PCE coefficients for NIPC and Nataf transformations for handling correlated uncertain parameters.

5.2 Computational Methods

In this section, I discuss the methods and techniques used to formulate a PCE model, both for intrusive and non-intrusive methods.

5.2.1 The generalized PCE

Let λ be a uncertain parameter in a physical model with a given probability density function. Then, it can be represented by a generalized PCE form: [166]

$$\lambda = \lambda_0\phi_0 + \sum_{i=1}^{\infty}\lambda_i\phi_1(\xi_i) + \sum_{i=1}^{\infty}\sum_{j=1}^{i}\lambda_{ij}\phi_2(\xi_i,\xi_j) + \sum_{i=1}^{\infty}\sum_{j=1}^{i}\sum_{k=1}^{j}\lambda_{ijk}\phi_3(\xi_i,\xi_j,\xi_k) + \ldots \tag{15}$$

Eq. 15 can be written in a condensed form as:

$$\lambda = \sum_{i=1}^{\infty}\hat{\lambda}_i\phi_i(\xi_1,\xi_2,\ldots) \tag{16}$$

Here, $\hat{\lambda}_i$ are the deterministic coefficients (or the PC coefficients) of the expansion of the uncertain parameter λ; ϕ_i is the Wiener polynomial chaos (or the basis functions) of order

i; $\xi_{i/j/k}$ are standard normal vectors. It is unrealistic to represent infinite terms in the summation (eq. 15 and 16) for computational purposes. Hence, the PCE approximation is truncated to represent an expansion of order *p* and dimension *n*. The truncated form of the PCE approximation is given by:

$$\lambda = \sum_{i=0}^{P} \hat{\lambda}_i \phi_i(\xi_1, \xi_2, ..., \xi_n) \tag{17}$$

where *P* is the total number of terms in the PCE approximation:

$$P + 1 = \frac{(p+n)!}{p!n!} \tag{18}$$

The basis function, ϕ_i are orthogonal in L_2-space with respect to the inner product, represented by $\langle , \rangle$, such that:

$$\langle \phi_i(\xi), \phi_j(\xi) \rangle = \int \phi_i(\xi) \phi_j(\xi) w(\xi) d\xi = \delta_{ij} \langle \phi_i^2(\xi) \rangle \tag{19}$$

where δ_{ij} is the Kronecker delta and $w(\xi)$ is the probability density function of ξ. There is a one-to-one correspondence between the basis function ϕ_i, the uncertain parameter ξ and the probability density function $w(\xi)$. Assuming that the uncertain input parameter follows a Gaussian distribution, the basis function, ϕ_n is a Hermite polynomial of the Wiener-Askey chaos scheme [166]

$$\phi_n = (-1)^n e^{\frac{\xi^T \xi}{2}} \frac{\partial^n}{\partial \xi_1 \partial \xi_2 ... \partial \xi_n} e^{-\frac{\xi^T \xi}{2}} \tag{20}$$

The corresponding probability density function is:

$$w(\xi) = \frac{1}{\sqrt{2\pi}} e^{-\frac{\xi^T \xi}{2}} \tag{21}$$

Depending on the type of distribution of the uncertain input parameter, the distribution type of ξ and the corresponding basis function is decided. Table A.3 gives a list of uncertain input distributions and their corresponding basis functions.

Table 5.1: Relation between the uncertain input distribution and the basis function

Type	Uncertain input distribution	Basis function	Support
Continuous	Gaussian	Hermite	(-∞,∞)
	Gamma	Laguerre	(0, ∞)
	Beta	Jacobi	[a,b]
	Uniform	Legendre	[a,b]
Discrete			

Poisson	Charlier	{0, 1, 2…}
Binomial	Krawtchouk	(0, 1,….,N}
Negative binomial	Meixner	{0, 1, 2…)

For a one-dimensional uncertain input parameter, eq. 17 reduces to,

$$\lambda = \sum_{i=0}^{P} \hat{\lambda}_i \phi_i(\xi) \tag{22}$$

The first few Hermite polynomials for a one-dimensional uncertain input parameter are given as:

$\phi_0 = 1$
$\phi_1 = \xi$
$\phi_2 = \xi^2 - 1$
$\phi_3 = \xi^3 - 3\xi$
...

Hence, the PCE approximation can be written as:

$$\lambda = \hat{\lambda}_0 + \hat{\lambda}_1 \xi + \hat{\lambda}_2(\xi^2 - 1) + \hat{\lambda}_3(\xi^3 - 3\xi) + ... \tag{23}$$

In order to compute the PCE analysis, evaluation of PCE coefficients, $\hat{\lambda}_i$ is required. This is done by taking Galerkin projection of the orthogonal basis function on the PCE approximation. Thus, PCE coefficients are evaluated as:

$$\hat{\lambda}_i = \frac{\langle \lambda, \phi_i \rangle}{\langle \phi_i^2 \rangle} \tag{24}$$

In case of multi-dimensional uncorrelated uncertain input parameters, the basis functions of the model output variables are obtained by taking the product of individual basis functions for each uncertain parameter and the joint probability density function is obtained by taking the product of probability density functions of the individual uncertain parameters:

For a 2-dimensional uncertain input parameter with Gaussian distribution, PCE approximation for the model output variable, *Y* is given as:

$$Y = \hat{y}_0\phi_0 + \hat{y}_1\phi_1 + \hat{y}_2\phi_2 + \hat{y}_3\phi_3 + \hat{y}_4\phi_4 + \hat{y}_5\phi_5 + \ldots \tag{25}$$

where

$\phi_0 = 1$
$\phi_1 = \xi_1$
$\phi_2 = \xi_2$
$\phi_3 = \xi_1^2 - 1$
$\phi_4 = \xi_2^2 - 1$
$\phi_5 = \xi_1\xi_2$
...

5.2.2 Nataf Transformation

PCE approximations are based on polynomials that are functions of orthogonal standard uncertain parameter (ξ). In case of correlation between the uncertain input parameters, appropriate transformation is required before the PCE approximation is applied to the model. In this chapter, the Nataf transformation is utilized to convert the correlated input parameters into an orthogonal set as discussed below.

The Nataf Transformation [156] is a nonlinear mathematical model to convert a given original space of a correlated vectors to a mutually independent standard normal space. It does not require information about the joint PDF of all the input uncertain parameters. However, the marginal PDFs of individual uncertain parameter must be known. The procedure to implement Nataf transformation on correlated uncertain input parameters is given below:

Step 1: *Convert correlated parameters to correlated standard normal vectors*

Let x_i be the original correlated uncertain parameters and $F(\,)$ is the cumulative distribution function (CDF) of the original probability distribution. The correlated uncertain parameters, x_i, are converted to the corresponding correlated standard normal vectors, z_i, through eq. 26.

$$\varphi(z_i) = F(x_i) \tag{26}$$

where $\varphi(\,)$ is the standard normal CDF.

Step 2: *Convert correlated standard normal vectors to uncorrelated standard normal vectors*

The correlated standard normal vectors, as obtained from Step 1, are then transformed to uncorrelated standard normal vectors through eq. 27.

$$z_i = L\ \xi_i \tag{27}$$

where L is obtained by Cholesky decomposition of the correlation matrix of z, and ξ_i are the uncorrelated standard normal vectors (orthogonal in parametric space).

5.2.3 Intrusive Polynomial Chaos (IPC) Method

The IPC method involves modification of original governing equation by introducing additional probabilistic dimensions through Galerkin projection. Let Y be the output vector of a model, M, and X denoting a vector of multi-dimensional uncertain parameters as given by:

$$M(Y; X) = 0 \tag{28}$$

Using the probabilistic domain ξ in the model, M, and taking inner product with the basis function, eq. 28 becomes:

$$\left\langle M \sum_{k=0}^{N} \left(\sum_{j=0}^{N} \sum_{i=0}^{N} Y_i \phi'_i(\xi_1, \xi_2, ..., \xi_n); X_j \phi_j(\xi_j) \right), \phi_k \right\rangle = 0 \tag{29}$$

where ϕ'_i represents the orthogonal polynomial for the output variables with a joint probability density function and ϕ_j and ϕ_k are the basis functions for the uncertain input parameters. This results in a set of N+1 coupled equations for each original governing

equation. The modified model undergoes single deterministic simulation to generate PCE coefficients for the output vectors, which is used to analyze the uncertainty in output variables through PCE approximations.

In case of complex non-linear mathematical models with multi-dimensional uncertain inputs, implementation of IPC method can be a challenging task since converting the original deterministic model to the PCE framework can be complicated.

5.2.4 Non-Intrusive Polynomial Chaos (NIPC) Method

The NIPC method is used to obtain approximations of the polynomial coefficients without modifying the original model. Given a model ($M(Y; X(\xi)) = 0$) with a d-dimensional basis, $\xi = (\xi_1, \xi_2, ..., \xi_d)$, the NIPC procedure is performed through following steps:

1) Generate N_s samples of $\xi = \{\xi_i^j \mid_{i=1}^{d}\}_{j=1}^{N_s}$ through a sampling technique. In this chapter, I have used Latin Hypercube Sampling (LHS) strategies to generate the sample points.

2) Evaluate the model M, at each sample point, ξ^j and determine the model output, $Y^j = M(X(\xi^j))$.

3) Perform Least Square Approximation to evaluate approximations of the output PCE coefficient, $\hat{y}_k \mid_{k=0}^{P}$ where P is the number of terms in the output PCE expansion (eq. 18).

4) Evaluate the output variable, *Y* through PCE approximations, $Y = \sum_{k=0}^{P} \hat{y}_k \phi_k(\xi)$.

The techniques (Latin Hypercube Sampling and Least Square Approximation) that are used to perform NIPC are explained next.

5.2.5 Latin Hypercube Sampling Method

The computational cost of NIPC is dominated by deterministic evaluation of model at each sample point, ξ^j. The LHS method, an extension of stratified sampling, ensures each of the input parameters has all portions of its range represented by creating equiprobable partitioning of the range. Further, LHS can deal with many input parameters and is computationally cheap to generate.[175] A general procedure to perform LHS design is given as follows:

1) Divide each parameter range by creating N_s equiprobable non-overlapping partition.
2) Select one value at random from each partition based on its probability density.
3) Repeat the first two steps for all the uncertain parameters, $\xi_i\{i = 1, 2, ..., d\}$.
4) Pair the N_s values of each uncertain parameter with others at random.

5.2.6 Least Square Approximation Method

The output PCE coefficients can be estimated by Least Square Approximation (also called, Regression methods). Once the sample input points are selected using LHS method, the deterministic model is evaluated at each sample point:

$$M(Y^j, X(\xi_i^j|_{i=1}^d) = 0$$

The approximations of output PCE coefficients (Y_i) denoted by $\hat{Y}_i$, is estimated by solving eq. 30.

$$\hat{y} = \arg\min_{y_k} \sum_{j=1}^{N_s} \left(Y^j - \sum_{k=0}^{P} y_k \phi_k(\xi^j) \right)^2 \tag{30}$$

5.3 Applications in CO_2 Capture from ambient air

I have applied the PCE method to analyze the uncertainties involved during the adsorption dynamics of the DAC model explained in Chapter 2. The coating of the adsorbent film on the monolith substrate is non-uniform as seen from Figure 2.1. This leads to uncertainty in overall mass transfer coefficient, k inside the adsorbent (refer eq. 40-42 in Appendix A).

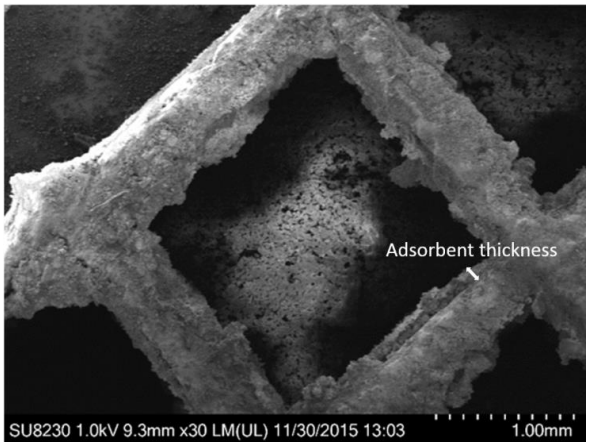

Figure 5.1: SEM image for the film growth of a mmen-Mg_2(dobpdc) MOF on a 100 cpsi monolith substrate [176]

We can also have uncertainty in the inlet gas flowrates due to fluctuations in inlet conditions. Figure 5.2 shows the impact of uncertainty on inlet velocity on CO_2 breakthrough curve. The inlet velocity is assumed to follow a Gaussian distribution, N ~ (3, 0.5). It is evident from the figure that uncertainty in the inlet gas velocity can produce substantial uncertainty on the CO_2 breakthrough curve. This can cause uncertainty in computing the adsorption time, which, in turn, can create uncertainty in computing the energy and cost of DAC. Hence, quantification of these uncertainties is important.

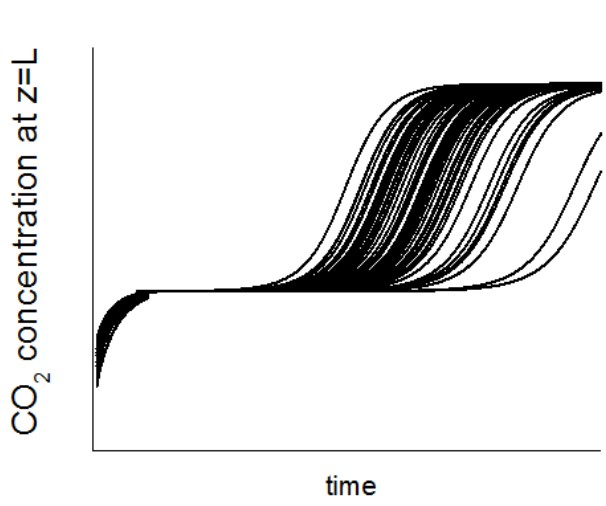

Figure 5.2: Effect of uncertainty in mass transfer rates on a CO_2 breakthrough curve

5.3.1 Uncertainty in one parameter

In this section, I compare IPC and NIPC methods with the MCS results when the uncertainty is present in one input parameter. I have assumed uncertainty in inlet temperature, T_0 (N(298,1.0)) which may result due to fluctuations in the boundary conditions.

The first step of applying the IPC method is PCE coefficient determination by taking Galerkin projections of orthogonal basis functions as described earlier (eq. 24). Figure 5.3 shows the histogram of the inlet temperature as sampled via normal distribution and 2nd order PCE coefficients. It can be seen from the figure that the distribution of the uncertain parameter given by the 2nd order PCE closely matches the one randomly sampled (with 10 x 10^6 sample points) from a normal distribution.

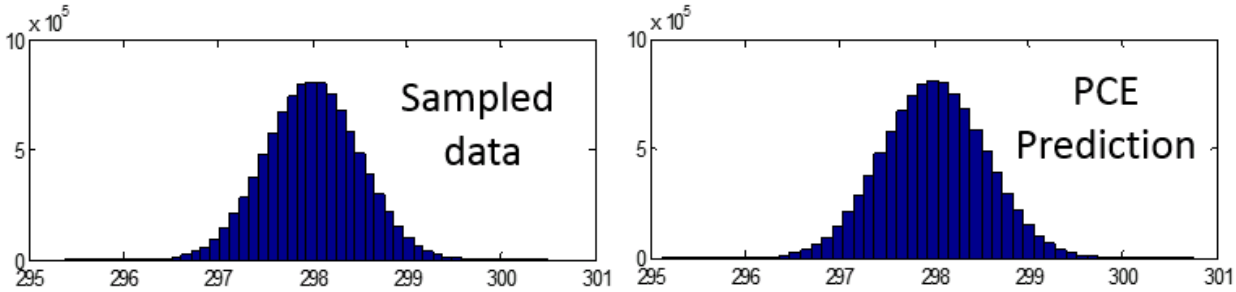

Figure 5.3: Histogram generated through MCS (left) and 2nd order PCE coefficient (right)

The next step of the IPC method is to reformulate the DAC model with PCE approximations, details of which can be found in APPENDIX C. The reformulated model is simulated to analyze the model outputs due to the input uncertainty. Figure 5.4 compares the mean CO_2 breakthrough curve at the channel exit and compares the results with MCS runs. It can be seen from the figure that model outputs converges to the results from MCS runs with IPC method. It can also be seen from the figure that the model has the same accuracy in predicting the output for 1st, 2nd and 3rd order of IPC methods, which can also be seen from R^2 values as listed in Table 5.2. The table also shows that IPC methods are much faster computationally as compared to MCS runs. Also, the increase in computational

time with the IPC order is not significant. This means that the system shows improved computational efficiency even if the model has converged with higher order of IPC.

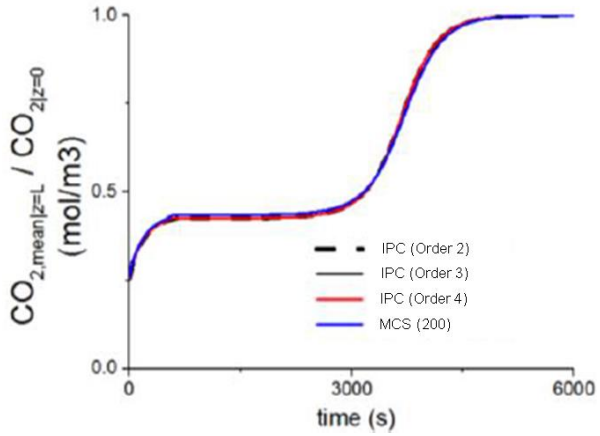

Figure 5.4: Comparison of IPC with MCS for one uncertain parameter using CO_2 breakthrough

Table 5.2: Computational statistics for IPC fit with one uncertain parameter

Method	Computational Time (s)	R^2
IPC (order 1)	100	0.9988
IPC (order 2)	140	0.9988
IPC (order 3)	170	0.9988
MCS	3500	-

5.3.2 Uncertainty in two parameters

In this section I discuss handling uncertainties in DAC system, when the uncertainty is present in two parameters which are not correlated. I have considered uncertainty in inlet velocity, N(3,0.5) and inlet temperature, N(298,1.0). The IPC method was implemented for the two uncertain parameters in a similar procedure as discussed in the previous section (for one uncertain parameter). Figure 5.5 shows the model outputs obtained through IPC methods and MCS runs, which shows IPC of the second and third order converge with the MCS runs. It can be seen from Table 5.3 that IPC methods have a good fit and took less computational time as compared to the MCS runs.

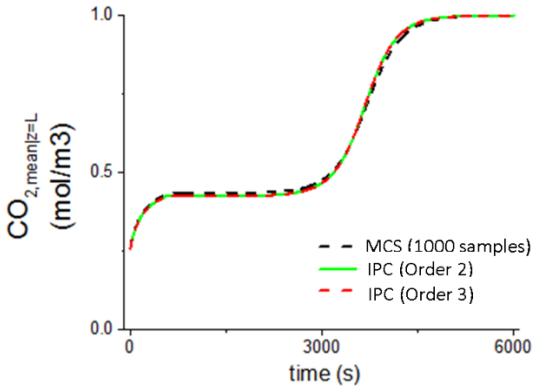

Figure 5.5: Comparison of IPC with MCS for two uncertain parameters using CO_2 breakthrough

Table 5.3: Computational statistics for IPC fit with two uncertain parameters

Method	Computational Time (s)	R^2
IPC (order 2)	450	0.9987
IPC (order 3)	510	0.9988
MCS	48550	-

The NIPC method was implemented for the same two uncertain parameters (inlet velocity – N(3,0.5) and inlet temperature – N(298,1.0)). The input parameters were sampled through Latin hypercube sampling technique and the model outputs converged using the 4^{th} order and 5^{th} order of the NIPC methods. Figure 5.6 shows the model outputs using the 4^{th} and 5^{th} order of the NIPC methods with different sampling points. It can be seen from the figure that increasing the sampling points increases the accuracy of convergence for both 4^{th} and 5^{th} order of the NIPC. This can also be confirmed from Table 5.4 which lists the R^2 values for all the sampling points.

Table 5.4 also lists the speed up factor for different methods which is defined by the following equations:

$$\text{speed up factor} = \frac{\text{Number of MCS runs}}{\text{Number of NIPC runs}} \tag{31}$$

It can also be seen from the table that there is a trade-off between the speed up factor and the convergence of the NIPC methods with the MCS runs. For the 4^{th} order, the speed up factor was found to be 24 (42 sampling points), and that for the 5^{th} order was 8 (120 sampling points), comparing those which have the value of R^2 above 0.99. Here, it should be noted that a higher speed up factor requires less computational time, while a higher R^2 has more accuracy. Depending on the process requirement, an appropriate NIPC method and sampling order should be chosen for quantifying the uncertainty.

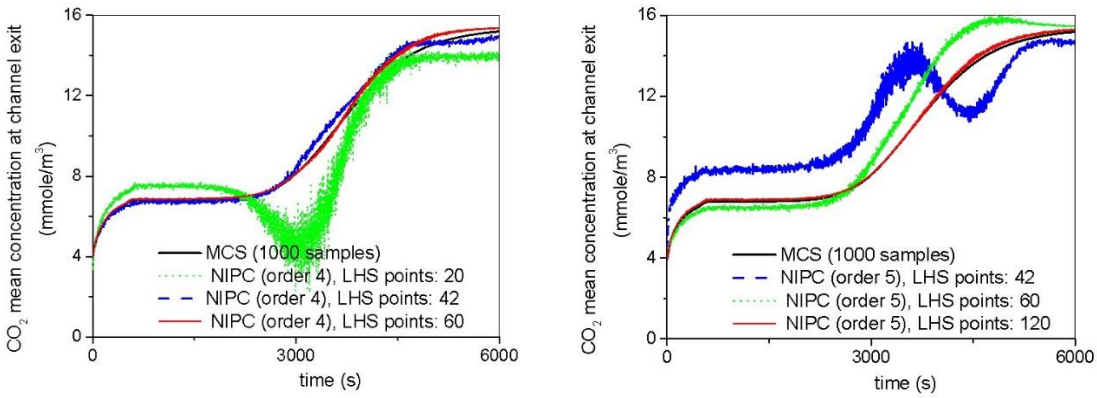

Figure 5.6: Effect of increase in NIPC sample points for order 4 (left) and order 5 (right)

Table 5.4: Computational statistics for NIPC fit with two uncertain parameters

Method	Speed up Factor	R^2
Order 4		
NIPC (20 samples)	50	0.8416
NIPC (42 samples)	24	0.9924
NIPC (60 samples)	17	0.9991
MCS	1	-
Order 5		
NIPC (42 samples)	24	0.7939
NIPC (60 samples)	17	0.9788
NIPC (120 samples)	8	0.9997
MCS	1	-

5.3.3 Uncertainty in three parameters

In this section, I discuss handling uncertainty when the uncertainty is present in three parameters which are correlated. I consider uncertainties in mass transfer coefficient (*k*), inlet velocity (*v*) and CO_2 diffusivity (*D*) inside the adsorbent. The correlation coefficient, ρ, is used to quantify the correlation between uncertain parameters as defined in Eq. 32.

$$\rho = \frac{n\sum x_1 x_2 - \left(\sum x_1\right)\left(\sum x_2\right)}{\sqrt{n\left(\sum x_1^2\right) - \left(\sum x_1\right)^2}\sqrt{n\left(\sum x_2^2\right) - \left(\sum x_2\right)^2}} \tag{32}$$

where *n* is the number of pairs of uncertain parameters and x_1 and x_2 are the two uncertain parameters whose correlation is being calculated.

The correlation between each pair of the three uncertain parameters *k, v,* and *D* is plotted in Figure 5.7. It can be seen from the figure that there is high correlation between diffusivity and the mass transfer coefficient, mild correlation between inlet velocity and mass transfer coefficient and almost no correlation between inlet velocity and diffusivity. This can be further confirmed from Eq. 33 which calculates the correlation coefficient matrix for the three uncertain parameters.

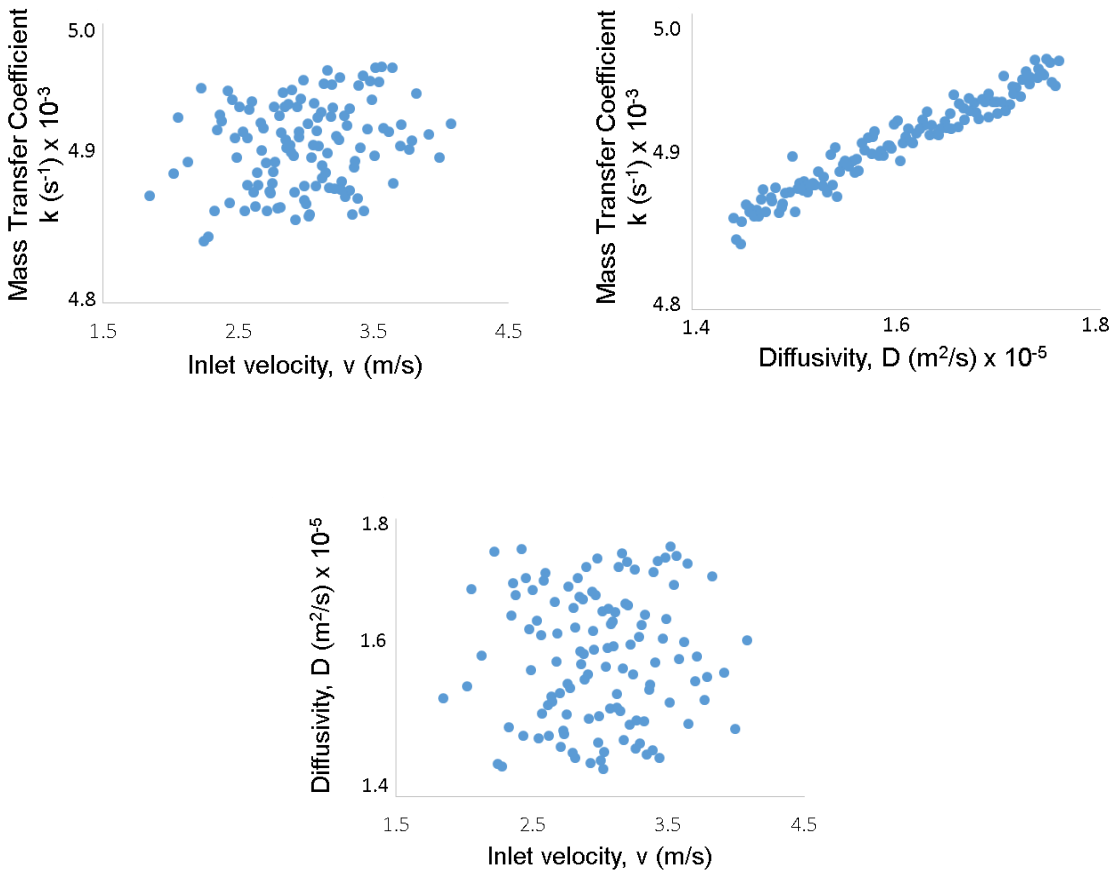

Figure 5.7: Correlation illustration between the three uncertain parameters

$$\rho = \begin{array}{c} \begin{matrix} v & k & D \end{matrix} \\ \begin{bmatrix} 1 & 0.27 & 0.08 \\ 0.27 & 1 & 0.97 \\ 0.08 & 0.97 & 1 \end{bmatrix} \end{array} \begin{matrix} v \\ k \\ D \end{matrix} \tag{33}$$

In order to implement NIPC method on the correlated uncertain parameters, the parameters need to be transformed so that they become uncorrelated, since the polynomial chaos methods works only if all parameters are not correlated. I used the Nataf transformation to resolve all parameter correlations. Figure 5.8 shows the correlation between the parameters

after application of the Nataf transformation. It can be seen from the figure that the correlation between the parameters have been removed. This can be further confirmed from the Eq. 34 which computes the correlation coefficient matrix between the uncertain parameters.

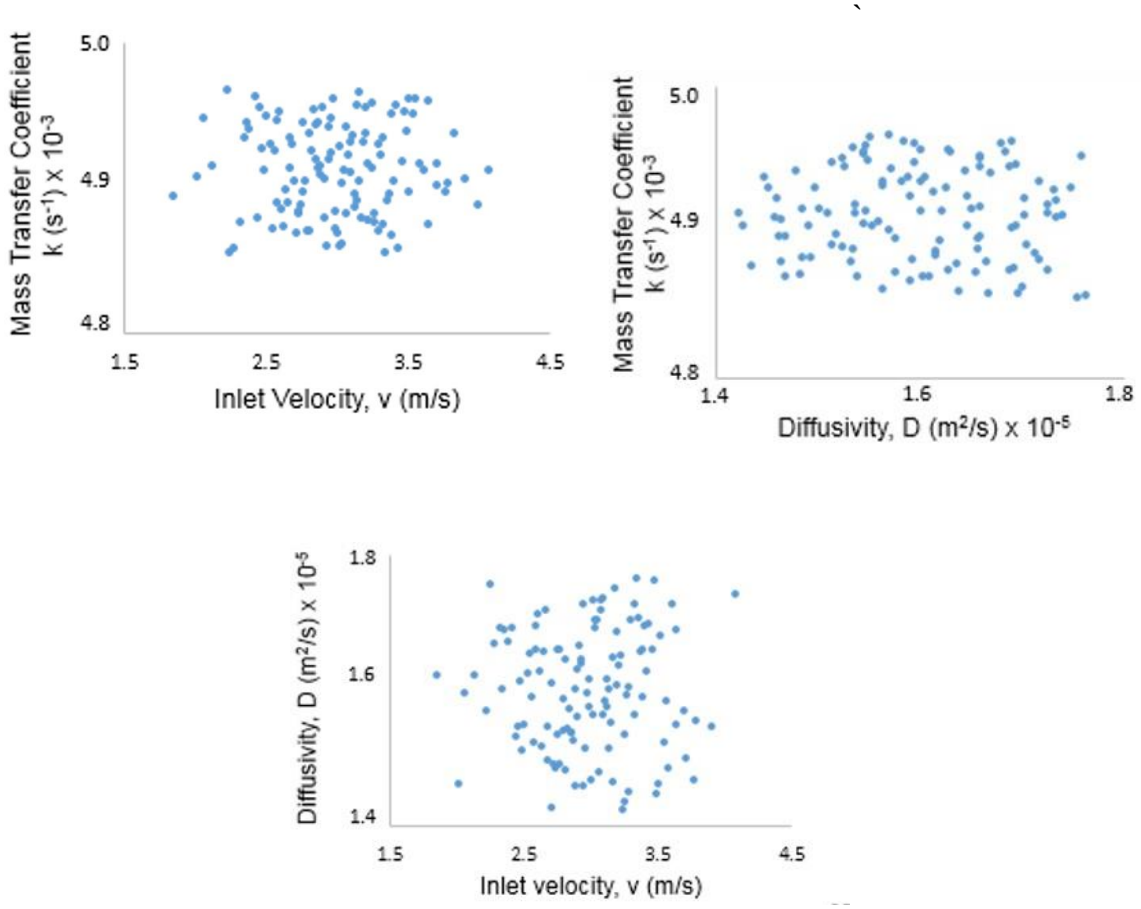

Figure 5.8: Nataf transformation on the correlated parameters

$$\rho = \begin{array}{c} \begin{matrix} v & k & D \end{matrix} \\ \begin{bmatrix} 1 & 0 & 0 \\ 0 & 1 & 0 \\ 0 & 0 & 1 \end{bmatrix} \end{array} \begin{matrix} v \\ k \\ D \end{matrix} \tag{34}$$

The uncorrelated uncertain parameters were quantified using NIPC methods with different sampling points as shown in the Figure 5.9. It can be seen from the figure that the NIPC method with the order of 4 and 5 shows good convergence with 60 and 120 sampling points respectively. This can be further seen from Table 5.5 which shows the speed up factor and the R^2 values of NIPC method and compares it with the MCS runs. It can be seen from the table that there is a trade-off between the speed up factor and the accuracy of fitting (R^2).

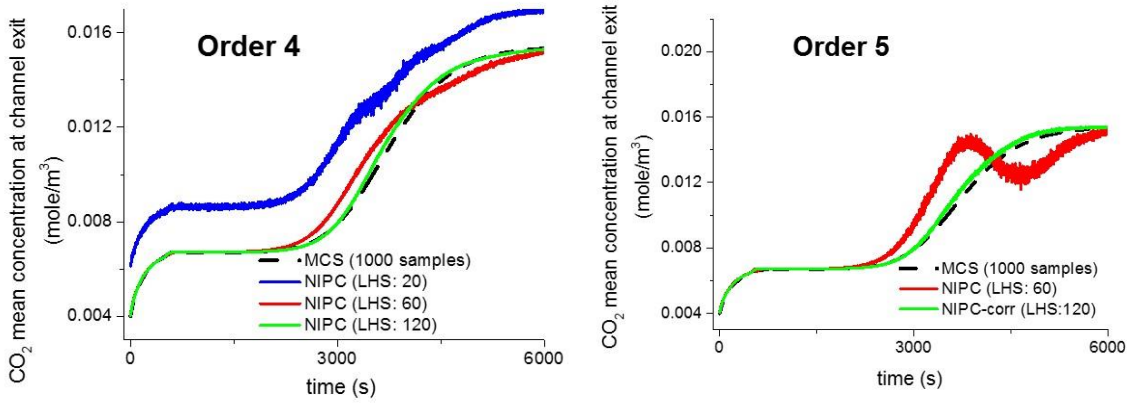

Figure 5.9: Effect of NIPC order for three uncertain parameters

Table 5.5: Computational statistics for NIPC fit with three uncertain parameters

Method	Speed up Factor	R^2
Order 4		
NIPC (20 samples)	50	0.9751
NIPC (60 samples)	17	0.9851
NIPC (120 samples)	8	0.9986
MCS	1	-
Order 5		
NIPC (60 samples)	17	0.8594
NIPC (120 samples)	8	0.9985
MCS	1	-

5.4 Application in CO_2 capture from enclosed air

In Chapter 4, I modeled the CO_2 capture system inside enclosed environments. However, the assumption of single valued parameters may not hold true in real life situations, because of the inherent uncertainty and because some of the input parameters will have distributions. For example, in estimating the CO_2 energy requirements and footprint of office space of 45 million sq. m (similar to New York), it was assumed that the total space is a collection of large numbers of rooms with fixed size. In order to maintain air quality in each of these rooms, I assumed fixed size of the air conditioning system with the same fixed number of people occupying the room all day. In reality, the assumption that large office rooms can be divided into spaces with fixed size does not hold true. Similarly, the number of people occupying the room during different days may vary.

In order to quantify the uncertainties discussed above, it is important to perform sensitivity analysis of these input parameters and analyse their impact on the model outputs. In this section I have analyzed uncertainty associated with CO_2 capture from the enclosed environments by performing the sensitivity analysis on the uncertain parameters and then quantifying the uncertainty in the outputs.

5.4.1 Sensitivity Analysis

I performed sensitivity analysis on number of people inside the room to analyze its impact on model output. The number of people inside the room is varied between 3 to 6 people (a resulting spatial density between 3 to 17 m^2 per person). Non-integer values of people are possible since this represents average number of people occupying the room during the entire day. Figure 5.10a shows the effect of people density on CO_2 concentration dynamics

inside the room. The system is analyzed during office hours (9 AM – 5 PM). It can be seen from the figure that the peak CO_2 concentration inside the room increases with an increase in the density of people. This is because, keeping other parameters fixed, increase in people density increases the respiration dynamics inside the room. Hence the peak CO_2 concentration increases since the monolithic system can remove a fixed amount of CO_2.

I have also performed sensitivity analysis on the room size, varying it from 4×4×2.3 (~37) m^3 to 6×6×2.6 (~128) m^3. Figure 5.10 b shows the effect of room volume on CO_2 concentration dynamics inside the room. It can be seen from the figure that time to reach the peak concentration increases with increase in room volume. The room with the lowest volume reaches the peak concentration within 8 hour period while the room with highest volume has still not reached the peak concentration yet. All the cases if simulated for a longer period of time reaches the same peak CO_2 concentration. This is because I have assumed fixed number of people in this analysis. This ensures fixed respiration dynamics within the room and fixed amount of CO_2 being removed from the monolithic system. The variation in room volume varies the time taken to reach the steady state (peak concentration).

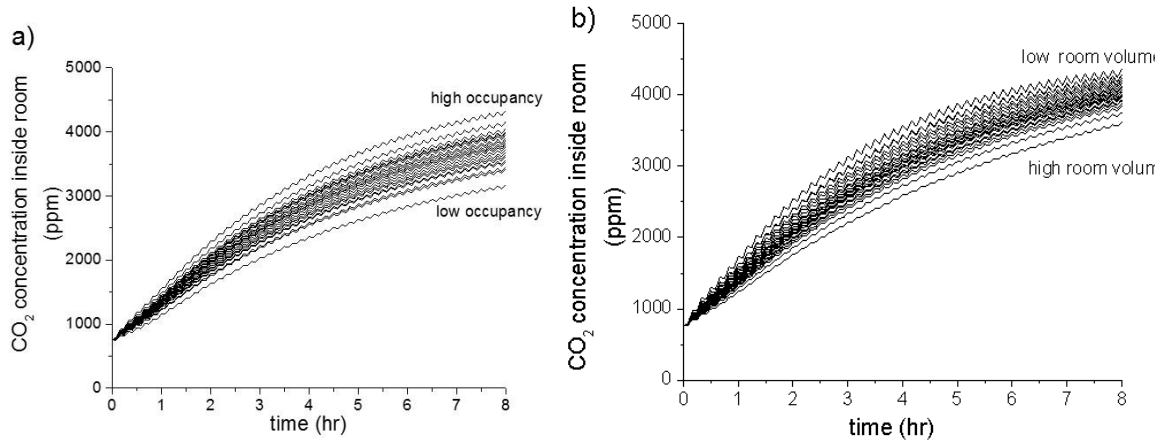

Figure 5.10: Variation of CO_2 concentration inside room with a) room size and b) people density

The discussion above shows that room volume and people density are both sensitive parameters with regards to CO_2 concentration dynamics inside the room.

5.4.2 Uncertainty quantification

In the previous section, sensitivity due to room volume and people density was discussed individually. However for a complete analysis, sensitivity due to both these parameters needs to be analysed together. A small room with high people density may represent conference and meeting rooms where large number of people sit in a confined space. On the other hand, large room with low people density may represent building lobby and other large areas which remain vacant or less occupied with people during most of the time. All the other combinations of room volume and people density between these two extremes may represent numerous scenarios.

In order to quantify the uncertainty in the room size and number of people, I have compared the performance of NIPC methods with MCS runs. I have assumed a Gaussian distribution of room volume with a mean of 82 m^3 and a standard deviation of 19. Similarly, I have assumed Gaussian distribution of people with a mean of 4 people and a standard deviation of 0.5. The NIPC method is performed on the air conditioning system with different number of sampling points and the comparison is made with MCS runs with 500 sampling points. Figure 5.11 shows the CO_2 concentration dynamics inside the rooms and compares the result when the computation is performed through MCS and NIPC of order 2 with 10, 20 and 40 sampling points. It can be seen from the figure that increase in sampling points increases the convergence of NIPC method with MCS runs since coefficient of regression (R) reaches unity when sampling points increases from 10 to 40.

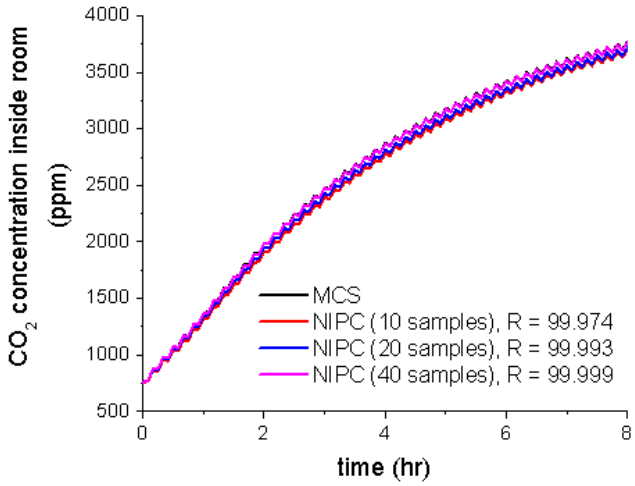

Figure 5.11: Mean CO_2 concentration inside room

Table 5.6 compares the performance of NIPC method with the MCS runs. It can be seen from the table that the computational time incurred due to MCS runs are much higher than NIPC methods. Depending on the accuracy required, the number of sampling points for

the NIPC method can be chosen. It can be seen from the table that the accuracy in the model outcome (Energy) increases as the sampling points of NIPC method increases from 10 to 40. Hence, NIPC method can be used to predict and evaluate model outcomes instead of MCS runs to improve the model's computational efficiency and speed up factor.

Table 5.6: Comparison between MCS and NIPC results

		Speed up Factor	**Computational time (s)**	**Energy (MJ/mole)**
NIPC (Order 2)	**10 samples**	50	375	1.30
	20 samples	25	770	1.28
	40 samples	12	1570	1.25
MCS		1	21210	1.25

5.5 Conclusion

In this chapter I presented a strategy to quantify uncertainty through PCE methods. The basic mathematical formulation of the IPC and NIPC methods were discussed and the implementation of the methods on a CO_2 capture system was explained. PCE methods were analyzed for the DAC and enclosed systems. The results indicate that IPC methods are

computationally most efficient since they require single iteration of the modified deterministic model to generate the outputs. The IPC methods are beneficial for optimization under uncertainty since it removes the uncertainty in the original model through Galerkin projections. However, the major disadvantage of the IPC method is that it becomes challenging to formulate for multi-dimensional uncertainty in the input parameters. This is because converting the original model to PCE framework through orthogonal projections becomes increasingly difficult with the increase in the number of uncertain input parameters.

The results obtained through NIPC methods indicate that these methods have a higher speed up factor than MCS runs, and they can generate outputs with a similar accuracy as MCS runs with an appropriate NIPC order and number of sampling points. It is also found that there is a trade-off between the speed up factor and the model accuracy. Hence, based on the process requirements, the NIPC order and number of sampling points should be decided. NIPC methods are easier to formulate as compared to IPC methods since NIPC methods do not require transformation of the original deterministic model. However, NIPC methods are less efficient in terms of computational time as compared to IPC methods.

The work done in this chapter lays foundation of uncertainty quantification in gas separation based systems through PCE methods. These methods needs to be further explored to study the effect of uncertainty when there are more than three uncertain parameters. In addition, optimization and design under uncertainty using PCE methods needs to be explored to minimize and constraint the sensitivity of systems due to parametric uncertainties.

CHAPTER 6. CONCLUSIONS AND FUTURE WORK

6.1 Outlook

The rising CO_2 concentration in the atmosphere has created an imperative for research into CO_2 mitigation technologies. The work done in this thesis was motivated by the concept of capturing CO_2 directly from the atmosphere, thereby targeting CO_2 emissions from dispersed sources and providing a long term route to reducing CO_2 concentrations in the atmosphere. The economics of capturing CO_2 from the air has been much debated in previous literature. There has been concern on the cost, size and energy consumption of systems designed to capture significant amounts of CO_2 from the air [31, 177]. However, these studies and reviews have either considered a single process design, and then extrapolating the conclusions for entire array of possibilities of process designs for the DAC, or they have concluded the high economics of DAC based on preliminary calculations without performing a detailed techno-economic analysis based on fully functional process model. There have also been studies [34, 86] which concludes optimistic performance of the DAC processes and proposes extensive research in this area to establish DAC as one of the favorable ways of mitigating CO_2 levels from the atmosphere. Clearly the debate is not settled.

Recently, MOFs have been synthesized which have shown high capacity for CO_2 capture under ambient CO_2 concentrations[8-9]. With the advent of efficient synthesis methods and highly tunable properties of these MOFs, it is expected that even higher capacity and more stable MOFs can be synthesized in future. The work performed in this thesis has been

inspired by the optimistic studies on the DAC processes to explore further the use of solid adsorbents in cyclic adsorption processes.

Another topic where the methodologies developed for DAC can be applied is to study the economics of capturing CO_2 from enclosed environments. This presents an additional benefit of reducing the CO_2 levels inside the enclosed space, such as commercial buildings, to ensure comfort of building occupants. Enclosed air capture can also help in reducing the load on the HVAC systems and hence improve building energy efficiency. Exploring the methodologies for improvement in energy consumptions inside buildings has been a widely researched area [89-90]. The work proposed in this thesis on enclosed air capture is motivated by the lack of substantial research on improving building energy efficiency through CO_2 removal techniques. With the work presented in this thesis, it is found that the CO_2 removal through solid adsorbents in the enclosed space can help in modifying conventional HVAC systems and reduce overall energy consumption.

The process models developed for DAC and enclosed air capture are often subject to parametric uncertainties. Quantification of these uncertainties is necessary for more useful model predictions. There have been substantial research on methods used for handling model uncertainties [130-131]. PCE is one such method, on which, there has been limited research particularly on processes with gas separations. The uncertainty quantification work performed in this thesis expands the research front of PCE in the areas of CO_2 capture systems.

6.2 Summary

This results presented in this thesis have met the three main objectives listed below:

1. Design of a class of DAC processes to analyze the energetics and techno-economics of CO_2 capture from air through solid adsorbents.
2. Extension of the DAC adsorption model to analyze performance of CO_2 capture systems in enclosed environments with multi-bed simulation.
3. Establishment of PCE based methods for CO_2 capture systems and comparison of their performance with Monte Carlo Simulations.

The first objective is discussed in detail in Chapters 2 and 3 of this thesis. In Chapter 2, two MOFs (MIL-101(Cr)-PEI-800 [8] and mmen-Mg_2(dobpdc) [9, 51]) are considered to study the design and economics of DAC processes. The MOFs are coated as films inside monolithic support structure and steam is used as the stripping agent for the removal of CO_2 during the desorption process. A TVSA model is proposed to simulate the process comparing the performance of both the MOFs for DAC. Systems design and operating parameters are fixed and a detailed energy and cost analysis is performed for both the adsorbents with the assumption of equilibrium sorption behavior and a linear driving force model based on mass transfer resistances. The modeling outcome shows that the net primary combustion energy used for MIL-101(Cr)-PEI-800 and mmen-Mg_2(dobpdc) are 0.225 and 0.158 MJ/mole respectively. These values are less than the heat of combustion that generated the CO_2 (0.45 MJ/mole). The net cost (which has taken both the capital and operating cost into consideration) of the DAC process is found to be around $ 95-160 per tonne of CO_2 captured for MIL-101(Cr)-PEI-800 if the lifetime of the adsorbent is assumed

to be between 1 to 3 years. The net cost of DAC with mmen-Mg_2(dobpdc) as the adsorbent is found to be $ 75-200 per tonne of CO_2 captured for the same range of adsorbent's lifetime.

Based on the methodology developed in Chapter 2, a parametric analysis of DAC for solid sorbents is presented in Chapter 3. A hierarchical based approach is followed to vary the parameters of the DAC process and the sensitivity of the model with regards to energetics and techno-economics is analyzed for these parametric variations. The results indicate that adsorbent purchase cost and its lifetime plays a major role in determining the overall cost of the DAC process. The analysis presented in this chapter also provides bounds on the parameters which can be referenced in future synthesis of novel adsorbents and design of CO_2 capture systems. It is also found that the DAC process has a lower carbon footprint for the electrical energy component as compared to the thermal component. In addition, flux and energy intensity analysis has been performed for the DAC process. It is concluded that a typical DAC plant will have a higher flux and consume lower energy intensity as compared to a tropical tree.

The second objective of this thesis is discussed in Chapter 4. This chapter analyzes a multi-component, multi-bed model to lower down the CO_2 concentration inside enclosed space such as commercial buildings. Modeling results indicate a reduction in energy consumption of the buildings with the enclosed air capture as compared to the conventional ventilation systems. CO_2 emissions caused due to the enclosed air capture system is studied by scaling up the system to the size comparable to the total office inventory of New York and the carbon footprint of the process is analyzed and compared with the conventional ventilation system for different source of generation of electricity. It is found that replacement of the

conventional ventilation system with the enclosed air capture (for the scale up study) can help in reducing the CO_2 emissions equivalent to 92.3 million incandescent lamps switched to LEDs or 6.4 million barrels of oil consumed. It is also concluded that an adsorbent that is stable against water and has high capacity can help in further bringing down cost of the enclosed air capture system.

The third objective of the thesis is discussed in Chapter 5. This chapter discusses different PCE methods for uncertainty quantification in DAC as well as enclosed air capture process. The IPC method shows faster computational speed as compared to other methods (NIPC and MCS). However, it is found that the IPC methods becomes increasing complex to formulate with increase in the number of uncertain parameters. The NIPC method is found easier to implement compared to IPC method and has a higher speed up factor as compared to MCS runs but slower compared to the IPC. The chapter also discusses strategies to handle correlation between the uncertain parameters through the application of Nataf transformation. For both DAC and enclosed air capture the PCE methods shows good convergence and higher computational efficiency as compared to the MCS runs.

6.3 Future work

6.3.1 Extensive kinetic study of CO_2 uptake on the adsorbent

The DAC study performed in this thesis assumes a fixed mass transfer coefficient for the two MOFs (MIL-101(Cr)-PEI-800 and mmen-Mg_2(dobpdc)). Since the kinetics of CO2 uptake on these MOFs have not been properly established experimentally, the mass transfer coefficient for these MOFs are calculated based on the diffusivity of CO_2 in other MOF crystals that are found in existing literature. Utilizing the information about the diffusivity

studies, the mass transfer coefficient calculations have been performed using empirical relations for monoliths found in the literature [71].

Recent experimental studies [178] have shown that the CO_2 adsorption on mmen-Mg_2(dobpdc)) may have different saturation capacity depending on the flow rate of the inlet gas (in addition to the S shaped isotherm behavior). Hence the adsorption dynamics may not be best represented by a LDF model. Instead, Avrami's model [179] where the mass transfer coefficient is time dependent may be more suitable for explaining the CO_2 uptake on this adsorbent. However, further study needs to be performed to establish this phenomenon and additional experimental investigation needs to be performed to examine the behavior of the adsorbent during desorption conditions. Such studies will help in accurately representing the adsorption/desorption dynamics of CO_2 on this adsorbent which will provide more accurate energetics and techno-economic analysis. This may point to a tradeoff in DAC systems between having low temperature regeneration, 80-90C which uses low grade heat, and fast kinetics that controls the adsorption and desorption times and hence the system capital costs. The selection of the adsorbent may be driven more by the kinetics of desorption than by the maximum equilibrium capacity.

6.3.2 Further exploration of DAC techno-economics

The relative ease of synthesis of MOFs, coupled with the structural and functional tunability of their properties, has made MOF research one of the fastest growing areas in synthetic chemistry. With new MOFs constantly being reported in the literature, the DAC study needs to be explored to incorporate MOFs with higher CO_2 equilibrium capacity, fast kinetics, longer lifetime and better stability under humid conditions. Further, the work

performed in this thesis (Chapter 3) has analysed the techno-economics of DAC for different combination of temperature and vacuum swing combinations with numerous variations of systems design and operating parameters. Utilizing the methodology presented in this thesis, optimization studies needs to be performed on the DAC model to further establish the favourable role of DAC in CO_2 mitigation strategies.

The thickness of adsorbent growth on the support structure has also been identified a key area of future research in this thesis, since the ratio of contactors to adsorbent has significant effect on the techno-economics of the DAC process. Stable growth of thicker adsorbents over thinner monolithic walls needs to be established experimentally in order to improve the economics of DAC through solid adsorbents.

The use of 3-D printed monolith structures also enables further optimization of the DAC system. In particular the geometry of the channel along the contactor and the amount of adsorbent per unit length could be optimized to improve performance. For example, the thickness of the MOF film could be varied along the channel by growing it on smaller sections of the monolith that are then assembled into a longer monolith. This would allow for higher density of adsorbent at the entrance of the channel which will see CO_2 for longer and hence the slower kinetics will be less of a limitation.

We can consider what solar collection area would be required to power the capture system – for example we could use PV at 20% efficiency and parabolic trough mirror systems at 70% efficiency to provide the power and heat and then have this area integrated into the system. Note that the PV array could be integrated with the collectors by being mounted

on top but also in between the rows of the collectors since they need to be spaced apart any way.

6.3.3 Extending enclosed air capture to other applications

The enclosed air capture analysed in this thesis (Chapter 4) focuses on energy reduction pathways inside commercial buildings and suggests strategies to reduce the carbon footprints of office spaces by comparing the proposed methods with the conventional ventilation system. However, the enclosed air capture has a broader applications in addition to buildings such as submarines and space shuttles. The CO_2 adsorption through 3D monoliths can be extended to such applications by understanding the key limitations in these areas and modeling the carbon capture processes that caters to the specific needs of these systems. For example, if the loss of carbon from the system can be tolerated in short space flights, then vacuum desorption into space can provide an essentially free desorption step.

Handling uncertainty in enclosed air capture should be further explored to introduce uncertainty quantification on correlated uncertain parameters. The system performance will be sensitive to the rate of generation of CO_2 and H_2O which are related to the number of people in the room and their rates of respiration. The number of people will be time varying and this will create spikes in the CO_2 concentration that must be managed. Design of the system to be robust to these uncertain variations is a challenge and should be further explored.

6.3.4 Optimization under uncertainty

The uncertainty quantification performed in this thesis (Chapter 5) discusses implementation of PCE methods and establishes the superior performance of these methods over the MCS runs in terms of the accuracy of the approximation of the distribution of performance and computational effort. This opens a huge opportunity of future research in optimizing the CO_2 capture processes under uncertainty with PCE methods employed to quantify the uncertainties and provide more rapid evaluation of objective function values under uncertainty. This can be achieved by formulating an optimization problem such that the objective function and the constraints are polynomial approximations of some model outputs of interest. The optimization problem can be approached using different techniques and methods used in solving the uncertainty model [180]. One such strategy is to minimize the net cost of the DAC process under uncertainty, keeping constraints on purity. The optimization problem is presented below:

$$\min_{v_1, v_2, t_1, t_2} \text{E (CAPEX + OPEX)}$$

s.t

$$P\left(g(\text{x}) \leq 0\right) \geq \text{P}_0$$

Objective function consists of uncertain parameters. For example:

$$\text{Blower OPEX} = \Delta P \pi R_1^{\,2} v_{ads} t_{ads} C_E$$

where

$$v_{ads} = \sum_{j=0}^{P} v_j \psi_j(\xi)$$

g(x) is defined below:

$$g(x) = \text{Purity} - \gamma$$

$$\text{Purity} = \frac{\int_{t_{step1}}^{t_{step3}} C_{CO_2}(L)v(L)dt}{\int_{t_{step1}}^{t_{step3}} C_{CO_2}(L)v(L)dt + \int_{t_{step1}}^{t_{step3}} C_{N_2}(L)v(L)dt}$$

Purity also contains uncertain variables such as $v(L)$ and $C_{CO2}(L)$. These variables can be computed in a deterministic framework through IPC methods. Details of model formulation through IPC method is provided in APPENDIX C.

APPENDIX A.

Heat and Mass Balance Equations for CO_2 capture using monoliths:

A three component system comprised of CO_2, inert gas (N_2 and O_2) and water vapor is considered. *CO_2, inert* and *H_2O* are used as subscripts in the model equations for defining these three components, respectively, and *r* and *z* are used to denote radial and axial domains, respectively.

$$\frac{\partial C_{CO_2}}{\partial t} + v\frac{\partial C_{CO_2}}{\partial z} + C_{CO_2}\frac{\partial v}{\partial z} = D_{CO_2}\left[\frac{1}{r}\frac{\partial}{\partial r}(r\frac{\partial C_{CO_2}}{\partial r}) + \frac{\partial^2 C_{CO2}}{\partial z^2}\right] \tag{35}$$

$$\frac{\partial C_{inert}}{\partial t} + v\frac{\partial C_{inert}}{\partial z} + C_{inert}\frac{\partial \mathrm{v}}{\partial z} = D_{inert}\left[\frac{1}{r}\frac{\partial}{\partial r}(r\frac{\partial C_{inert}}{\partial r}) + \frac{\partial^2 C_{inert}}{\partial z^2}\right] \tag{36}$$

$$\frac{\partial C_{H_2O}}{\partial t} + v\frac{\partial C_{H_2O}}{\partial z} + C_{H_2O}\frac{\partial \mathrm{v}}{\partial z} = D_{H_2O}\left[\frac{1}{r}\frac{\partial}{\partial r}(r\frac{\partial C_{H_2O}}{\partial r}) + \frac{\partial^2 C_{H_2O}}{\partial z^2}\right] \tag{37}$$

where *C* and *D* are the concentration and diffusivity of the gaseous components in the channel, respectively, and *v* is the velocity of gas inside the channel. The Hagen Poiseuille equation is used to estimate the gas velocity (eq. 38) inside the channel:

$$v = \frac{1}{4\mu}\frac{\partial P}{\partial z}\left(r^2 - R_1^{\,2}\right) \tag{38}$$

where P is the total pressure inside channel, μ is the gaseous viscosity and R_1 is channel inner radius. Both axial and radial components are taken into account while estimating the gas velocity inside the channel.

To estimate the overall mass transfer coefficient, the following correlations are used, [71] in which the effect of internal, and external mass transfer resistances, are taken into account:

$$k_i = \frac{4D_e}{\left[(r_0/r_i)-1)(r_o^2-r_i^2)-(1/r_i(r_o-r_i)\right]\left[(1/2)(r_o^4-r_i^4)-(4r_o/3)(r_o^3-r_i^3)+r_o^2(r_o^2-r_i^2)\right]} \quad (39)$$

$$k_e = \frac{2.696D[1+0.139(2R_1/L)\,\mathrm{ReSc}]^{0.81}}{2R_1} \quad (40)$$

$$\frac{1}{k} = \frac{1}{k_i} + \frac{1}{k_e} \quad (41)$$

where k_i, k_e and k are the internal, external and overall mass transfer coefficient coefficients respectively, D is the molecular diffusivity in the gas phase and D_e is the effective diffusivity inside the adsorbent.

The initial and boundary conditions for the CO_2, inert gas and water vapor concentrations are given in Table A.1. $C_{CO2}(0)$ and $C_{inert}(0)$ are the ambient air concentration and $C_{H2O}(0)$ corresponds to 25% humid air during the adsorption step. $C_{CO2}(1)$ and $C_{inert}(1)$ are air concentrations at the desorption step, which are negligible, and $C_{H2O}(1)$ corresponds to concentration of low grade saturated steam during the desorption step.

Table A.1: Initial and boundary conditions for CO_2, inert gas and water components (i = CO_2, inert, H_2O).

Initial conditions
$C_{i\|t=0} = C_i(0)$
Axial Boundary conditions
$C_{i\|z=0} = C_i(0)$ [Adsorption]
$C_{i\|z=0} = C_i(1)$ [Desorption]
$\frac{\partial C_i}{\partial z}_{\|z=L} = 0$
Radial Boundary conditions
$\frac{\partial C_i}{\partial r}_{\|r=0} = 0$
$-D_{CO_2} \frac{\partial C_{CO_2}}{\partial r}_{\|r=R_1} = \rho_{ads} k \left(Q^{eq}{}_{CO_2} - Q_{CO_2} \right)$
$D_{inert} \frac{\partial C_{inert}}{\partial r}_{\|r=R_1} = 0$

$$-D_{H_2O}\frac{\partial C_{H_2O}}{\partial r}_{|r=R_1} = k_m\left(C_{H_2O} - C^{i}{}_{H_2O}\right)$$

For defining the heat balance of the TVSA model, three components comprised of the gas inside the channel, the adsorbent and the monolithic wall are considered and *gas*, *ads* and *wall* are used as subscripts in the mathematical equation to denote the gas phase, the adsorbent phase and the monolith phase, respectively. The differential energy balances are described by the following equations:

$$\rho_{gas} C_{p,gas}\left(\frac{\partial T_{gas}}{\partial t} + v\frac{\partial T_{gas}}{\partial z} + T_{gas}\frac{\partial v}{\partial z}\right) = k_{gas}\left[\frac{1}{r}\frac{\partial}{\partial r}(\mathrm{r}\frac{\partial T_{gas}}{\partial \mathrm{r}}) + \frac{\partial^2 T_{gas}}{\partial z^2}\right] \tag{42}$$

$$A_1\rho_{ads}C_{p,ads}\frac{\partial T_{ads}}{\partial t} = A_1 k_{ads}\frac{\partial^2 T_{ads}}{\partial z^2} + A_1 Q_{gen} + H_{vap} - h\left(T_{ads} - T_{air}\right) + h\left(T_{wall} - T_{ads}\right) \tag{43}$$

$$A_2\rho_{wall}C_{p_{wall}}\frac{\partial T_{wall}}{\partial t} = A_2 k_{wall}\frac{\partial^2 T_{wall}}{\partial z^2} + h\left(T_{ads} - T_{wall}\right) \tag{44}$$

where ρ, C_p, k and h denotes the density, specific heat capacity, thermal conductivity and heat transfer coefficient respectively, A_1 and A_2 are the specific surface area for the adsorbent and the wall, respectively, and T denotes the temperature. Q_{gen} is the adsorption heat, which is defined as:

$$Q_{gen} = \Delta H\,\rho_{ads} k\left(Q^{eq}{}_{CO_2} - Q_{CO_2}\right) \tag{45}$$

In this equation, ΔH is the heat of adsorption. It is calculated using the Clausius−Clapeyron equation (eq. 46).

$$\left(\ln p\right)_{Q_{CO_2}} = \left(\frac{\Delta H}{R}\right)\left[\frac{1}{T}\right] + \mathrm{C} \tag{46}$$

where R is the gas constant. H_{vap} in eq. S47 is the heat released during condensation of water vapor. It is defined as:

$$H_{vap} = k_m \left(C_{H_2O} - C^{i}{}_{H_2O}\right) L^{vap}{}_{H_2O} \tag{47}$$

where k_m is the overall mass transfer coefficient[181] for water condensation over the MOF film and $L^{vap}{}_{H2O}$ is the latent heat of condensation of water vapor.

The adsorbent film and monolith wall gain heat and have higher temperatures during the desorption step due to condensation of steam. On the other hand, during the adsorption and cooling step, the reverse phenomenon takes place. The film and the wall lose heat (needed for water evaporation) and drop their temperatures to near ambient conditions. The initial and boundary conditions for the monolith channel, the adsorbent film and the wall are given in Table A.2, where T_0 is 298 K and 373 K during the adsorption and desorption steps, respectively.

Table A.2: Initial and boundary conditions for the gas, the adsorbent film and the wall.

Initial conditions (i = *gas*, *ads*, *wall*)
$T_{i\|t=0} = T_{ambient}$
Boundary conditions for gas
$T_{gas\|z=0} = T_o \quad ; \qquad \left.\frac{dT_{gas}}{dz}\right_{z=L} = 0$
$\left.\frac{dT_{gas}}{dr}\right_{r=0} = 0 \; ; \qquad -k_{gas}\frac{\partial T_{gas\|r=R_1}}{\partial r} = h\left(T_{gas} - T_{ads}\right)$
Boundary conditions for adsorbent and wall (j = *ads*, *wall*)
$k_j \frac{\partial T_{j\|z=0}}{\partial z} = h\left(T_{j\|z=0} - T_{ambient}\right)$
$k_j \frac{\partial T_{j\|z=L}}{\partial z} = h\left(T_{ambient} - T_{j\|z=L}\right)$

Table A.3 shows the velocity and total pressure boundary conditions for different steps of the TVSA cycle. During the adsorption and desorption step, both the ends of the channel are open. Evacuation and cooling steps involve closing the front end of the channel and

pulling a vacuum from the rear end of the channel. The pressurization step involves closing the rear end of the channel and pressurizing the channel (in finite steps, *p(t)*) by flowing steam from the front end. To implement these steps in the TVSA model, we propose three different sets of boundary conditions for the gas velocity and total pressure, as shown in Table A.3.

Table A.3: Boundary conditions for velocity and total pressure.

Adsorption/Desorption Step	Evacuation/Cooling Step	Pressurization Step
$v_{z=0} = v_{0,1}$ $\frac{\partial v}{\partial z}_{z=L} = 0$ $P_{z=0} = P_{high}$ $\frac{\partial P}{\partial z}_{z=L} = 0$	$v_{z=0} = 0$ $\frac{\partial v}{\partial z}_{z=L} = 0$ $\frac{\partial P}{\partial z}_{z=0} = 0$ $P_{z=L} = P_{high} - p(t)$	$v_{z=0} = v_{0,2}$ $v_{z=L} = 0$ $P_{z=0} = P_{low} + p(t)$ $\frac{\partial P}{\partial z}_{z=L} = 0$

APPENDIX B.

Heat and Mass Balance Equations for H_2O removal using packed beds:

The packed bed mass balance has four components, O_2, CO_2, H_2O and N_2. The mass balance equations for each of the components is given as:

$$\varepsilon \frac{\partial C_i}{\partial t} + \varepsilon v \frac{\partial C_i}{\partial z} = D \frac{\partial^2 C_i}{\partial z^2} - \rho_B \frac{\partial q_i}{\partial t} \tag{48}$$

where C_i is the concentration of the i^{th} gas component, ε is the bed porosity, ρ_B is the adsorbent bulk density, v is the gas velocity and D is axial dispersion coefficient. The amount of gas adsorbed q, is negligible for CO_2, O_2 and N_2. For H_2O, q is calculated using Eq. 49.

$$\frac{\partial q_{H_2O}}{\partial t} = K_p \left(q_{eq} - q \right) \tag{49}$$

where K_p is the mass transfer coefficient of H_2O on the silica gel pellets and q_{eq} is equilibrium concentration of the adsorbed H_2O as determined by the isotherm.

For defining the energy balance of the packed bed system, three components, gas, pellet and wall are considered. The differential energy balance is described by the following equations:

$$\rho_g C_{p,g} \left(\frac{\partial T_g}{\partial t} + v \frac{\partial T_g}{\partial z} \right) = k_g \frac{\partial^2 T_g}{\partial z^2} - \frac{2h}{R} \left(T_g - T_p \right) \tag{50}$$

$$\left(\varepsilon\rho_g C_{p,g} + (1-\varepsilon)\rho_p C_{p,\mathrm{p}}\right)\frac{\partial T_p}{\partial t} = k_p \frac{\partial^2 T_p}{\partial z^2} + \Delta H \rho_B (1-\varepsilon)\frac{\partial q_i}{\partial t} - \frac{2h}{R}\left(T_p - T_g\right) - \frac{2h}{R}\left(T_p - T_w\right) \quad (51)$$

$$\rho_w C_{p,w}\frac{\partial T_w}{\partial t} = k_w \frac{\partial^2 T_w}{\partial z^2} - \frac{2h}{R}\left(T_w - T_p\right) - \frac{2h}{R}\left(T_w - T_0\right) \quad (52)$$

where the subscripts *g*, *p* and *w* denotes gas phase, silica gel pellets and packed bed wall respectively, ρ_g is the gas density, ρ_g is the pellet density, *h* is the convective heat transfer coefficient, ΔH is the heat of adsorption of H_2O on silica gel pellets, *k* is the heat transfer coefficient, C_p is the heat capacity and T_0 is the temperature of the room. The initial and boundary conditions are provided in Table A.1, where C_0 is the concentration of gas inside the room which is entering the silica gel packed bed.

Table B.1: Initial and boundary conditions packed bed system

Initial conditions
$@t=0;\ q=0,\ C_i=0,\ T=T_{ambient}$
Axial Boundary conditions
$C_{i\|z=0}=C_0 \qquad \frac{\partial C_i}{\partial z}_{\|z=L}=0$
$T_{i\|z=0}=T_0 \qquad \frac{dT_i}{dt}_{z=L}=0$

APPENDIX C.

PCE construction

Let us consider a heat balance equation for the gas inside the monolithic channel.

$$\rho_g C_{p,g}\left(\frac{\partial T_g}{\partial t}+v\frac{\partial T_g}{\partial z}+T_g\frac{\partial v}{\partial z}\right)=k_g\left[\frac{1}{r}\frac{\partial}{\partial r}\left(\mathrm{r}\frac{\partial T_g}{\partial \mathrm{r}}\right)+\frac{\partial^2 T_g}{\partial z^2}\right] \tag{53}$$

where ρ, C_p, and k denotes the density, specific heat capacity and thermal conductivity and r and z are used to denote radial and axial domains, respectively. T and v denotes the temperature and gas velocity respectively and the subscript g refers to the gas phase inside the channel.

Assuming gas inlet velocity, v_0, as the only uncertain input parameter for the given case, all the output variables (such as v and T in eq. 42) becomes stochastic in nature. To this equation, I apply the PCE to these variables by introducing another domain, ξ to each of them in addition to the axial and radial domains. This is described as follows:

$$\begin{aligned} v &= v(\xi,z,r)=\sum_{i=0}^{P} v_i(z,r)\phi_i(\xi) \\ T &= T(\xi,z,r)=\sum_{j=0}^{P} T_j(z,r)\phi_j(\xi) \end{aligned} \tag{54}$$

where ϕ_i and ϕ_j are the basis functions for v and T respectively. Substituting eq. 54 in eq. 53, following equation is obtained:

$$\rho_{\mathrm{g}} C_{p,g}\left[\sum_{j=0}^{P}\Phi_j\frac{\partial T_{\mathrm{g,j}}}{\partial t}+\sum_{i=0}^{P}\sum_{j=0}^{P}v_i\Phi_i\Phi_j\frac{\partial T_{\mathrm{g,j}}}{\partial z}+\sum_{i=0}^{P}\sum_{j=0}^{P}T_{g,j}\Phi_i\Phi_j\frac{\partial \mathrm{v_j}}{\partial z}\right]= \\ k_{\mathrm{g}}\left[\sum_{j=0}^{P}\Phi_j\left(\frac{1}{r}\frac{\partial}{\partial r}\left(\mathrm{r}\frac{\partial T_{g,\mathrm{j}}}{\partial \mathrm{r}}\right)+\frac{\partial^2 T_{\mathrm{g,j}}}{\partial z^2}\right)\right] \tag{55}$$

I take orthogonal projection of the above equation with basis function ϕ_k . This is achieved by taking inner product on both sides of eq. 55 with ϕ_k as shown below:

$$\rho_g C_{p,g}\left[\sum_{j=0}^{P}\sum_{k=0}^{P}\langle\Phi_j\Phi_k\rangle\frac{\partial T_{\mathrm{g,j}}}{\partial t}+\sum_{i=0}^{P}\sum_{j=0}^{P}\sum_{k=0}^{P}\langle\Phi_i\Phi_j\Phi_k\rangle v_i\frac{\partial T_{\mathrm{g,j}}}{\partial z}\right]= \\ k_g\left[\sum_{j=0}^{P}\sum_{k=0}^{P}\langle\Phi_i\Phi_k\rangle\left(\frac{1}{r}\frac{\partial}{\partial r}\left(\mathrm{r}\frac{\partial T_{g,\mathrm{j}}}{\partial \mathrm{r}}\right)+\frac{\partial^2 T_{\mathrm{g,j}}}{\partial z^2}\right)\right] \tag{56}$$

The terms within the summation in the above equation can be computed numerically for a given basis function with a given probability distribution function.

Thus, I started with one equation (eq. 42) and after applying PCE, it transformed into a set of (P + 1) equations with expanded number of terms. Similar strategy is applied to rest of the model equations (including initial and boundary conditions).

REFERENCES

1. Yu, C.-H.; Huang, C.-H.; Tan, C.-S., A Review of CO2 Capture by Absorption and Adsorption. *Aerosol and Air Quality Research* **2012**.

2. Choi, S., Jeffrey H. Drese, and Christopher W. Jones., Adsorbent materials for carbon dioxide capture from large anthropogenic point sources. *ChemSusChem* **2009,** *2 (9)*, 796-854.

3. Siriwardane, R. V., Ming-Shing Shen, Edward P. Fisher, and James A. Poston., Adsorption of CO2 on molecular sieves and activated carbon. *Energy & Fuels* **2001,** *15 (2)*, 279-284.

4. Siriwardane, R. V., Ming-Shing Shen, Edward P. Fisher, and James Losch., Adsorption of CO2 on zeolites at moderate temperatures. *Energy & Fuels* **2005,** *19 (3)*, 1153-1159.

5. Brandani, F., and Douglas M. Ruthven., The effect of water on the adsorption of CO2 and C3H8 on type X zeolites. *Industrial & engineering chemistry research* **2004,** *43 (26)*, 8339-8344.

6. Furukawa, H., Kyle E. Cordova, Michael O'Keeffe, and Omar M. Yaghi., The chemistry and applications of metal-organic frameworks.". *Science* **2013,** *341 (6149)*, 1230444.

7. Liu, J.; Tian, J.; Thallapally, P. K.; McGrail, B. P., Selective CO2Capture from Flue Gas Using Metal–Organic Frameworks—A Fixed Bed Study. *The Journal of Physical Chemistry C* **2012,** *116* (17), 9575-9581.

8. Darunte, L. A., Oetomo, A. D., Walton, K. S., Sholl, D. S., Jones, C. W., Direct Air Capture of CO2 using Amine Functionalized MIL-101 (Cr). *ACS Sustainable Chemistry & Engineering* **2016,** *4*, 5761-5768.

9. McDonald, T. M.; Lee, W. R.; Mason, J. A.; Wiers, B. M.; Hong, C. S.; Long, J. R., Capture of carbon dioxide from air and flue gas in the alkylamine-appended metal-organic framework mmen-Mg2(dobpdc). *Journal of the American Chemical Society* **2012,** *134* (16), 7056-65.

10. Canadell JG, L. Q. C., Raupach MR, Field CB, Buitenhuis ET, Ciais P, Conway TJ, Gillett NP, Houghton RA, Marland G. , Contributions to accelerating atmospheric CO2 growth from economic activity, carbon intensity, and efficiency of natural sinks. . *Proceedings of the national academy of sciences.* **2007,** *104(47)*, 18866-70.

11. Intergovernmental Panel on Climate Change. Climate Change 2014: Mitigation of Climate Change. Vol. 3. Cambridge University Press, . **2015**.

12. Jones, C. W., CO2 capture from dilute gases as a component of modern global carbon management. *Annual review of chemical and biomolecular engineering* **2011,** *2*, 31-52.

13. Greenwood, K., and Pearce, M., The removal of carbon dioxide from atmospheric air by scrubbing with caustic soda in packed towers. *Trans Inst Chem Eng* **1953,** *31*, 201–207.

14. Spector, N. A.; Dodge, B. F., Removal of carbon dioxide from atmospheric air. *Transactions of the American Institute of Chemical Engineers* **1946,** *42* (5-6), 827-848.

15. Tepe, J. B.; Dodge, B. F., Absorption of carbon dioxide by sodium hydroxide solutions in a packed column. *Trans. Am. Inst. Chem. Eng* **1943,** *39*, 255-276.

16. Lackner, K. S.; Grimes, P.; Ziock, H.-J., Carbon dioxide extraction from air: is it an option? *24th Annual Technical Conference on Coal Utilization, Clearwater, FL* **1999**, 885-896.

17. Lackner, K. S., Brennan, S., Matter, J.M., Park, A.H.A., Wright, A. and Van Der Zwaan, B., The urgency of the development of CO2 capture from ambient air. *Proceedings of the National Academy of Sciences* **2012,** *109(33)*, 13156-13162.

18. Zeman, F., Energy and Material Balance of CO2 Capture from Ambient Air. *Environ. Sci. Technol.* **2007,** *41*, 7558-7563.

19. Zeman, F. S., and Lackner, K.S., Capturing carbon dioxide directly from the atmosphere. *World Resource Review* **2004,** *16*, 157-172.

20. Baciocchi, R.; Storti, G.; Mazzotti, M., Process design and energy requirements for the capture of carbon dioxide from air. *Chemical Engineering and Processing: Process Intensification* **2006,** *45* (12), 1047-1058.

21. Mahmoudkhani, M.; Keith, D. W., Low-energy sodium hydroxide recovery for CO2 capture from atmospheric air—Thermodynamic analysis. *International Journal of Greenhouse Gas Control* **2009,** *3* (4), 376-384.

22. Stolaroff, J. K., Keith, D.W. and Lowry, G.V., Carbon Dioxide Capture from Atmospheric Air Using Sodium Hydroxide Spray. *Environ Sci Technol* **2008,** *42*, 2728–2735.

23. Yuan, Z., Eden, M.R. and Gani, R., Toward the Development and Deployment of Large-Scale Carbon Dioxide Capture and Conversion Processes. *Industrial & Engineering Chemistry Research* **2015,** *55(12)*, 3383-3419.

24. Didas, S. A., Choi, S., Chaikittisilp, W. and Jones, C.W., Amine–Oxide Hybrid Materials for CO2 Capture from Ambient Air. *Accounts of chemical research* **2015,** *48(10)*, 2680-2687.

25. Darunte, L. A., Walton, K. S., Sholl, D. S., and Jones, C. W., CO2 capture via adsorption in amine-functionalized sorbents. . *Current Opinion in Chemical Engineering* **2016,** *12*, 82-90.

26. Sanz-Pérez, E. S., Murdock, C.R., Didas, S.A. and Jones, C.W., Direct Capture of CO2 from Ambient Air. *Chemical reviews* **2016**.

27. Simon, A. J., Kaahaaina, N.B., Friedmann, S.J. and Aines, R.D., Systems analysis and cost estimates for large scale capture of carbon dioxide from air. *Energy Procedia* **2011,** *4*, 2893-2900.

28. Smith, P., Davis, S.J., Creutzig, F., Fuss, S., Minx, J., Gabrielle, B., Kato, E., Jackson, R.B., Cowie, A., Kriegler, E. and Van Vuuren, D.P., Biophysical and economic limits to negative CO2 emissions. *Nature Climate Change* **2016,** *6(1)*, 42-50.

29. House, K. Z., Baclig, A.C., Ranjan, M., van Nierop, E.A., Wilcox, J. and Herzog, H.J., Economic and energetic analysis of capturing CO2 from ambient air. *Proceedings of the National Academy of Sciences* **2011,** *108(51)*, 20428-20433.

30. Realff, M. J., and Eisenberger, P., Flawed analysis of the possibility of air capture. *Proceedings of the National Academy of Sciences of the USA* **2012,** *109(25)*, E1589.

31. Socolow, R., A Technology Assessment for the APS Panel on Public Affairs, American Physical Society. *APS physics* **2011**.

32. Krekel, D., Remzi Can Samsun, Ralf Peters, and Detlef Stolten., The separation of CO 2 from ambient air–A techno-economic assessment. *Applied Energy* **2018,** *218*, 361-381.

33. Zeman, F., Reducing the cost of Ca-based direct air capture of CO2. *Environmental science & technology* **2014,** *48 (19)*, 11730-11735.

34. Kulkarni, A. R.; Sholl, D. S., Analysis of Equilibrium-Based TSA Processes for Direct Capture of CO2from Air. *Industrial & Engineering Chemistry Research* **2012,** *51* (25), 8631-8645.

35. Buzanowski, Sorbents for air prepurification in air separation. *Chemical Engineering Science* **2000,** (55), 4827-4838.

36. Buzanowski, Air-prepurification by pressure swing adsorption using single/layered beds. *Chemical Engineering Science* **2001,** (56), 2745-2759.

37. Wang, Q.; Luo, J.; Zhong, Z.; Borgna, A., CO2 capture by solid adsorbents and their applications: current status and new trends. *Energy Environ. Sci.* **2011,** *4* (1), 42-55.

38. Lively, R. P., and Realff, M.J., On thermodynamic separation efficiency: Adsorption processes. *AIChE* **2016**.

39. Sumida, K.; Rogow, D. L.; Mason, J. A.; McDonald, T. M.; Bloch, E. D.; Herm, Z. R.; Bae, T. H.; Long, J. R., Carbon dioxide capture in metal-organic frameworks. *Chemical reviews* **2012,** *112* (2), 724-81.

40. Saha, D.; Bao, Z.; Jia, F.; Shuguang, D., Adsorption of CO2, CH4, N2O, and N2 on MOF-5, MOF-177, and Zeolite 5A. *Environ. Sci. Technol.* **2010,** *44*, 1820-1826.

41. Yazaydın, A. O., Snurr, R.Q., Park, T.H., Koh, K., Liu, J., LeVan, M.D., Benin, A.I., Jakubczak, P., Lanuza, M., Galloway, D.B. and Low, J.J., Screening of Metal-Organic Frameworks for Carbon Dioxide Capture from Flue Gas Using a Combined Experimental and Modeling Approach. *J. AM. CHEM. SOC.* **2009,** *131*, 18198-18199.

42. Yaghi, O. M.; Millward, A. R., Metal-Organic Frameworks with Exceptionally High Capacity for Storage of Carbon Dioxide at Room Temperature. *J. AM. CHEM. SOC.* **2005,** *127*, 17998-17999.

43. Li, J. R.; Kuppler, R. J.; Zhou, H. C., Selective gas adsorption and separation in metal-organic frameworks. *Chemical Society reviews* **2009,** *38* (5), 1477-504.

44. Kuppler, R. J.; Timmons, D. J.; Fang, Q.-R.; Li, J.-R.; Makal, T. A.; Young, M. D.; Yuan, D.; Zhao, D.; Zhuang, W.; Zhou, H.-C., Potential applications of metal-organic frameworks. *Coordination Chemistry Reviews* **2009,** *253* (23-24), 3042-3066.

45. Belmabkhout, Y.; Serna-Guerrero, R.; Sayari, A., Amine-bearing mesoporous silica for CO2 removal from dry and humid air. *Chemical Engineering Science* **2010,** *65* (11), 3695-3698.

46. Bao, Z.; Yu, L.; Ren, Q.; Lu, X.; Deng, S., Adsorption of CO2 and CH4 on a magnesium-based metal organic framework. *Journal of colloid and interface science* **2011,** *353* (2), 549-56.

47. Hong, D. Y., Hwang, Y.K., Serre, C., Ferey, G. and Chang, J.S.,, Porous Chromium Terephthalate MIL-101 with Coordinatively Unsaturated Sites: Surface Functionalization, Encapsulation, Sorption and Catalysis. *Advanced Functional Materials* **2009,** *19(10)*, 1537-1552.

48. Lin, Y., Yan, Q., Kong, C. and Chen, L., Polyethyleneimine incorporated metal-organic frameworks adsorbent for highly selective CO2 capture. *Scientific reports* **2013,** *3*, 1859.

49. Lin, Y., Lin, H., Wang, H., Suo, Y., Li, B., Kong, C. and Chen, L., Enhanced selective CO 2 adsorption on polyamine/MIL-101 (Cr) composites. *Journal of Materials Chemistry A* **2014,** *2(35)*, 14658-14665.

50. Mason, J. A.; Sumida, K.; Herm, Z. R.; Krishna, R.; Long, J. R., Evaluating metal–organic frameworks for post-combustion carbon dioxide capture via temperature swing adsorption. *Energy & Environmental Science* **2011,** *4* (8), 3030.

51. McDonald, T. M., Mason, J.A., Kong, X., Bloch, E.D., Gygi, D., Dani, A., Crocellà, V., Giordanino, F., Odoh, S.O., Drisdell, W.S. and Vlaisavljevich, B.,, Cooperative insertion of CO2 in diamine-appended metal-organic frameworks. *Nature* **2015,** *519(7543)*, 303-308.

52. Rezaei, F.; Subramanian, S.; Kalyanaraman, J.; Lively, R. P.; Kawajiri, Y.; Realff, M. J., Modeling of rapid temperature swing adsorption using hollow fiber sorbents. *Chemical Engineering Science* **2014,** *113*, 62-76.

53. Lively, R. P., Chance, R.R., Kelley, B.T., Deckman, H.W., Drese, J.H., Jones, C.W. and Koros, W.J., Hollow fiber adsorbents for CO2 removal from flue gas. *Industrial & Engineering Chemistry Research* **2009,** *48(15)*, 7314-7324.

54. Casas, N.; Schell, J.; Joss, L.; Mazzotti, M., A parametric study of a PSA process for pre-combustion CO2 capture. *Separation and Purification Technology* **2013,** *104*, 183-192.

55. Wurzbacher, J. A.; Gebald, C.; Piatkowski, N.; Steinfeld, A., Concurrent separation of CO2 and H2O from air by a temperature-vacuum swing adsorption/desorption cycle. *Environ Sci Technol* **2012,** *46* (16), 9191-8.

56. Hefti, M., Joss, L., Bjelobrk, Z. and Mazzotti, M.,, On the potential of phase-change adsorbents for CO2 capture by temperature swing adsorption. *Faraday Discussions.* **2016**.

57. Yates, M.; Blanco, J.; Martin-Luengo, M. A.; Martin, M. P., Vapour adsorption capacity of controlled porosity honeycomb monoliths. *Microporous and Mesoporous Materials* **2003,** *65* (2-3), 219-231.

58. Yu, F. D., Luo, L.A. and Grevillot, G.,, Adsorption Isotherms of VOCs onto an Activated Carbon Monolith: Experimental Measurement and Correlation with Different Models. *J. Chem. Eng. Data* **2002,** *47*, 467-473.

59. Li, Y. Y., Perera, S.P. and Crittenden, B.D.,, Zeolite monoliths for air separation Part 2: Oxygen Enrichment, Pressure Drop and Pressurization. *Trans IChemE* **1998,** *76(8)*, 931-941.

60. Rezaei, F.; Webley, P., Optimum structured adsorbents for gas separation processes. *Chemical Engineering Science* **2009,** *64* (24), 5182-5191.

61. Rezaei, F.; Webley, P., Structured adsorbents in gas separation processes. *Separation and Purification Technology* **2010,** *70* (3), 243-256.

62. Rezaei, F.; Mosca, A.; Hedlund, J.; Webley, P. A.; Grahn, M.; Mouzon, J., The effect of wall porosity and zeolite film thickness on the dynamic behavior of adsorbents in the form of coated monoliths. *Separation and Purification Technology* **2011,** *81* (2), 191-199.

63. Sakwa-Novak, M. A.; Jones, C. W., Steam induced structural changes of a poly(ethylenimine) impregnated gamma-alumina sorbent for CO2 extraction from ambient air. *ACS applied materials & interfaces* **2014,** *6* (12), 9245-55.

64. Hammache, S.; Hoffman, J. S.; Gray, M. L.; Fauth, D. J.; Howard, B. H.; Pennline, H. W., Comprehensive Study of the Impact of Steam on Polyethyleneimine on Silica for CO2Capture. *Energy & Fuels* **2013,** *27* (11), 6899-6905.

65. Li, W.; Bollini, P.; Didas, S. A.; Choi, S.; Drese, J. H.; Jones, C. W., Structural changes of silica mesocellular foam supported amine-functionalized CO2 adsorbents upon exposure to steam. *ACS applied materials & interfaces* **2010,** *2* (11), 3363-72.

66. Chaikittisilp, W.; Kim, H.-J.; Jones, C. W., Mesoporous Alumina-Supported Amines as Potential Steam-Stable Adsorbents for Capturing CO2from Simulated Flue Gas and Ambient Air. *Energy & Fuels* **2011,** *25* (11), 5528-5537.

67. Li, W.; Choi, S.; Drese, J. H.; Hornbostel, M.; Krishnan, G.; Eisenberger, P. M.; Jones, C. W., Steam-stripping for regeneration of supported amine-based CO(2) adsorbents. *ChemSusChem* **2010,** *3* (8), 899-903.

68. Bollini, P., Choi, S., Drese, J.H. and Jones, C.W., Oxidative degradation of aminosilica adsorbents relevant to postcombustion CO2 capture. *Energy & Fuels* **2011,** *25(5)*, 2416-2425.

69. Heydari-Gorji, A.; Sayari, A., Thermal, Oxidative, and CO2-Induced Degradation of Supported Polyethylenimine Adsorbents. *Industrial & Engineering Chemistry Research* **2012,** *51* (19), 6887-6894.

70. Bird, R. B. S., W. E.; Lightfoot, E. N. Transport Phenomena; Wiley: New York, 1960., 780 p.

71. Patton, A., Crittenden, B.D. and Perera, S.P., , Use of the linear driving force approximation to guide the design of monolithic adsorbents. *Chemical Engineering Research and Design* **2004,** *82(8)*, 999-1009.

72. Haynes, W. M., ed. CRC handbook of chemistry and physics. CRC press, 2014.

73. Liu, D., Purewal, J.J., Yang, J., Sudik, A., Maurer, S., Mueller, U., Ni, J. and Siegel, D.J.,, MOF-5 composites exhibiting improved thermal conductivity. *international journal of hydrogen energy* **2012,** *37(7)*, 6109-6117.

74. Huang, B. L., Ni, Z., Millward, A., McGaughey, A.J.H., Uher, C., Kaviany, M. and Yaghi, O.,, Thermal conductivity of a metal-organic framework (MOF-5): Part II. Measurement. *International Journal of Heat and Mass Transfer* **2007,** *50(3)*, 405-411.

75. Osborne, D. W., Schreiner, F., Malm, J.G., Selig, H. and Rochester, L.,, Heat Capacity and Other Thermodynamic Properties of MoF6 between 4° and 350° K. . *The Journal of Chemical Physics* **1966,** *44(7)*, 2802-2809.

76. CoorsTek, I., Cordierite Ceramic Material :: CoorsTek Technical Ceramics. **2016**.

77. Carey, J. W., The heat capacity of hydrous cordierite above 295 K. *Physics and Chemistry of Minerals* **1993,** *19(8)*, 578-583.

78. Bridgeman, O. C. a. A., E.W.,, Vapor pressure tables for water. *Journal of Heat Transfer* **1964,** *86(2)*, 279-286.

79. Saha, D., Bao, Z., Jia, F. and Deng, S.,, Adsorption of CO2, CH4, N2O, and N2 on MOF-5, MOF-177, and zeolite 5A. *Environmental science & technology* **2010,** *44(5)*, 1820-1826.

80. Li, J. R., Ma, Y., McCarthy, M.C., Sculley, J., Yu, J., Jeong, H.K., Balbuena, P.B. and Zhou, H.C.,; Vancouver, Carbon dioxide capture-related gas adsorption and separation in metal-organic frameworks. . *Coordination Chemistry Reviews* **2011.,** *255(15)*, 1791-1823.

81. Zhao, Z., Li, Z., and Lin, Y. S., Adsorption and diffusion of carbon dioxide on metal− organic framework (MOF-5). *Industrial & Engineering Chemistry Research* **2009,** *48.22*, 10015-10020.

82. U.S. Energy Information Administration - EIA - Independent Statistics and Analysis. *Annual Energy Review* **2016**.

83. Daniel DeSantis, J. A. M., Brian D. James, Cassidy Houchins, Jeffrey R. Long,and Mike Veenstra, Techno-economic analysis of metal-organic frameworks for hydrogen and natural gas storage (Accepted). *Environ. Sci. Technol.* **2016**.

84. Broehm, M., Jessica Strefler, and Nico Bauer., Techno-Economic Review of Direct Air Capture Systems for Large Scale Mitigation of Atmospheric CO2. **2015**.

85. Keith, D. W., Ha-Duong, M. and Stolaroff, J.K., Climate strategy with CO2 capture from the air. *Climatic Change* **2006,** *74(1-3)*, 17-45.

86. Lackner, K. S., Capture of carbon dioxide from ambient air. *The European Physical Journal Special Topics* **2009,** *176 (1)*, 93-106.

87. Goeppert, A., Miklos Czaun, GK Surya Prakash, and George A. Olah., Air as the renewable carbon source of the future: an overview of CO 2 capture from the atmosphere. *Energy & Environmental Science* **2012,** *5 (7)*, 7833-7853.

88. Kitajima, K., S. Mulkey, and S. Wright., Decline of photosynthetic capacity with leaf age in relation to leaf longevities for five tropical canopy tree species. *American Journal of Botany* **1997,** *84 (5)*, 702-708.

89. Costa, A., Marcus M. Keane, J. Ignacio Torrens, and Edward Corry., Building operation and energy performance: Monitoring, analysis and optimisation toolkit. *Applied Energy* **2013,** *101*, 310-316.

90. Pérez-Lombard, L., José Ortiz, and Christine Pout., A review on buildings energy consumption information. *Energy and buildings* **2008,** *40 (3)*, 394-398.

91. U.S. Energy Information Administration, Independent Statistics and Analysis. *https://www.eia.gov/totalenergy/data/monthly/#consumption*.

92. Isaac, M., and Detlef P. Van Vuuren., Modeling global residential sector energy demand for heating and air conditioning in the context of climate change. *Energy policy* **2009,** *37 (2)*, 507-521.

93. Ruan, Y., Qingrong Liu, Weiguo Zhou, Ryan Firestone, Weijun Gao, and Toshiyuki Watanabe., Optimal option of distributed generation technologies for various commercial buildings. *Applied Energy* **2009,** *86 (9)*, 1641-1653.

94. Kneifel, J., Life-cycle carbon and cost analysis of energy efficiency measures in new commercial buildings. *Energy and Buildings* **2010,** *42 (3)*, 333-340.

95. Dubois, M.-C., and Åke Blomsterberg., Energy saving potential and strategies for electric lighting in future North European, low energy office buildings: A literature review. *Energy and Buildings* **2011,** *43 (10)*, 2572-2582.

96. Yang, L., Haiyan Yan, and Joseph C. Lam. , Thermal comfort and building energy consumption implications–a review. *Applied Energy* **2014,** *115*, 164-173.

97. Hong, T., Le Yang, David Hill, and Wei Feng., Data and analytics to inform energy retrofit of high performance buildings. *Applied Energy* **2014,** *126*, 90-106.

98. Turnpenny, J. R., D. W. Etheridge, and D. A. Reay., Novel ventilation cooling system for reducing air conditioning in buildings.: Part I: testing and theoretical modelling. *Applied Thermal Engineering* **2000,** *20 (11)*, 1019-1037.

99. Avci, M., Murat Erkoc, Amir Rahmani, and Shihab Asfour., Model predictive HVAC load control in buildings using real-time electricity pricing. *Energy and Buildings* **2013,** *60*, 199-209.

100. Huang, W., and H. N. Lam., Using genetic algorithms to optimize controller parameters for HVAC systems. *Energy and Buildings* **1997,** *26 (3)*, 277-282.

101. Li, D. H., Liu Yang, and Joseph C. Lam., Impact of climate change on energy use in the built environment in different climate zones–a review. *Energy* **2012,** *42 (1)*, 103-112.

102. Bakó-Biró, Z., D. J. Clements-Croome, Neena Kochhar, H. B. Awbi, and M. J. Williams., Ventilation rates in schools and pupils' performance. *Building and Environment* **2012,** *48*, 215-223.

103. A.S.H.R.A.E. Standard 62.1, Ventilation for acceptable indoor air quality. *15* **2004**.

104. Fang, L., Geo Clausen, and Povl Ole Fanger., Impact of temperature and humidity on the perception of indoor air quality. *Indoor air* **1998,** *8 (2)*, 80-90.

105. Toftum, J., Anette S. Jørgensen, and Povl Ole Fanger., Upper limits for indoor air humidity to avoid uncomfortably humid skin. *Energy and Buildings* **1998,** *28 (1)*, 1-13.

106. Daisey, J. M., William J. Angell, and Michael G. Apte., Indoor air quality, ventilation and health symptoms in schools: an analysis of existing information. *Indoor air* **2003,** *13 (1)*, 53-64.

107. Lee, T. S., Jung Hyuk Cho, and Suk Hwan Chi., Carbon dioxide removal using carbon monolith as electric swing adsorption to improve indoor air quality. *Building and Environment* **2015,** *92*, 209-221.

108. Jayathissa, P., Mauro Luzzatto, Jeremias Schmidli, Johannes Hofer, Zoltan Nagy, and Arno Schlueter. , Optimising building net energy demand with dynamic BIPV shading. *Applied Energy* **2017,** *202*, 726-735.

109. Nielsen, T. R., and Christian Drivsholm., Energy efficient demand controlled ventilation in single family houses. *Energy and buildings* **2010,** *42 (11)*, 1995-1998.

110. Wang, Y., Fu-Yun Zhao, Jens Kuckelkorn, Hartmut Spliethoff, and Ernst Rank. , School building energy performance and classroom air environment implemented with the heat recovery heat pump and displacement ventilation system. *Applied Energy* **2014,** *114*, 58-68.

111. Kim, M. K., Luca Baldini, Hansjürg Leibundgut, Jan Andre Wurzbacher, and Nic Piatkowski., A novel ventilation strategy with CO2 capture device and energy saving in buildings. *Energy and Buildings* **2015,** *87*, 134-141.

112. Cui, X., B. Mohan, M. R. Islam, S. K. Chou, and K. J. Chua., Energy performance evaluation and application of an air treatment system for conditioning building spaces in tropics. *Applied Energy* **2017,** *204*, 1500-1512.

113. Thakkar, H., Stephen Eastman, Amit Hajari, Ali A. Rownaghi, James C. Knox, and Fateme Rezaei., 3D-printed zeolite monoliths for CO2 removal from enclosed environments. *ACS applied materials & interfaces* **2016,** *8 (41)*, 27753-27761.

114. Li, G., Penny Xiao, Paul Webley, Jun Zhang, Ranjeet Singh, and Marc Marshall., Capture of CO2 from high humidity flue gas by vacuum swing adsorption with zeolite 13X. *Adsorption* **2008,** *14, no. 2-3*, 415-422.

115. Narayanan, S., Xiansen Li, Sungwoo Yang, Ian McKay, Hyunho Kim, and Evelyn N. Wang., Design and optimization of high performance adsorption-based thermal battery. *American Society of Mechanical Engineers* **2013**, V001T01A044-V001T01A044.

116. Lee, J.-S., Jong-Hwa Kim, Jin-Tae Kim, Jeong-Kwon Suh, Jung-Min Lee, and Chang-Ha Lee., Adsorption equilibria of CO2 on zeolite 13X and zeolite X/activated carbon composite. *Journal of Chemical & Engineering Data* **2002,** *47 (5)*, 1237-1242.

117. Ng, K. C., H. T. Chua, C. Y. Chung, C. H. Loke, T. Kashiwagi, A. Akisawa, and B. B. Saha., Experimental investigation of the silica gel–water adsorption isotherm characteristics. *Applied Thermal Engineering* **2001,** *21 (16)*, 1631-1642.

118. US-Office-Oulook-Q4, http://www.us.jll.com/united-states/en-us/Research/US-Office-Outlook-Q4-2016-JLL.pdf. **2016**.

119. Chua, H. T., K. C. Ng, A. Malek, T. Kashiwagi, A. Akisawa, and B. B. Saha., Modeling the performance of two-bed, sillica gel-water adsorption chillers. *22 (3)* **1999,** *International Journal of Refrigeration*, 194-204.

120. Ferretti, G., Maximal oxygen consumption in healthy humans: theories and facts. *European journal of applied physiology* **2014,** *114 (10)*, 2007-2036.

121. Smith, P. N., Determination of ventilation rates in occupied buildings from metabolic CO2 concentrations and production rates. *Building and Environment* **1988,** *23 (2)*, 95-102.

122. Kuno, Y., Human perspiration. **1956,** *285*.

123. Taylor, T. N., Peter M. Schwarz, and James E. Cochell., 24/7 hourly response to electricity real-time pricing with up to eight summers of experience. *Journal of regulatory economics* **2005,** *27 (3)*, 235-262.

124. NREL, Life Cycle Greenhouse Gas Emissions from Electricity Generation. *https://www.nrel.gov/docs/fy13osti/57187.pdf*.

125. EIA (2017). 2017 Annual Energy Outlook, T. A. E. S., Disposition, Prices, and Emissions.

126. Miller, D. C., Madhava Syamlal, David S. Mebane, Curt Storlie, Debangsu Bhattacharyya, Nikolaos V. Sahinidis, Deb Agarwal et al., Carbon capture simulation initiative: a case study in multiscale modeling and new challenges. *Annual review of chemical and biomolecular engineering* **2014,** *5*, 301-323.

127. Biegler, L. T., Ignacio E. Grossmann, and Arthur W. Westerberg., Systematic methods for chemical process design. **1997**.

128. Sahraei, M. H., Duchesne, M.A., Hughes, R.W. and Ricardez-Sandoval, L.A., Experimental assessment, model validation and uncertainty quantification of a pilot-scale gasifier. *Industrial & Engineering Chemistry Research* **2016**.

129. Xiu, D., Fast numerical methods for stochastic computations: a review. *Communications in computational physics* **2009,** *5(2-4)*, 242-272.

130. Oberkampf, W. L.; Deland, S. M.; Rutherford, B. M.; Diegert, K. V.; Alvin, K. F., Error and uncertainty in modeling and simulation. *Reliability Engineering and System Safety* **2002,** *75*, 33-357.

131. Wilson, F. Z. a. J. R., Accounting for parameter uncertainty in simulation input modeling. *IIE Transactions* **2003,** *35* (9), 781-792.

132. Michael D. McKay l, J. D. M., Stephen C. Upton Evaluating prediction uncertainty in simulation models. *Computer Physics Communications* **1999,** *117*, 44-51.

133. Hammersley, J., Monte carlo methods. *Springer Science & Business Media* **2013**.

134. Kuczera, G. a. P., E., Monte Carlo assessment of parameter uncertainty in conceptual catchment models: the Metropolis algorithm. *Journal of Hydrology* **1998,** *211(1)*, 69-85.

135. Annan, J. D.; Vancouver, Modelling under uncertainty: Monte Carlo methods for temporally varying parameters. *Ecological Modelling* **2001,** *136(2)*, 297-302.

136. Davis, T. J.; Keller, C. P., Modelling uncertainty in natural resource analysis using fuzzy sets and Monte Carlo simulation: slope stability prediction. *International Journal of Geographical Information Science* **1997,** *11* (5), 409-434.

137. Cox, M.; Harris, P.; Siebert, B. R.-L., Evaluation of measurement uncertainty based on the propagation of distributions using monte carlo simulation. *Measurement Techniques* **2003,** *46* (9), 824-833.

138. He, J. H., Homotopy perturbation method: a new nonlinear analytical technique. *Applied Mathematics and computation* **2003,** *135(1)*, 73-79.

139. Kleiber, M. a. H., T.D., The stochastic finite element method. *John Wiley, New York* **1992**.

140. Xiu, D. a. K., G.E., Supersensitivity due to uncertain boundary conditions. *International journal for numerical methods in engineering* **2004,** *61(12)*, 2114-2138.

141. Ghanem, R. a. S., P.D., A stochastic Galerkin expansion for nonlinear random vibration analysis. *Probabilistic Engineering Mechanics* **1993,** *8(3-4)*, 255-264.

142. Xiu, D. a. S., J., Efficient stochastic Galerkin methods for random diffusion equations. *Journal of Computational Physics* **2009,** *228(2)*, 266-281.

143. Wiener, N., The homogeneous chaos. *American Journal of Mathematics* **1938,** *60(4)*, 897-936.

144. Onorato, G., Loeven, G.J.A., Ghorbaniasl, G., Bijl, H. and Lacor, C., Comparison of intrusive and non-intrusive polynomial chaos methods for CFD applications in

aeronautics. *V European Conference on Computational Fluid Dynamics ECCOMAS, Lisbon, Portugal* **2010**, 14-17.

145. Najm, H. N., Uncertainty Quantification and Polynomial Chaos Techniques in Computational Fluid Dynamics. *Annual Review of Fluid Mechanics* **2009,** *41* (1), 35-52.

146. Ernst, O. G., Mugler, A., Starkloff, H.J. and Ullmann, E., On the convergence of generalized polynomial chaos expansions. *ESAIM: Mathematical Modelling and Numerical Analysis* **2012,** *46(2)*, 317-339.

147. Xiu, D. a. K., G.E., Modeling uncertainty in flow simulations via generalized polynomial chaos. *Journal of computational physics* **2003,** *187(1)*, 137-167.

148. Li, R., Ghanem, R., Adaptive polynomial chaos expansions applied to statistics of extremes in nonlinear random vibration. *Probabilistic engineering mechanics* **1998,** *13(2)*, 125-136.

149. Reagan, M. T.; Najm, H. N.; Debusschere, B. J.; Maître, O. P. L.; Knio, O. M.; Ghanem, R. G., Spectral stochastic uncertainty quantification in chemical systems. *Combustion Theory and Modelling* **2004,** *8* (3), 607-632.

150. Helton, J. C. a. D., F.J., Latin hypercube sampling and the propagation of uncertainty in analyses of complex systems. *Reliability Engineering & System Safety* **2003,** *81(1)*, 23-69.

151. Simpson, T. W., Lin, D.K. and Chen, W., Sampling strategies for computer experiments: design and analysis. *International Journal of Reliability and Applications* **2001,** *2(3)*, 209-240.

152. Olsson, A. M., and Sandberg, G.E., Latin hypercube sampling for stochastic finite element analysis. *Journal of Engineering Mechanics* **2002,** *128(1)*, 121-125.

153. Hosder, S., Walters, R.W., and Balch, M., Efficient sampling for non-intrusive polynomial chaos applications with multiple uncertain input variables. *AIAA paper* **2007,** *1939*, 2007.

154. Eldred, M. S., Recent advances in non-intrusive polynomial chaos and stochastic collocation methods for uncertainty analysis and design. *AIAA Paper* **2009,** *2274(2009)*, , 37.

155. Reagana, M. T., Najm, H.N., Ghanem, R.G. and Knio, O.M., Uncertainty quantification in reacting-flow simulations through non-intrusive spectral projection. *Combustion and Flame* **2003,** *132(3)*, 545-555.

156. Der Kiureghian, A., and Pei-Ling Liu., Structural reliability under incomplete probability information. *Journal of Engineering Mechanics* **1986,** *112.1*, 85-104.

157. Box, G. E. a. C., D.R., An analysis of transformations. *Journal of the Royal Statistical Society. Series B (Methodological)* **1964**, 211-252.

158. Rosenblatt, M., Remarks on a multivariate transformation. *The annals of mathematical statistics* **1952,** *23(3)*, 470-472.

159. Marzouk, Y. M., Najm, H.N. and Rahn, L.A., Stochastic spectral methods for efficient Bayesian solution of inverse problems. *Journal of Computational Physics* **2007,** *224(2)*, 560-586.

160. Oladyshkin, S. a. N., W., Data-driven uncertainty quantification using the arbitrary polynomial chaos expansion. *Reliability Engineering & System Safety* **2012,** *106*, 179-190.

161. Crestaux, T., Le Maıˆtre, O. and Martinez, J.M., Polynomial chaos expansion for sensitivity analysis. *Reliability Engineering & System Safety* **2009,** *94(7)*, 1161-1172.

162. Blatman, G. a. S., B., Adaptive sparse polynomial chaos expansion based on least angle regression. *Journal of Computational Physics* **2011,** *230(6)*, 2345-2367.

163. Choi, S. K., Grandhi, R.V., Canfield, R.A. and Pettit, C.L., Polynomial chaos expansion with latin hypercube sampling for estimating response variability. *AIAA journal* **2004,** *42(6)*, 1191-1198.

164. Ghiocel, D. M. a. G., R.G., Stochastic finite-element analysis of seismic soil-structure interaction. *Journal of Engineering Mechanics* **2002,** *128(1)*, 66-77.

165. Ghanem, R. G. a. S., P.D., Stochastic finite elements: a spectral approach. *Courier Corporation* **2003**.

166. Xiu, D. a. K., G.E., The Wiener--Askey polynomial chaos for stochastic differential equations. *SIAM journal on scientific computing* **2002,** *24(2)*, 619-644.

167. Xiu, D. a. K., G.E., Modeling uncertainty in steady state diffusion problems via generalized polynomial chaos. *Computer methods in applied mechanics and engineering* **2002,** *191(43)*, 4927-4948.

168. Xiu, D., Lucor, D., Su, C.H. and Karniadakis, G.E., Stochastic modeling of flow-structure interactions using generalized polynomial chaos. *Journal of Fluids Engineering* **2002,** *124(1)*, 51-59.

169. Tatang, M. A., Direct incorporation of uncertainty in chemical and environmental engineering systems (Doctoral dissertation). Massachusetts Institute of Technology. **1995**.

170. Najm, H. N.; Debusschere, B. J.; Marzouk, Y. M.; Widmer, S.; Le MaÃ®tre, O. P., Uncertainty quantification in chemical systems. *International Journal for Numerical Methods in Engineering* **2009,** *80*, 789-814.

171. Villegas, M., Augustin, F., Gilg, A., Hmaidi, A. and Wever, U., Application of the polynomial chaos expansion to the simulation of chemical reactors with uncertainties. *Mathematics and Computers in Simulation* **2012,** *82(5)*, 805-817.

172. Reagan, M. T., Najm, H.N., Pebay, P.P., Knio, O.M., and Ghanem, R.G., Quantifying uncertainty in chemical systems modeling. *International journal of chemical kinetics* **2005,** *37(6)*, 368-382.

173. Le Maître, O. P., Najm, H.N., Pébay, P.P., Ghanem, R.G. and Knio, O.M., Multi-resolution-analysis scheme for uncertainty quantification in chemical systems. *SIAM Journal on Scientific Computing* **2007,** *29(2)*, 864-889.

174. Zhang, Y., and Sahinidis, N.V., Uncertainty quantification in CO2 sequestration using surrogate models from polynomial chaos expansion. *Industrial & Engineering Chemistry Research* **2012,** *52(9)*, 3121-3132.

175. Sacks, J., Welch, W.J., Mitchell, T.J. and Wynn, H.P., Design and analysis of computer experiments. *Statistical science* **1989**, 409-423.

176. Sinha, A., Lalit A. Darunte, Christopher W. Jones, Matthew J. Realff, and Yoshiaki Kawajiri., Systems Design and Economic Analysis of Direct Air Capture of CO2 through Temperature Vacuum Swing Adsorption using MIL-101 (Cr)-PEI-800 and mmen-Mg2 (dobpdc) MOF Adsorbents. *Industrial & Engineering Chemistry Research* **2017,** *56 (3)*, 750-764.

177. Bui, M., Claire S. Adjiman, André Bardow, Edward J. Anthony, Andy Boston, Solomon Brown, Paul S. Fennell et al., Carbon capture and storage (CCS): the way forward. *Energy & Environmental Science* **2018**.

178. Darunte, L. A. Application of Metal-Organic Frameworks (MOFs) to Capturing CO2 Directly from Air. Doctoral dissertation, Georgia Institute of Technology, 2018.

179. Serna-Guerrero, R., and Abdelhamid Sayari., Modeling adsorption of CO2 on amine-functionalized mesoporous silica. 2: Kinetics and breakthrough curves. *Chemical Engineering Journal* **2010,** *161, no. 1-2* 182-190.

180. Sahinidis, N. V., Optimization under uncertainty: state-of-the-art and opportunities. *Computers & Chemical Engineering* **2004,** *28, no. 6-7*, 971-983.

181. Jeong, K., Kessen, M.J., Bilirgen, H. and Levy, E.K.,, Analytical modeling of water condensation in condensing heat exchanger. *International Journal of Heat and Mass Transfer* **2010,** *53(11)*, 2361-2368.